FLAME STABILIZATION IN GAS-FUELED INVERSE DIFFUSION FLAMES AND LIQUID-FUELED SWIRLING COMBUSTION

XUREN ZHU

PhD

The Hong Kong Polytechnic University

2018

The Hong Kong Polytechnic University

Department of Mechanical Engineering

Flame Stabilization in Gas-fueled Inverse Diffusion Flames and Liquid-fueled Swirling Combustion

Xuren Zhu

A thesis
submitted in partial fulfillment of the requirements for the degree
of
Doctor of Philosophy

May 2017

CERTIFICATE OF ORIGINALITY

I hereby declare that this thesis is my own work and that, to the best of my knowledge and belief, it reproduces no material previously published or written, nor material that has been accepted for the award of any other degree of diploma, except where due acknowledgement has been made in the text.

____(Signed)

____Xuren Zhu______________________(Name of student)

Abstract

Three parts are illustrated in the present work on the non-premixed flames, which includes near-field flow stability of buoyant methane/air inverse diffusion flames, wall effects on the stability of buoyant inverse diffusion flames of methane and the influence of centerbody air injection on liquid combustion in a model gas turbine combustor.

In the first part, experiment and simulation were performed to investigate buoyant methane/air inverse diffusion flames, with emphasis on the near-field flow dynamics under non-reacting and reacting conditions. In the non-reacting flow condition, the initial shear flow and the buoyancy effect induce opposite-direction vortices, which interact with each other and cause flow instability similar to the mechanism forming the von Karman vortex street. The instability is greatly intensified at around unity Richardson number, when the two vortices are comparably strong. In the reacting inverse diffusion flame, the density gradient is reversed due to chemical heat release and so is the buoyancy-induced vortex that it has the same direction with the vortex of the initial shear flow. As a result, the buoyancy-induced vorticity generation would facilitate the growth of the initial shear layer, thus the near-field flow remains stable. However, the growing shear flow would eventually lead to the development of the Kelvin-Helmholtz instability in the far field.

In the second part, experimental and numerical studies were performed to examine the stability of inverse diffusion flames (IDFs) with the focus on the boundary wall effects. A regime diagram for flame stability was obtained based on the visual characteristics of flames and verified by the simulated flow fields. The boundary wall effect was identified and investigated by simulating the IDFs with different outer burner diameters. It was found that the wall-bounded induced shear layers (WISLs) either reduce the flow instability by vorticity diffusion or enhance it by vorticity convection. Proposed as a way to control the IDF stability, an additional shear layer with opposite vorticity sign to the main shear layer was created in the fuel inflow to emulate the wall effects on the IDFs. This non-uniform fuel inflow was found to suppress the flame instability by restraining the development of the main shear layers through vorticity diffusion.

In the liquid gas turbine non-premixed combustion, a portion of centerbody air is injected directly into the central recirculation zone. The experimental and numerical results show that an enlarged recirculation zone with higher temperature can be formed in the swirl combustor with the centerbody air injection, which therefore may hold potentials in enhancing flame stabilization and combustion efficiency In addition, the centerbody air injection pushes the recirculation zone to the farther downstream of the fuel injector and hence can reduce the exposure of the fuel injector to the high-temperature combustion zone. Since the centerbody air injection was found to only slightly modify the effective swirl number, the modified velocity and temperature characteristics are mainly due to the changes of the shape and location of the central recirculation zone and the local stoichiometry in the vicinity of fuel injection. A parametric study for various inlet air velocities and excess air factors further substantiates the effectiveness of the centerbody air injection on improving the combustion performance although the extent of the improvement relies on other factors that therefore merits future studies for optimization design.

Keywords: non-premixed combustion; inverse diffusion flames; swirl combustion; center air injection; flame oscillation; wall effect.

Publications

1. **X. Zhu**, R. Li, D. Li, P. Zhang, R. Qian, Experimental study and RANS calculation on velocity and temperature of a kerosene-fueled swirl laboratory combustor with and without centerbody air injection, International Journal of Heat and Mass Transfer, 89 (2015) 964-976.
2. **X. Zhu**, X. Xia and P. Zhang, Near-field Flow Stability of Buoyant Methane/Air Inverse Diffusion Flames, Combustion and Flame (*accepted*)
3. **X. Zhu**, X. Xia and P. Zhang, Wall Effects on the Stability of Buoyant Inverse Diffusion Flames of Methane (under review)
4. **X. Zhu** and P. Zhang, Experimental Study and Numerical Simulation on a Cross-Drilled Swirl Combustor. The 10th Asia-Pacific Conference on Combustion, Beijing, July 19-22, 2015.
5. **X. Zhu**, X. Xia and P. Zhang, Flow and Flame Dynamics of a Confined Buoyant Inverse Diffusion Flame. The 11th Asia-Pacific Conference on Combustion, Sydney, December 10-14, 2017.

Acknowledgement

First I would like to express my sincere gratitude to my supervisor Prof. Peng Zhang for the continuous support of my Ph.D study and related research for his patience, motivation, and immense knowledge. His have guided and mentored me in research for the last three years and introduced me to the topic of combustion. The joy and enthusiasm he has for his research was contagious and motivational for all the group members.

I would also thank my co-supervisor Prof. Chun Wah LEUNG and Prof. Chih Yung WEN who provided me to have the facilities in Heat Transfer and Combustion Laboratory and Wind Tunnel Laboratory respectively. Thanks to the technician office Chris Tsang and Mr. Lu Shen for their generous help on my experiments. Without their help it would not be possible for me to finish my project.

Special thanks should also be given to Dr. Xi Xia who helped me so much in the analysis of the results and provided me a lot of very usefully suggestions of writing this thesis. I would also like to thank all of my group members who worked with me and talked with me even in the tough time of my Ph.D study.

Last but not the least, I would like to express my gratitude to my family and my girlfriend for supporting me spiritually throughout my Ph.D study and my life. Your devotion, unconditional love and support, optimism and advice was more valuable than you could ever imagine.

Contents

List of Figures

List of Tables

1 Introduction

1.1 Background

Combustion affords greatest amount of the energy consumption in the modern world. For the past decades the reduction of fuel consumption and harmful pollutants from combustion systems has been the major actuator of combustion technology development.

In many combustion processes, the oxidizer and fuel are separated injected before going into the combustion region where they mixing together and burn. These combustion reactions are named as non-premixed flames or diffusion flames since the transport of oxidizer and fuel into the combustion zone mainly controlled by diffusion.

In a wide range of combustion phenomenon such as industrial flames, fire and domestic flames etc. are operates in non-premixed mode. However, the presence of soot has an objectionable influence on combustion. Most importantly, these soot formation produce potential harm to human health and environment. In fire accidents for instance, much heavier loss caused due to the existence of toxic emissions which may contain soot, soot precursors, such polycyclic aromatic hydrocarbons generated in underventilated fires [1-4]. Moreover, enhanced radiation heat transfer due to soot formation is a very important factor for the accidental fires rapid spread [5, 6].

To protect the increasing worse environment and to achieve fire safety, it is essential to research and predict the detail of soot formation. As a special kind of non-premixed flame, Inverse diffusion flame was designed for providing further understanding of soot formation in common and in underventilated flames [7-9].

In normal diffusion flames (NDF), soot form on the insider of flame since fuel is injected in the center and surrounded by air injection. Thus, in the over ventilated NDF soot will be oxidized without emitting when going through the flame due to its closed flame tip. In IDFs, soot forms on the surrounding of the flame since fuel injection is surrounded by air flow, Owing to Sorret effect it can escape without being oxidized from the flame since it never go through the flame [8, 10, 11]. Therefore, IDFs may provide clear insights into soot initial inception and growth.

It is noted that flow field generates essential influence on the IDFs correspondingly soot formation[12, 13]. Despite that a wide range of study on IDFs has been carried out over the past decades both on flow and flame characteristics, [14-19] flame dynamics and characteristics in IDFs are still not fully explained, detailed research on the influence of flow field in IDFs which is an essential step is still highly in demand. In the previous research, it was assumed that the flow field in IDFs is similar to that of NDFs in which air co-flow entrainment dominates in the near field of the flame base, resulting a radial inflow from the side of main injection with a vertical buoyant flow [20]. In a work by Blevins et al. [21], a schematic of the IDF flow field was given, inward flow in the near field has a slight expansion with a small radial out flow after a short distance of development. By using laser Doppler velocimetry, Kang et al. [22] found that the air flow in IDF tends to going outward to the fuel side. Shaddix and Williams [23] provided measurements of the velocity field in IDFS fueled with ethylene. However, no detailed research on flow or flame oscillation phenomenon was given.

Back to 1984, Wu and Essenhigh [24] gave a detailed map for the structure of methane IDFs. It was found that with very flow fuel inlet velocity (< 1cm/s), the IDFs started to oscillate with a frequency of 1-2 Hz. It was declared that the oscillation would be related to the relative important buoyancy effect in the low fuel injection velocity condition. Katta et al. [15] investigated the dynamics of an in IDF, the main focus was put on the role of flow dynamics in the polycyclic-aromatic-hydrocarbon and soot formation. In both work, no further detailed analysis for the flame or flow dynamics of the IDF flow field was provided.

For relative high inflow velocity combustion system, gas turbine combustion in power plant for instance, due to safety reasons also mostly operate in the non-premixed burning mode. In non-premixed gas turbine combustion system, the main aims are to increase the turbine inlet temperature while keeping NOx emission in a low level, extend stability limit, improve cycle heat efficiency and decrease running cost. Tremendous efforts have been made on these topics [25-27].

Swirler and swirl combustion which are widely used in gas turbine combustor have been extensively studied in the past decades. Beer and Chigier [28] systematically summarized earlier studies on swirl combustion. Syred and Beer [29] and Lilley [30] reviewed non-reacting and reacting flows in the swirl combustors. Gupta, Lilley and Syred [31] described rich physical phenomena and flow characteristics of swirl flows and summarized the relevant engineering applications. In recent years, studies on swirling combustion have been carried out in the context of combustion instability.[32] A stability regime diagram was determined by Syred [33] to correlate the operating conditions with the occurrence of instabilities.Lieuwen, Neumeier and Zinn [34] suggested that the deficient mixing process produces varying local equivalent ratios in the flame zone, which play an important role in inducing combustion instabilities. Swirling flame dynamics and its relation with combustion instability was also reviewed by Candel, Durox, Schuller, Palies, Bourgouin and Moeck [35]

Because the flame stabilization in a swirl combustor is realized by forming a backflow that entrains a portion of the post-combustion gases to mix with the incoming air and fuel, the size, shape and flow characteristics of the CRZ are of critical importance. Rhode, Lilley and Mclaughlin [36] experimentally studied the mean flow field in axisymmetric swirl combustors with emphasis on the important role of CRZ. It was found that the CRZ is enlarged with increasing the swirl vane angle and that the corner bubble is eliminated and larger axial velocities occur when the side-wall angle decreases. In the experiments of Ghaffarpour and Chehroudi [37]， the average temperature were measured at the axial positions and the flow velocity was measured by using a Laser Doppler Velocimeter (LDV). They found that, at a fixed flow rate of diluted air, increasing swirling air flow rate may eventually extinguish the flame, while the flame may be blown out from the combustor when the swirling air flow is decreased.Valera-Medina, Syred and Bowen [38] characterized the CRZ under reacting flow conditions and found that partially premixed combustion at near-stoichiometric equivalence ratios reduced the coherence of the CRZ and often caused it to nearly disappear, while the CRZ was strengthened at low equivalence ratios for both non-premixed and partially premixed combustion. Eaton and Johnston [39] found that the streamwise pressure gradient, which is partially controlled by the overall system geometry, directly influences the size and shape of the CRZ. Anacleto, Fernandes, Heitor and Shtork [40] investigated the swirl flow structure and the flame characteristics in a model lean premixed combustor and found that the swirl number and the expansion ratio of the combustor are the determining factors of the adverse pressure gradient.

Fuel/air mixing in CRZ has a strong influence on the combustion efficiency and flame stabilization in swirl combustors.[41-43] Anacleto, Fernandes, Heitor and Shtork [40]found that increasing the swirling intensity and preheating the airflow was able to provide a high level of fuel pre-vaporization and enhanced mixing before the combustion zone. Chen and Driscoll [44] found that the CRZ enhances the fuel/air mixing, thus the CRZ acts like a large toroidal vortex with a characteristic velocity and length scale and the air is entrained into the vortex from the downstream region of the vortex. Sankaran and Menon [45] found that that increasing swirl number promotes the vortex breakdown and spray dispersion which in turn lead to enhanced fuel/air mixing. Lee and Moon [46] introduced a turbulent generator by installing saw blades on the swirl vanes to significantly enhance turbulent mixing of fuel and air. Terasaki and Hayashi [47] investigated a non-premixed gas turbine combustor with double swirler and found that the mixing of fuel and air was more rapid in the double-swirler burner than that in the conventional single-swirl burners.

Recent advances in computational fluid dynamics and high-performance computing facilities enable the high-quality numerical simulation of turbulent swirling flow and swirl combustion. Bowen, O'Doherty and Lucca‐Negro [48] applied Reynolds stress model in the simulation of swirl-burner furnace system, which qualitatively agreed with their experimental data. Guo, Langrish and Fletcher [49] employed a k–ε turbulent model in their RANS simulation to study a low-swirl flow in a sudden expansion chamber and observed several modes of vortex core oscillation. Wegner, Maltsev, Schneider, Sadiki, Dreizler and Janicka [50] evaluated the performance of the unsteady RANS (U-RANS) method in predicting the vortex core phenomenon and found that U-RANS is able to capture the vortex core both qualitatively and quantitatively. The swirl effects on velocity, mixture fraction, and temperature intermittency were studied by Ranga Dinesh, Jenkins, Kirkpatrick and Malalasekera [51] for turbulent methane flames by using large eddy simulation (LES). Their results show that due to the occurrence of recirculation zones, the transition from laminar to turbulent is more rapid for the velocity than the mixture fraction. Huang and Yang [52] used LES to investigate the combustion dynamics in a lean-premixed swirl combustor. Their results indicate that, beyond a critical inlet swirl number, a vortex-breakdown-induced central toroidal recirculation zone is established in the downstream region, while the excessive swirl may cause the central recirculating flow to penetrate into the inlet annulus and lead to the occurrence of flame flashback. The LES of Sankaran and Menon [45] on the spray combustion in swirling flows shows that combustion heat release tends to reduce the size of the CRZ.

Regardless of the merits of swirl combustion, an excessive swirl may cause the central recirculation flow to move into the inlet annulus and lead to the occurrence of flame flashback in premixed combustion.[52-54] To solve the flashback problem in premixed combustors, Terhaar, Reichel, Schrödinger, Rukes, Paschereit and Oberleithner [55] introduced an axial air injection through the center body and found that the axial air injection provided a suitable flow field for flame stabilization and flashback-proof. For non-premixed combustors, which although are completely free from flashback, the overheating problem of the fuel nozzle and combustion chamber wall is arisen[56, 57]. Fang, Majdalani and Chiaverini [58] developed a cold-wall bidirectional vortex non-premixed combustion chamber, in which the swirling flow is separated into two distinct coaxial zones, with the outer vortex stream circulating towards the head end and an inner concentric vortex in the opposite direction. The outer vortex protects the chamber walls from excessive heating loads via convective cooling.

Efforts have been made to develop novel swirl combustors through the design of swirler. Notable examples are the double-stage and even triple-stage swirler combustors. Grinstein, Young, Gutmark, Li, Hsiao and Mongia [59] studied the flow dynamics in a series of combustors with single-stage, double-stage and triple-stage swirlers, found that the flow is very sensitive to the detailed nature of the velocity radial profiles. Kamal [60] found that by injecting the coal with a gas/air mixture as a combined central jet surrounded by a swirled air stream, a double flame envelope develops with high temperature fuel-rich conditions between the reaction zones so that the pyrolysis reactions to N_2 are facilitated. Cheng, Yegian, Miyasato, Samuelsen, Benson, Pellizzari and Loftus [61] and Littlejohn, Majeski, Tonse, Castaldini and Cheng [62] have developed a low swirl combustion (LSC) technology which has evolved into a simple and robust ultra-low emissions combustion technology for burners in industrial heaters and in gas turbines for electricity production. Note that, the main idea of LSC is to reduce the swirl intensity well below the vortex breakdown threshold by introducing axial flows through the central channel without being swirled, such that no recirculating flow generated in the combustor. Zhao, Zhou and Zhao [63] proposed a petal swirl burner (PSB), which has been successfully applied in boiler burners of electric power generation. To study the influence of axial injection on flashback in premixed combustion, vortex breakdown types and helical instabilities in a swirling combustor were also investigated by Terhaar, Reichel, Schrödinger, Rukes, Paschereit and Oberleithner [55] Recently, the authors[64] designed and implemented a cross-drilled swirler in a model gas-turbine combustor and found it holds potential in prominently enhancing the combustion efficiency. In their testing experiment, a small amount of fuel and air was delivered directly into the CRZ from the slots and then ignited in the high-temperature CRZ to produce a stabilized pilot flame. Similar design was used by Qian, Wu, Jin and Du [65] in bluff-body flame holders by cutting a slot in the center of a bluff-body.

1.2 Objectives

In the present work, both numerical simulation and experimental approaches have been applied to research the dynamics of IDFs, wall effect and characteristics of IDFs and influence of centerbody air injection on liquid combustion in a model gas turbine combustor. In the research of dynamic of IDFs, large eddy simulation (LES) combined with infinite fast irreversible chemical reaction was performed to obtain detailed unsteady flow field information. Reynolds averaged Navier-Stokes (RANS) were used to exam the liquid gas turbine combustion. In experimental study, particle image velocimetry (PIV) system was used to investigate the non-reacting flow in the research of the dynamics of IDFs. IDFs' flow field and flame images were captured by high speed camera and normal camera respectively for qualitative validation and analysis. All of the numerical results were validated either by the present experiments. This work aims,

(1) To identify the fundamental physics of the oscillation in the non-reacting and reacting IDFs based on the detailed results obtained in the experimental and numerical work

(2) To understand the fundamental vortex dynamics mechanisms associated with the wall effect and their effects on flow stability of IDF

(3) To research the flow and temperature characteristics of the CRZ in the non-premixed model gas turbine combustor with or without centerbody air injection and to explore the potential advantages of the centerbody air injection in the combustion efficiency and flame stability.

1.3 Thesis Stucture

This thesis is distributed into three parts.

In Part I, flow dynamics of IDFs have been research both under non-reacting and reacting conditions. Large eddy simulation validated by PIV results were used to analyse the non-reacting flow. Under reacting condition, large eddy simulation coupled with and infinite fast irreversible chemistry was performed, flame images were obtained to further validate the numerical results. Detailed steady and unsteady flow information was acquired and the fundamental physics in the dynamics of the IDFs was given by analysing the flow field.

In Part II, IDFs will be investigated through qualitative experimental observations and then detailed vortex flow analysis based on numerical simulation. The main objective is to understand the fundamental vortex dynamics mechanisms associated with the wall effect and their effects on flow stability of IDFs. Inspired by the knowledge of the wall effect, a shear-layer-based injection technique will be proposed and substantiated for flow stabilization control of IDFs.

In Part III, detailed experimental study and RANS simulation on a non-premixed model gas turbine combustor fueled with kerosene were conducted with particular interests in characterizing the flow and temperature characteristics of the CRZ in the combustor with centerbody air injection. By using the RANS simulation, which has been validated by the present experimental data, the influence of airflow velocity and excess air factor, was parametrically studied to demonstrate the effectiveness of the centerbody injection.

The conclusions of the work are presented in the following Chapter of Part III.

2 Part I: Research of Dynamics of Inverse Diffusion Flames

2.1 Introduction

Buoyant diffusion flames exist in a wide range of industrial combustion devices and accidental fires. The research of buoyant diffusion flames is of great significance in optimizing combustion performance, controlling environmental pollution and reducing fire damage. In buoyant diffusion flames, flow instability and laminar-turbulent transition are evident in the near-field where fuel and air mix with each other [66]. The distinct flow and flame dynamics of buoyant diffusion flames have been attributed to combustion heat release, fuel-air density difference, and fuel and air Reynolds numbers [67-69]， where the former two are the main factors contributing to the buoyancy effect and greatly influence the flame dynamics at low Reynolds numbers [70].

A number of investigations have been performed to understand the flame or flow instabilities of buoyant normal diffusion flames (NDFs) [71-75], where the flames oscillate at the relatively low frequencies typical of 10-20 Hz [71, 76, 77]. It was also found that the oscillation frequency is slightly affected by the fuel type, the fuel nozzle size, or the fuel inlet velocity [66, 78-82]. Because of the coupling of inertial instability, buoyancy, vortex dynamics, and chemical heat release, it is usually difficult to isolate one factor from another in the study of buoyant NDFs. As a result, the existing literature does not consent on the mechanism of the flow and flame instability in reacting or even non-reacting conditions[83]. Cetegen and Kasper [84] attributed buoyant flow instability to Rayleigh-Taylor instability, but Coats [66] and Buckmaster and Peters [85] to Kelvin-Helmholtz instability. Buckmaster and Peters [85] proposed that the buoyant flow instability is a convective instability that is controlled by the thermomechanical properties of the hot and cold gases under the gravitational acceleration, but others considered the buoyant flows absolutely unstable [86-88]. Jiang and Luo [67, 89-91] studied the formation of large vortex structures in buoyant reactive plumes and found that the enhanced tendency of flow transition to turbulence in buoyant NDFs is due to combustion induced buoyancy, in contrast to the re-laminarization effect of chemical exothermicity in non-buoyant NDFs.

Inverse diffusion flames (IDFs), where oxidizer is surrounded by fuel in contrast to fuel being surrounded by air in NDFs, have been extensively investigated in laboratory with emphasis on soot formation [13, 16, 92, 93]. Soot formation in IDFs was found to be significantly influenced by the flow field characteristics [12, 13]. However, to the authors' knowledge, relatively limited research attention was focused on the flow and flame dynamics in IDFs. Santoro et al. [20] assumed that the flow field in IDFs is similar to that of NDFs, in which air co-flow entrainment dominates the near-field of the flame base and results in a radial inflow from the side of the main injection together with a vertical buoyant flow. Blevins et al. [21] gave a schematic of the IDF flow field, where the inward flow in the near-field has a slight expansion, resulting in a small radial out flow after a short distance of development. By using laser Doppler velocimetry, Kang et al. [94] found that the air flow in IDF tends to move outward to the fuel side. Shaddix and Williams [12] provided the velocity field data for ethylene IDFs and used the velocity data for soot formation analysis. Recently, Sen et al. [95] adopted dynamic systems analysis to understand the connection between flame dynamics and thermoacoustic characteristics of a ducted IDF. In spite of these worthy studies, limited details were provided on the flow or flame oscillation of IDFs in most literature.

In their early study, Wu and Essenhigh [96] gave a detailed map for the structure of methane IDFs. They found that, with a very low fuel inlet velocity (< 1cm/s), the IDFs started to oscillate with a frequency of 1-2 Hz, probably because of the relatively important buoyancy effect. Katta et al. [15] investigated the dynamics of an IDF, for which the main focus was on the role of flow dynamics in the polycyclic-aromatic-hydrocarbon (PAH) and soot formation. According to their simulation results, the advection of vorticities at 17.2 Hz enhanced the mixing of the species and contributed to a more uniform distribution of PAH in the downstream. In both works, no further analysis was provided to address the flame or flow dynamics of the IDF, e.g. the main factor determining the instability.

In this part, the non-reacting and reacting flows of methane/air IDFs were examined through both experiment and numerical simulation. Particle Image Velocimetry (PIV) system was used for the measurement of non-reacting flows. Large eddy simulation (LES), which has been sufficiently validated by the PIV experiment, was applied to analyze the unsteady flow and flame dynamics. The main goal of the study is to explore the fundamental physics responsible for the flow and flame oscillations in buoyant IDFs.

2.2 Experimental set-up

In the present work, a co-annular burner consisting of two concentric stainless-steel tubes was built up to generate IDFs, similar to that used by Sidebotham and Glassman

[97]. As shown in Fig. 2.1, the air flow is injected through the central tube with a diameter of 10 mm and a length of 200 mm, and the fuel flow is injected through the annulus between the outer tube and the central tube. The tip of the central tube is sharpened to 0.3 mm thickness to reduce the blockage effect that causes wake. The upper segment of the central tube is encircled by the outer tube, which has an inner diameter of 40 mm, a thickness of 15 mm, and a length of 150 mm. To create a uniform inflow velocity profile for the injecting fuel, the annulus is filled with steel wire gauze and small steel beads which was also adopted by Sidebotham and Glassman [97]. To isolate the flames from the ambient oxygen, a quartz glass tube is installed above the burner to serve as a chimney. The tube has the same diameter as the outer burner tube with a length of 300 mm.

The air flow is supplied by a compressed air tank, which has a capacity of 320 L and a maximum working pressure of 18.9 bar. A central air supply system is used to deliver air to the tank while maintaining pressure. Pure methane (purity 99.9%) stored in Dewar tanks is released to provide the fuel flow. Pressure control valves and flow meters are combined to control and monitor air and fuel flow rates. The laboratory conditions for all the present experiments were 293 K and 101 kPa.

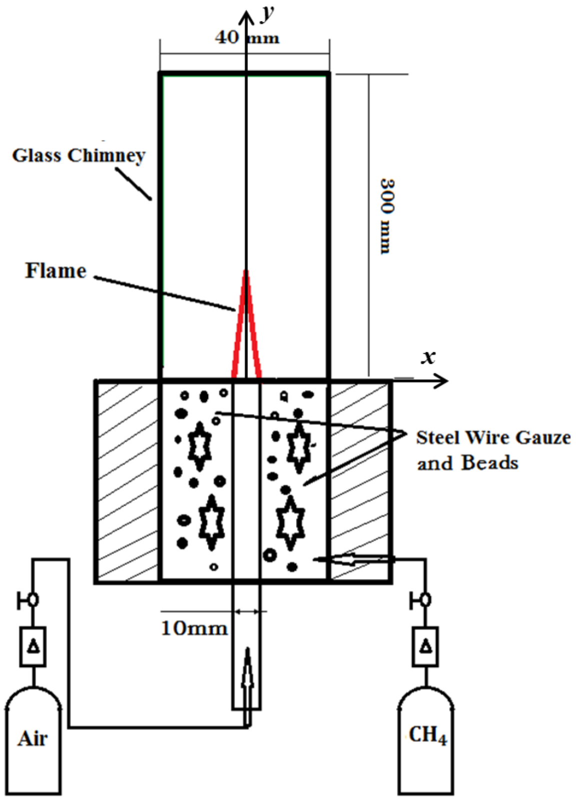

Fig.2.1: Schematic of the burner

PIV measurement was employed to obtain the non-reacting IDF flow field information and hence to validate the present LES results. A schematic of the PIV system is shown in Fig. 2.2, where the IDF burner is mounted vertically. The fuel flow is injected directly into the outer annulus, whereas the air flow is pre-mixed with PIV particles in a separate tank before entering the central air tube. A Quantel dual cavity Nd:Yag laser (EverGreen 600 mJ/pulse, 532 nm wavelength) is used to generate laser pulses at 5 Hz. The point laser beam is transformed into a plane laser sheet through a series of sheet forming optics. By adjusting the angle of the mirror placed above the burner, the laser sheet is aligned with the axis of the burner to enable the flow measurement in the *xy*-plane, as shown in Fig. 2.2. A TSI Incorporated™ 9307-6 aerosol generator is applied to generate olive oil droplets of 1 μm diameter to seed the air flow. The PIV images are captured by a high-speed camera (Hisense 4M, 2048 × 2048 pixels), which is synchronized with a Berkeley Nucleonics Corporation 575 pulse/delay generator, and the time delay between two frames is fixed at 200 μs. The PIV images are processed by the Dantec Dynamic Studio software to obtain the corresponding velocity data.

For visualizing the reacting IDFs, the flow and flame images are captured using a digital camera (Nikon D5200) and a lens (Tamaon 1800mm Macro 1:1). The aperture is adjusted to f5.6 and the IOS value was fixed at 1000 to reduce the interference of external light.

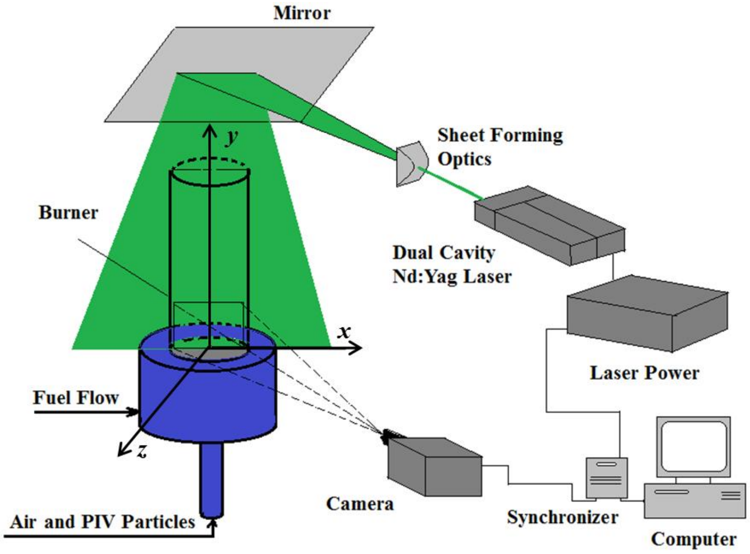

Fig.2.2: Schematic of the PIV system

2.4 Experimental Observations of Flow and Flame Oscillation

The first experimental evidence for oscillation of IDFs was reported by Wu and Essenhigh [96], who found that with sufficiently low fuel velocity the IDFs would become unsteady and start to oscillate. Following their observation, we reproduced a series of oscillating IDFs and present the instantaneous flame images for a representative case in Fig. 2.3. To characterize the air and fuel inlet flows, we defined two Reynolds numbers by

$$Re_i = \frac{\rho_i v_i d_i}{\mu_i},\ Re_o = \frac{\rho_o v_o d_o}{\mu_o}, \tag{1}$$

where ρ, v, and μ are the density, velocity, and viscosity; the subscripts i and o represent the properties for the air and fuel flows; d_i and d_o are the inner diameters of the center air tube and the outer fuel tube. For the IDF in Fig. 2.1, the air inlet velocity is v_i=30cm/s ($Re_i = 192$) and the fuel inlet velocity is v_o=2cm/s ($Re_o = 46$). It is observed that flame oscillation only occurs in the upper portion (i.e. the yellow cap) of the flame, where the direction of the flame tip swings and the height varies, while the blue region at the bottom remains stable.

Fig.2.3: Instantaneous images of an IDF with $Re_\mathrm{i} = 192$ and $Re_\mathrm{o} = 46$.

To understand the source of flame oscillation, we also examined the non-reacting flow characteristics for comparison. Here, the non-reacting flow refers to the one with the same flow conditions as Fig. 2.3 but without ignition. Fig. 2.4 shows the instantaneous vorticity (Ω_z) contour obtained from the PIV measurement for the non-reacting flow. It is seen that the flow is also highly unsteady as the shear layer between fuel and air wiggles and deforms dramatically. Qualitatively, the non-reacting flow seems to be more unstable than the reacting flow as the bottom half of the shear layer also tends to be unsteady. Further justification for this observation will be provided in Sections 5 and 6. In short, based on the instantaneous flame images in Fig. 2.3 and the vorticity Ω_z contours in Fig. 2.4, the flow oscillations in both IDFs and their non-reacting flows are experimentally confirmed.

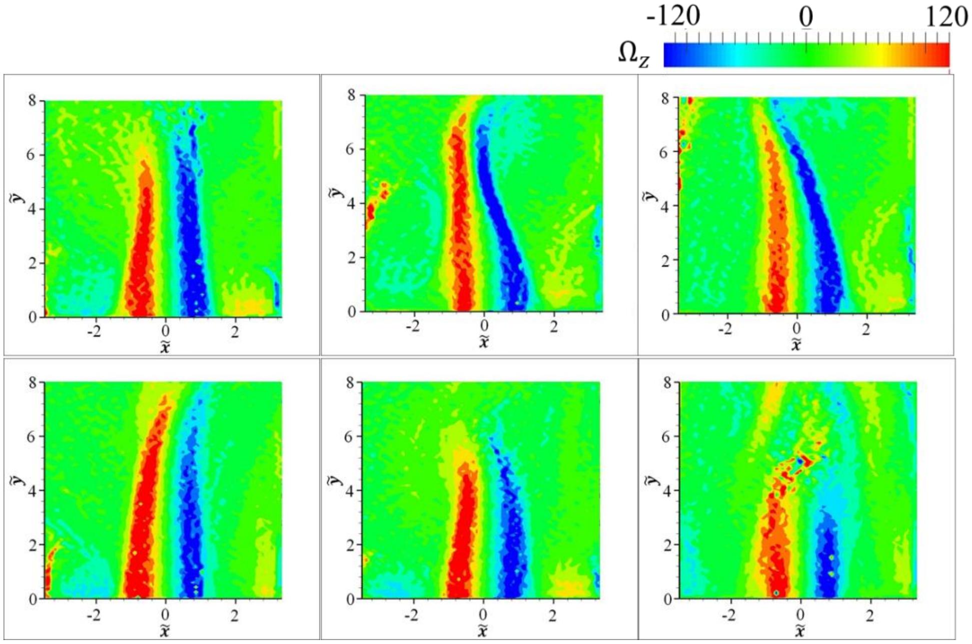

Fig.2.4: Instantaneous vorticity (Ω_z) contours of the non-reacting flow with $Re_i = 192$ and $Re_o = 46$. $\tilde{x} = 2x/d_i$ and $\tilde{y} = 2y/d_i$.

2.3 Numerical Simulation

As turbulence and chemical reaction present together with mass, momentum and heat transfer, the turbulent reacting flow is complex and challenging by nature. In turbulent flows, eddies are distributed into different length scales hence generate kinetic energy of different orders of magnitude. Eddies interact with each other and formation and breaking down is continual in these turbulent flows. Through vortex stretching with the velocity gradients presence, the largest scale eddies mix with and obtain energy from the mean flow and transfer to the smaller ones [98]. Large eddies break up into smaller eddies, which in turn break up into even smaller ones, until the smallest eddies disappear duet to viscous force. This leads to scale invariance of energy transfer in the inertial subrange of turbulence. This concept is known as energy cascade [99, 100]. Based on the energy cascade concept, the turbulent energy is produced by different eddies. Wave number space $E(k)$ is then introduced to evaluate the turbulent kinetic energy $\langle k\rangle$ contribution from different eddies.

$$\langle k\rangle = \frac{1}{2}\langle u_i' u_i'\rangle = \frac{1}{2}(\langle u_1' u_1'\rangle + \langle u_2' u_2'\rangle + \langle u_3' u_3'\rangle) \qquad \textit{(2.1)}$$

$$\langle k\rangle = \frac{1}{2}\langle u_i' u_i'\rangle = \int_0^\infty E(k)dk \qquad (2.2)$$

In Fig. 2.5, the turbulent kinetic energy spectrum is given. Based on how is the kinetic energy produced and dissipated, different subranges are introduced.

1. The energy containing range, in which the largest eddy scales and turbulent kinetic energy density are contained. In this range scale, mean flow effects dominate with the energy transfer from mean flow to turbulence. The characteristic length scale in this range is called the integral length scale (l_t). Eddies with the length scale are considered to provide most of the turbulent kinetic energy [101].
2. The inertial subrange, in which the turbulence spectrum has the largest range. In this range, according to Kolmogorov's theorem [102], small-scale turbulent motions are statistically isotropic with energy transfer rate independent of the molecular viscosity and equal to the dissipation rate.

3. The dissipation range, in which turbulent kinetic energy transfer to the mean flow through viscous effects. In this range, the turbulent kinetic energy per unit wave number holds a dramatic decrement [103]. Turbulent kinetic energy is dissipated into heat with the increase of wave number to lead to the length scale small enough. The smallest turbulent length scale is known as Kolmogorov length scale which is defined by,

$$\eta_k = (\nu^3/\varepsilon)^{1/4} \tag{2.3}$$

The eddy Reynolds number with a velocity fluctuation u_k' yields,

$$Re_k = \frac{u_k'\eta_k}{\nu} = 1 \tag{2.4}$$

In Fig. 2.5, the length scale which divides the inertial subrange from the energy containing range is defined as l_{EI}. l_{EI} approximately equals to one-sixth of integral length scale. l_{DI} is the length scale to separate the dissipation range with the inertial subrange. Normally, $l_{DI} \approx 60\eta_k$ [103].

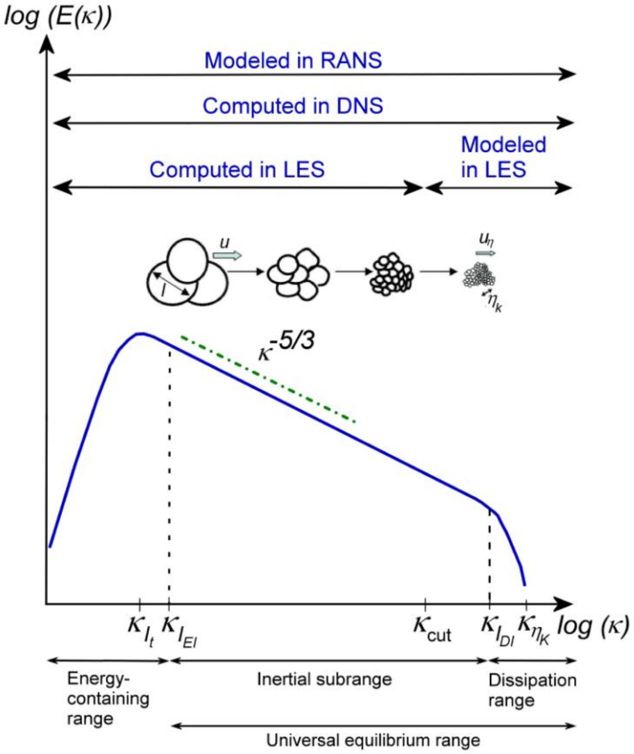

Fig.2.5: Turbulent kinetic energy spectrum, Wave number and the level of characteristic length scales in DNS, RANS and LES (cited from [100]).

In turbulent flow simulation with computational fluid dynamics, the computational mesh size is determined based on the length scales of the flow. When the eddy size is smaller than the mesh size, turbulent models should be introduced. According to the turbulent scales to be resolved, there are three types of methods for the turbulent flow simulation.

1. Reynolds Averaged Navier-Stokes (RANS) Simulation: RANS simulations are based on the averaged motions of the fluid dynamics. In RANS, Reynolds-averaged equations are solved to describe the evolution of the mean quantities. The RANS simulation cost the least computational expense thus being of most interests in engineering applications. The turbulent perturbation terms such as

Reynolds stress, turbulent scar fluxes, et al. are processed through time averaging, space averaging or ensemble averaging. All of the turbulent fluctuations are modeled to close the governing equations. After decades development, a wide range of models can be found such as, $\mathrm{k}-\epsilon$ model [104], $\mathrm{k}-\omega$ [105] and SST models [106]. Despite that RANS simulation is computationally cheap and popular in engineering applications, the instantaneous turbulence information will be totally lost since only averaged information can be obtained. Thus, RANS is not an appropriate approach for high instability flows.

2. Direct Numerical Simulation (DNS): DNS consists in solving Navier-Stokes equations directly, capturing all the scales of fluid motion, with implementation of initial and boundary conditions for the flow studied [99]. DNS is the simplest approach with unrivalled accuracy and level of information of flow field. However, it should be noted that the computational expense is extremely high when Reynolds number is large. And the computational cost increase dramatically with Reynolds number. In DNS, the smallest eddy is resolved which is much smaller than the integral length scale. For a n-dimensions problem, the grid nodes number N required can be given by,

$$N = (\frac{l_t}{\eta_k})^n = Re_t^{\frac{3}{4}n} \tag{2.5}$$

Here, turbulent Reynolds number yields,

$$\mathrm{Re}_t = \frac{u' l_t}{\nu} \tag{2.6}$$

Thus, when the Reynolds number in the practical application is high, DNS is not affordable.

3. Large Eddy Simulation (LES): In LES, the larger three-dimensional unsteady perturbations are directly calculated, whereas the motions in smaller eddies are modeled. The computational expense of LES is an intermediate between RANS and DNS. Through LES, large scale unsteady state flow information can be obtained and it is supposed to be more reliable and accurate thane RANS models in the simulation of highly unsteady problems [99]. To resolve the large eddies and model the smaller eddies, filtering operation is employed by considering a length of a filter [107]. As shown in Fig. 2.5, cut-off wave number for dividing the spectrum of resolved and non-resolved scale is given by,

$$\kappa_{cut} = \frac{\pi}{\bar{\Delta}_e} \tag{2.7}$$

In equ. 2.7, $\bar{\Delta}_e$ is the length scale of the mesh, which is given based on the cell volume by,

$$\bar{\Delta}_e = V_{cell}^{1/3} \tag{2.8}$$

As discussed above, DNS is computationally expensive, and the expense increase as Reynolds number cube, thus DNS is not affordable in most of practical applications due to the high Reynolds number. In most practical applications, large-scale motions are of the most interest, whereas the computational efforts in DNS are mainly spent on the calculation of smallest, dissipative motions. Therefore, compared with DNS, LES with the large-scale information explicitly computed, is much appreciated in practical simulation.

2.3.1 Governing Equations

The governing equations for the present work have made assumptions to simplify the solution of the equation [108]:

- Conserved mass of fluid is.
- Based on Newton's law, the momentum change rate equals to the total forces on a fluid particle.
- The energy change rate equals to the rate of added heat plus the rate of work done on a fluid particle (Law of conservation of energy).

The basic equation can be summarised by the following equations:

1. Mass conservation and species equations

The mass balance for a fluid element or the continuity equation gives that the rate of addition of mass in a fluid particle equals the sum rate of flow of mass into the fluid particle. The mass equation is expressed as:

$$\frac{\partial \rho}{\partial t} + \nabla \cdot (\rho u_i) = 0, \tag{2.9}$$

where, ρ , t and u_i are density, time and velocity vector respectively.

And in reacting flows, the species equation yields,

$$\frac{\partial \rho y_i}{\partial t} + \nabla \cdot (\rho u_i y_i) = -\nabla(\rho \boldsymbol{V}_i y_i) + \rho w_i, \ i = 1, \dots, N_s, \tag{2.10}$$

here, y_i, w_i and $\boldsymbol{V}_i$ are for mass fraction of i species, reaction rate of the ith reaction and the diffusion velocity respectively. The definition of $\boldsymbol{V}_i$ will be shown later.

2. Momentum equation

According to Newton’s second law, the momentum change rate of a fluid element equals the total forces acting on the element. Applying the statement of this law on a fixed control volume, we have momentum equation yields,

$$\frac{\partial(\rho u)}{\partial t} + \nabla\cdot(\rho u_i u_i) = -\nabla p + \nabla\cdot\tau_{i,j} + \rho\sum_i \boldsymbol{f}_i y_{i,} \tag{2.11}$$

where, p is pressure, $\tau_{i,j}$ is viscous stress and $\boldsymbol{f}_i$ is the body force vector.

3. Energy equation

$$\frac{\partial\rho(e+k)}{\partial t} + \nabla\cdot\left(\rho u_i(e+k)\right) = -\nabla\cdot(p u_i) + \nabla\cdot\left(\tau_{i,j}\cdot u_i\right) - \nabla\cdot\boldsymbol{q}$$

$$+\rho\sum_i(\boldsymbol{V}_i + u_i)\boldsymbol{f}_i y_{i.} \tag{2.12}$$

kinetic energy,

$$k = \frac{1}{2}v^2. \tag{2.13}$$

viscous stress is

$$\tau_{i,j} = -\mu\frac{2}{3}(\nabla\cdot u_i)\delta_{i,j} + \mu_B(\nabla\cdot u_i), \tag{2.14}$$

$\delta_{i,j}$ is tensorial Kronecker symbol =1 or 0.

Heat flux:

$$\mathrm{q} = -\kappa\nabla T + \sum_i \rho\boldsymbol{V}_i h_i y_i + \hat{R}T\sum_i\sum_j \frac{x_j D_{T,i}}{M_i D_{ij}}\left(\boldsymbol{V}_i - \boldsymbol{V}_j\right) + \boldsymbol{q}_{R.} \tag{2.15}$$

in RHS of eq. (2.15), the first term is heat conduction, the second is mass diffusion, the third is Dufour effect and the forth is radiation.

To obtain the diffusion velocity $\boldsymbol{V}_i$, one may need the mass diffusion equation in which diffusion velocity is implicitly included. (conf. Law’s book *p*.164 [109])

$$\nabla x_i = \sum_i \frac{x_i x_j}{D_{ij}}\left(\boldsymbol{V}_j - \boldsymbol{V}_i\right) + (y_i - x_i)\frac{\nabla p}{p} + \frac{\rho}{p}\sum_j y_i y_j\left(\boldsymbol{f}_i - \boldsymbol{f}_j\right) + \sum_j \frac{x_i x_j}{\rho D_{ij}}\left(\frac{D_{T,j}}{y_j} - \frac{D_{T,i}}{y_i}\right)\frac{\nabla T}{T} \tag{2.16}$$

In the RHS of eq. (2.16), the first term is Stefan-Maxwell, the second is pressure gradient, the third is body force and the forth is Soret effect.

4. State equation

$$p = \rho \sum_i \frac{y_i}{M_i} \hat{R} T. \tag{2.17}$$

For the N species, one of the N+1 equations which include mass conservation is redundant. So the diffusion velocities and the chemical sources term must satisfy,

$$\sum_i y_i V_i = 0, \qquad \sum_i w_i = 0, \tag{2.18}$$

or one can say, summing the N species equation yields mass equation.

Temperature can be implicitly related to internal energy or enthalpy through,

$$\mathrm{e} = \sum_i y_i e_i T, \qquad h = e + \frac{p}{\rho} = \sum_i y_i h_i T, \tag{2.19}$$

where, e_i and h_i are the species internal energies and enthalpies per unit mass, which for an idea gas are functions of temperature only. Species mole and mass fractions are related by

$$x_i = \frac{y_i/M_i}{\sum_i (y_i/M_i)}, \qquad y_i = \frac{x_i M_i}{\sum_i x_i M_i}. \tag{2.20}$$

To complete the specification of the governing equations, molecular transport, thermochemical, and chemical kinetic property data are needed:

(1) Transport properties: μ (dynamic viscosity); κ (thermal conductivity); D_{ij} (mass diffusivity reflecting diffusion strength between species i and species j $D_{T,j}$ (Temperature dependence of the thermodiffusion coefficient reflecting diffusion strength caused by different temperature gradient, i.e. Soret effect or Ludwig-Soret effect).

(2) Thermochemical data: h_i and M_i.

(3) Chemical kinetic properties: considering Arrhenius law, $k(T) = BT^{\alpha}e^{-E_a/R^0T}$, the E_a, B, α and species concentration, temperature, and pressure is required to calculate the chemical source term w_i.

To derive the LES of turbulent combustion, some assumptions are needed. In the present project, “low Mach number assumption” will be applied which may leads to the following phenomena be neglected,

a) Acoustic interaction and compressibility,

b) Bulk viscosity,

With the simplification, the governing equations will be written as follows,

Mass:

$$\frac{\partial \rho}{\partial t} + \nabla \cdot (\rho u_i) = 0 \qquad (2.21)$$

Momentum:

$$\frac{\partial (\rho \boldsymbol{u})}{\partial t} + \nabla \cdot (\rho u_i u_i) = -\nabla p + \nabla \cdot \tau_{i,j} + \rho g_i \qquad (2.22)$$

Chemical species:

$$\frac{\partial \rho y_k}{\partial t} + \nabla \cdot (\rho u_i y_k) = -\nabla \cdot \left(\rho V_{i,k} y_k\right) + w_k,\ k = 1, \dots, N_s \qquad (2.23)$$

Energy:

$$\frac{\partial \rho h_s}{\partial t} + \nabla \cdot (\rho u_i h_s) = \frac{Dp}{Dt} + \tau_{i,j}\nabla \cdot (u_i) + \nabla \cdot (\kappa \nabla T) - \nabla \cdot \left(\rho \sum_{k=1}^{N} V_{i,k} y_k h_{s,k}\right) + \omega_T,$$

$$\text{s=1,2,3…} \qquad (2.24)$$

If a general variable equation is introduced, the conservative form of all the fluid flow equation can be written in the following form:

$$\frac{\partial \rho \phi_k}{\partial t} + \nabla \cdot (\rho \boldsymbol{u} \phi_k) = -\nabla \cdot (p \alpha_k \nabla \phi_k) + \omega_{\phi},\ \ \text{k=1,2,3…} \qquad (2.25)$$

State relation,

$$\rho = f(\phi_1, \phi_2, \dots) \tag{2.26}$$

2.3.2 Favre Average

In the Reynolds turbulent flow concept, any quantity f was split into a mean $\overline{f},$ and a fluctuating, f' component ($f = f' + \bar{f}$). Using this procedure with the mass conservation Eq. (2.9) leads to:

$$\frac{\partial \bar{\rho}}{\partial t} + \nabla \cdot (\overline{\rho u_\iota}) = \nabla \bar{\rho} + \nabla \cdot (\bar{\rho}\bar{u}_\iota + \overline{\rho' u_\iota'}) = 0 \tag{2.27}$$

where the unclosed quantity $\overline{\rho' u_\iota'}$ corresponding to the correlation between density and velocity fluctuations appears and requires modeling. By using Reynolds average in variable density flows, many other unclosed relations between any quantity f and density fluctuations $\overline{\rho' f'}$ will be introduced. To avoid this difficulty, mass-weighted averages (called Favre averages) are usually preferred.

By introducing a density weighted average ũ, called the Favre average, which is more convenient than Reynolds average. For instance, the average of the product of the density with the two velocity components would lead with four terms,

$$\overline{\rho u v} = \overline{(\bar{\rho} + \rho')(\bar{u} + u')(\bar{v} + v')} = \bar{\rho}\bar{u}\bar{v} + \bar{\rho}\overline{u'v'} + \bar{u}\overline{\rho' v'} + \bar{v}\overline{\rho' u'} + \overline{\rho' u' v'}.$$

Whereas, the Favre average leads to,

$$\overline{\rho u v} = \bar{\rho}(\bar{u} + \widetilde{u')(\bar{v}} + v') = \bar{\rho}\tilde{u}\tilde{v} + \bar{\rho}u\widetilde{'v}',$$

2.3.3 Favre Averaged Governing Equations

Mass:

$$\frac{\partial \bar{\rho}}{\partial t} + \nabla \cdot (\bar{\rho}\widetilde{u_\iota}) = 0. \tag{2.28}$$

Momentum:

$$\frac{\partial(\bar{\rho}\widetilde{\boldsymbol{u}_\imath})}{\partial t}+\nabla\cdot\left(\bar{\rho}\widetilde{u_\imath}\widetilde{u_\jmath}\right)=-\nabla\bar{p}+\nabla\cdot\left(\bar{\tau}_{i,j}-\bar{\rho}\widetilde{u_\imath''u_\jmath''}\right)+\bar{\rho}g_i. \tag{2.29}$$

Chemical species:

$$\frac{\partial(\bar{\rho}\widetilde{\mathrm{y_k}})}{\partial \mathrm{t}}+\nabla\cdot(\bar{\rho}\widetilde{u_\imath}\widetilde{\mathrm{y_k}})=-\nabla\cdot\left(\overline{\boldsymbol{V}_{\imath,\jmath}y_k}+\bar{\rho}\widetilde{u_\imath''y_k''}\right)+\overline{\mathrm{w_k}},\ \ \mathrm{k}=1,\dots,\mathrm{N_s} \tag{2.30}$$

Energy:

$$\frac{\partial\bar{\rho}\widetilde{h_s}}{\partial t}+\nabla\cdot\left(\bar{\rho}\widetilde{u_\imath}\widetilde{h_s}\right)=\ \frac{\overline{Dp}}{Dt}+\overline{\tau_{\imath,\jmath}\nabla\cdot(u_\imath)}+\nabla\cdot\left(\overline{\lambda\nabla T}-\overline{\rho u_s''h_s''}\right)$$

$$-\nabla\cdot\left(\overline{\rho\textstyle\sum_{k=1}^{N}V_{k,\imath}y_k h_{s,k}}\right)+\overline{\omega_T},\qquad s=1,\dots,N \tag{2.31}$$

where

$$\frac{\overline{Dp}}{Dt}=\frac{\partial p}{\partial t}+\widetilde{u_\imath}\frac{\partial\bar{p}}{\partial x_i}+\overline{u_\imath''\frac{\partial p}{\partial x_\imath}}. \tag{2.32}$$

General transport equation:

$$\frac{\partial\bar{\rho}\tilde{\phi}_k}{\partial t}+\nabla\cdot\left(\bar{\rho}\widetilde{u_\jmath}\tilde{\phi}_i\right)=\nabla\cdot(\overline{\rho a_\imath\nabla\phi_\imath}-\bar{\rho}\widetilde{u_\jmath''\phi_\imath''})+\widetilde{\omega}_k\quad \text{k=1,2,3…} \tag{2.33}$$

State relation:

$$\bar{\rho}=\overline{f(\phi_1,\phi_2,\dots)}. \tag{2.34}$$

2.3.4 Filtering and Filtered Governing Equations

In LES, the filtering for variables are based on spectral space (e.g. the variables larger than a known cut-off frequency are blocked) or in physical space (weighted average over a given volume). The filtered quantity f is defined as:

$$\bar{f}(x)=\int f(x')F(x-x')dx', \tag{2.35}$$

where F is the LES filter and there are several filters are available. For example, the simplest one cut-off filter,

$$F(k) = \begin{cases} 1 & if\ k \leq k_c = \pi/\Delta \\ 0 & otherwise \end{cases}, \tag{2.36}$$

where k is the spatial wave number. This filter keeps length scales greater than the cut-off length scale 2Δ, where Δ is the filter size. As the result of filtering, the large scale with order of magnitude of 2Δ will be solved directly in the governing equations and the unresolved part will be modeled.

For variable density flows, we use a mass-weighted method to filter the quantity which is given by,

$$\bar{\rho}\bar{f}(x) = \int \rho f(x')F(x - x')dx'. \tag{2.37}$$

where $\bar{f}$ is filtered or resolved quantity, whereas $f' = f - \bar{f}$ corresponds to the unresolved part (i.e. the subgrid scale component, attributed to the unresolved flow motions). This operation should be carefully conducted:

- Contrary to RANS averaging, the filtering of the LES perturbation will result in a non-zero value, i.e. $\overline{f'} \neq 0$. After filtering, the two values are not equals to each other namely: $\bar{f} \neq \bar{\bar{f}}$. which is also yields the relation: $f = \tilde{f} + f''$, $\widetilde{f''} \neq 0$ and $\tilde{f} \neq \tilde{\tilde{f}}$.
- For the derivation of equations for the filtered quantities $\tilde{f}$ or $\bar{f}$, replacement of filter and derivative operators is necessary. This exchange is valid only under restricted assumptions and is wrong, for instance, when the filter size or the node size for simulation, changes with spatial location.

Filtered balance equations

Mass:

$$\frac{\partial \bar{\rho}}{\partial t} + \nabla \cdot (\bar{\rho}\widetilde{u_i}) = 0. \tag{2.38}$$

Momentum:

$$\frac{\partial(\bar{\rho}\boldsymbol{\widetilde{u_\imath}})}{\partial t} + \nabla\cdot(\bar{\rho}\widetilde{u}_\imath\widetilde{u}_\jmath) = -\nabla\bar{p} + \nabla\cdot\left[\bar{\tau}_{i,j} - \bar{\rho}\left(\widetilde{u_\imath u_\jmath} - \widetilde{u}_\imath\widetilde{u}_\jmath\right] + \bar{\rho}g_i. \tag{2.39}$$

Chemical species:

$$\frac{\partial(\bar{\rho}\widetilde{y_k})}{\partial t} + \nabla\cdot(\bar{\rho}\widetilde{u}_\imath\widetilde{y_k}) = \nabla\cdot\left(\overline{V_{\imath,\jmath}y_k} - \bar{\rho}(\widetilde{u_\imath y_k} - \widetilde{u}_\imath\widetilde{y_k})\right) + \overline{w_k},\ k = 1, \ldots, N_s \tag{2.39}$$

Energy:

$$\frac{\partial\bar{\rho}\widetilde{h_s}}{\partial t} + \nabla\cdot\left(\bar{\rho}\widetilde{u}_\imath\widetilde{h_s}\right) = \frac{\overline{Dp}}{Dt} + \overline{\tau_{\imath,\jmath}\nabla\cdot(u_\imath)} + \nabla\cdot\left(\overline{\lambda\nabla T} - \bar{\rho}(\widetilde{u_\imath h_s} - \widetilde{u}_\imath\widetilde{h_s})\right)$$

$$-\nabla\cdot\left(\overline{\rho\sum_{k=1}^{N} V_{k,\imath}y_k h_{s,k}}\right) + \overline{\omega_T}, \qquad s = 1, \ldots \tag{2.40}$$

where

$$\frac{\overline{Dp}}{Dt} = \frac{\partial\bar{p}}{\partial t} + +\overline{u_\imath\frac{\partial p}{\partial x_\imath}}. \tag{2.41}$$

State relation:

$$\bar{\rho} = \overline{f(\phi_1, \phi_2, \ldots)}. \tag{2.42}$$

Unresolved Reynolds stresses $t_{i,j} = \bar{\rho}(\widetilde{u_\imath u_\jmath} - \widetilde{u}_\imath\widetilde{u}_\jmath)$, requiring a subgrid scale turbulence model. Due to its simpleness and convenience, Smagorinsky model is welcomed in LES. Based on Boussinesq assumption, the unresolved momentum fluxes can be expressed as:

$$t_{i,j} = -\bar{\rho}\widetilde{u_\imath u_\jmath} + \bar{\rho}\tilde{u}_i\tilde{u}_j = 2\mu_t\tilde{S}_{i,j} - \frac{1}{3}\bar{\rho}t_{k,k}\delta_{i,j}. \tag{2.43}$$

where $\tilde{S}_{i,j} = \frac{1}{2}\left(\frac{\partial\tilde{u}_i}{\partial x_j} + \frac{\partial\tilde{u}_j}{\partial x_i}\right) - \frac{1}{3}\delta_{i,j}\frac{\partial\tilde{u}_k}{\partial x_k}$. The eddy viscosity is given by Smagorinsky model,

$$\mu_t = C_\mu\bar{\rho}\Delta^2|\tilde{S}|, \tag{2.44}$$

where $\tilde{S} = \sqrt{\tilde{S}_{i,j}\tilde{S}_{i,j}}$, Δ is the filter width. The subgrid kinetic energy is modeled by using,

$$\bar{\rho}t_{k,k} = C_k\bar{\rho}\Delta^2|\tilde{S}|^2. \tag{2.45}$$

C_μ, C_k can be obtained by dynamic procedure. To this stage, the momentum equation is closed.

Unresolved species fluxes $\bar{\rho}(\widetilde{u_\imath y_k} - \widetilde{u_\imath}\widetilde{y_k})$ and **enthalpy fluxes** $\bar{\rho}(\widetilde{u_\imath h_s} - \widetilde{u_\imath}\widetilde{h_s})$. with a gradient-diffusion assumption,

$$q_{ik} = -\bar{\rho}\widetilde{u_k \phi_\imath} + \bar{\rho}\widetilde{u_k}\widetilde{\phi_\imath} = \bar{\rho}\alpha_t \nabla \widetilde{\phi_\imath}, \tag{2.46}$$

where the eddy diffusivity is given,

$$\bar{\rho}\alpha_t = C_\alpha \bar{\rho}\Delta^2 |\tilde{\mathrm{S}}|. \tag{2.47}$$

C_α can be obtained by dynamic procedure.

There is another idea in Peters' book to handle the q_{ik}. (cf. Peters' book P. 31[44]). That approach of derivation will not be discussed here. The main idea is based on analysis of dimension and order of magnitude.

Filtered laminar diffusion fluxes for species and enthalpy. As in RANS, these molecular fluxes may either vanish or be modeled by a simplified gradient assumption like:

$$\overline{V_{\imath,\jmath} y_k} = -\bar{\rho}\overline{D_k}\frac{\partial \widetilde{y_k}}{\partial x_i} \text{ and } \overline{\lambda \frac{\partial T}{\partial x_\imath}} = \bar{\lambda}\frac{\partial \tilde{T}}{\partial x_i}. \tag{2.48}$$

Filtered chemical reaction rate $\overline{\mathrm{w_k}}$, which will be talked later.

The pressure velocity term $\overline{\mathrm{u_\imath}\frac{\partial \mathrm{p}}{\partial \mathrm{x_\imath}}}$ is usually approximated by $\mathrm{u_i}(\frac{\partial \bar{\mathrm{p}}}{\partial \mathrm{x_i}})$.

So far, there is only one nonlinear term in scalar balance equation, i.e. the chemical reaction source term $\bar{\rho}\widetilde{\omega}_\mathrm{k}$ which will be discussed later.

2.3.5 Chemical Reaction

In the present work, the focus is on the analysis the mechanism of the dynamics in the flow field not the IDF structure and Reynolds number is relative small. The one step irreversible infinite fast chemistry is employed to handle the chemical reaction term. Consider a reaction involves fuel (F), oxidizer (O) and products (P), we have,

$$v_F F + v_o \leftrightarrow v_p P \tag{2.49}$$

Thus, for single step reaction problems, the species reaction rate w_k is given as,

$$w_k = W_k v_k Q \tag{2.50}$$

Similarly, the reaction rate for temperature is also can be expressed as,

$$w_T = -w_F Q \tag{2.51}$$

In the assumption of irreversible infinite fast chemistry [55],

- Infinite fast denotes that the chemistry is infinitely fast, i.e. compare with flow time scale or diffusion time scale, chemical time scale is much shorter. This assumption indicate that chemical reactions proceed locally fast enough to reach equilibrium immediately.
- The reaction 2.50 only proceeds from left to right.

2.3.6 Computational Details and Validation

Large eddy simulation (LES), with its advantage in capturing unsteady flow motion and relatively cheap computational expense compared to Direct Numerical Simulation (DNS), was implemented through the open source code OpenFOAM (version 2.3.0) in the present work [110]. Pressure and momentum correctors were combined with the Pressure Implicit with the Splitting of Operators (PISO) method [111] to solve the time-dependent Navier-Stokes equations. The discretization of unsteady terms was performed using a second order backward scheme [112]. The Normalized Variable Diagram (NVD) scheme (Gamma differencing scheme) [113, 114] and the second order central difference scheme were used to discretize the convection and diffusion terms. Second order central difference linear interpolation was applied for mass flux calculation. The time step was constrained by the Courant-Friedrichs-Lewy (CFL) number for stable simulation. The infinitely fast and irreversible chemical reaction scheme suffices to investigate the present problem.

The 3D computational domain and mesh are shown in Fig. 2.6. Local refinement was performed to accurately resolve the unsteady flow near the center of the burner. The mesh in Fig. 2.6 contains 0.5 million grid nodes with all mesh edge size in the range of $0.01d_i - 0.12d_i$. Tab. 2.1 illustrates the boundary conditions for the benchmark reacting case presented in Fig. 2.6. To determine the temperature boundary condition on the side wall, the temperature at different vertical locations of the glass tube was measured experimentally. As the standard deviation is only about 37K, the averaged value of 450K was used in the present simulation for simplicity.

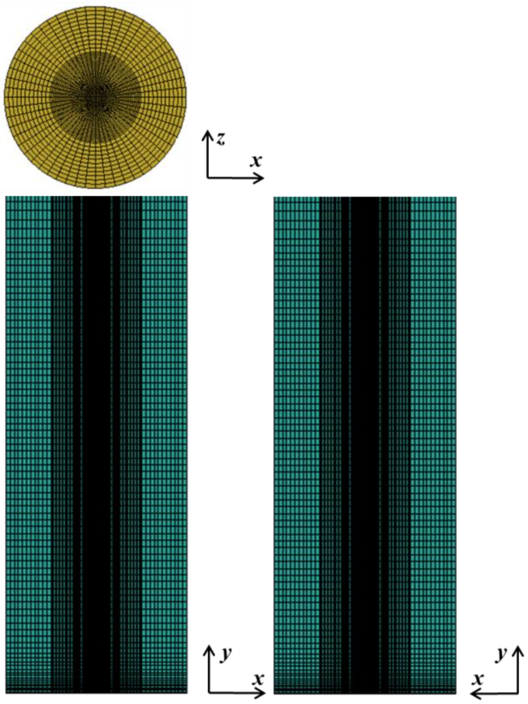

Fig.2.6: Computational mesh for the simulation.

Table2.1: Boundary conditions for the benchmark case.

	Velocity (m/s)	Pressure (Pa)	Temperature (K)	Components (-)
Air inlet	0.3	Zero Gradient	300	100% air
Fuel inlet	0.02	Zero Gradient	300	100% Methane
Outlet	Zero Gradient	101325	Zero Gradient	Zero Gradient
Glass chimney	0	Zero Gradient	450	Zero Gradient

The non-reacting flow presented in Fig. 2.3 was adopted as a benchmark case to validate the present LES. Fig. 2.7 presents the normalized time-averaged streamwise velocity as a function of span-wise coordinate at different streamwise locations, where $\widetilde{U}_y = U_y/v_i$ with U_y being the streamwise velocity and $v_i = 30\text{cm/s}$. It is seen that the simulation results are in good agreement with experiment, suggesting that the adopted flow solver together with the simulation set-up is capable of predicting the non-reacting flow field. Moreover, the convergence of the simulation results of different meshes confirms that the grid resolution of Cal.0.5M is sufficient for the non-reacting case.

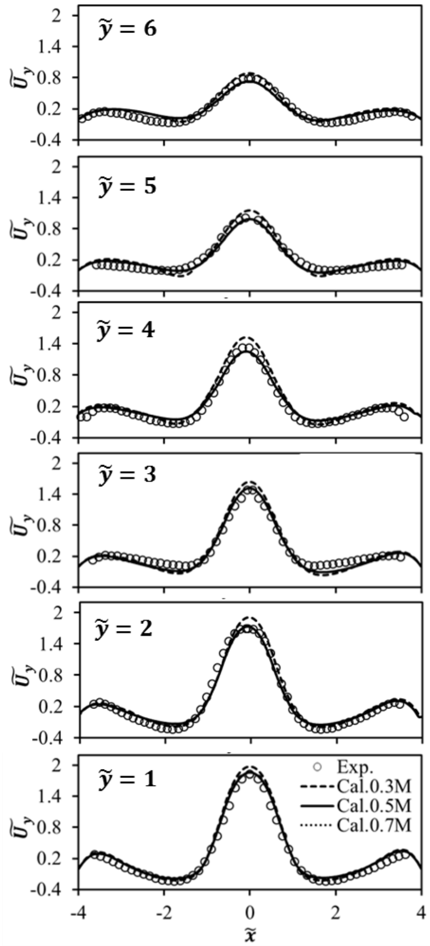

Fig.2.7: Validation of time-averaged streamwise velocity at different axial locations and grid independence analysis for the benchmark case. Cal.0.3M, Cal.0.5M, and Cal.0.7M denote the simulation results with 0.3million, 0.5 million, and 0.7 million grid nodes, respectively.

For the corresponding IDF flow shown in Fig. 2.3, the validation and the grid-dependence analysis of the present LES is unavailable because of the lack of velocity measurement. We however noted that the Reynolds number decreases due to heat release hence a larger turbulence length scale (~$Re^{-1/2}$)[115] is expected. Consequently, the mesh for the non-reacting flow is sufficiently fine for its corresponding reacting flow, and thus the mesh with 0.5 million were used for the simulation of IDFs.

Considering the flame height is one of the most important flame characteristics of a non-premixed flame [18, 116-118], we validated the present LES of IDF by comparing the calculated flame height with the experimental value, as shown in Fig. 2.8. According to Mikofski et al. [93], the edge of the blue flame approximates the reaction zone of methane IDFs, where massive heat is released to cause a local peak of temperature. In this respect, the outer boundary of the blue flame on the left side of Fig. 2.8 approximately matches with the ridge of the temperature contour on the right, verifying the good agreement between simulation and experiment.

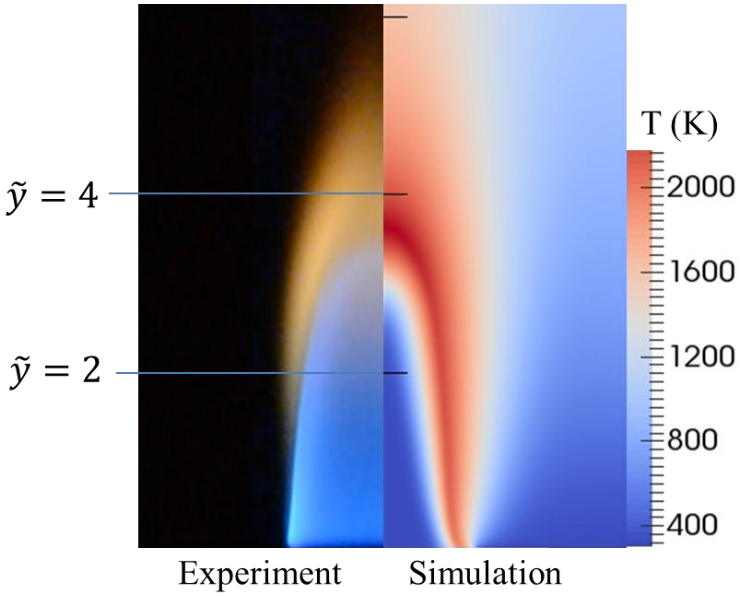

Fig.2.8: Comparison of flame height between experiment and simulation for the benchmark case of IDF.

2.4 Results and Discussion

In the researched IDFs of the present work, with presence of the density difference between inner air flow and outer fuel flow combined with buoyance effect, flow oscillation was observed both in experiments and simulation. The main goal is to identify the mechanism of the oscillation and which factors control the oscillation intensity. To achieve the goal, both non-reacting and reacting IDFs with a wide range of conditions were examined experimentally and numerically.

As an initial step of the analysis of the flow dynamics in IDFs, research of non-reacting flow is necessary. Compared with reacting flows, interaction between chemical reaction and fluid dynamics is isolated in the non-reacting flow. The unsteady pure flow motions and fuel/air mixing information can be obtained to support the analysis of the complicated reacting flows dynamics. Moreover, the non-reacting flow helps to understand the basic mechanisms associated with different regimes of flow instability. In the present IDFs, Reynolds number is relatively low thus the flow motions are mainly in large scale and the flow perturbation is typically not so strong.

2.4.1 Instability in Non-reacting Flows

In a previous study, Jiang and Luo [67] have demonstrated that the buoyancy-induced vorticity formation owing to the interaction between gravity and horizontal density gradient is the main cause of the flow instability in reacting plumes. Noting that the same mechanism also exists in non-reacting plume with horizontal density gradient and to promote the understanding of flame oscillation in IDF, we started with analyzing the oscillation of a non-reacting flow in the IDF configuration.

For the present axisymmetric incompressible flow, the vorticity transport equation can be expressed in the non-dimensional form by

$$\frac{D\boldsymbol{\omega}}{Dt} = \frac{\rho_a d_i}{\rho^2 {u_{ref}}^2}(\boldsymbol{\nabla}\rho \times \boldsymbol{g}) + Re^{-1}\boldsymbol{\nabla}^{\mathbf{2}}\boldsymbol{\omega}, \tag{2.52}$$

where ρ_a is the gas density of the ambient environment, ρ is the local gas density, $\boldsymbol{g}$ is the gravitational acceleration, d_i is the diameter of the center air tube, and u_{ref} is a reference velocity. In Eq. 2.52, the second term quantifies the vorticity diffusion, which does not generate new vorticity but only changes the vorticity distribution of the existing flow. Thus, the true source of vorticity is the first term, which produces non-zero vorticity by the non-parallel vertical gravity and horizontal density gradients. We further realized that the strength (γ) of a shear layer can be obtained by integrating vorticity along the normal direction (n) of the shear layer as $\gamma = \int \omega \mathrm{d}n$. Thus, the total change of strength of the buoyancy-induced shear layer (γ_B) can be calculated by integrating Eq. 2.52 as

$$\frac{\mathrm{d}\gamma_B}{\mathrm{d}t} = \int_0^{d_o/2} \frac{D\omega}{Dt}\mathrm{d}r = \int_{\rho_i}^{\rho_o} \frac{-\rho_a g d_i}{\rho^2 {u_{ref}}^2}\mathrm{d}\rho = \frac{\rho_a g d_i}{{u_{ref}}^2}\left(\frac{1}{\rho_o} - \frac{1}{\rho_i}\right). \tag{2.53}$$

Here, the derivation of Eq. 2.53 requires zero contribution from the vorticity diffusion term, $Re^{-1}\boldsymbol{\nabla}^{\mathbf{2}}\boldsymbol{\omega}$. Since the net effect of this term is the redistribution of vorticity, we only need $\boldsymbol{\nabla\omega} = \mathbf{0}$ at the boundary of the shear layer γ_B so that no external vorticity enters the vortex. This condition is readily satisfied for any individual vorticial structure (γ_B included), for which vorticity gradually vanishes at the boundary. At this point, it is interesting to note that the result of Eq. 2.53 can be interpreted as a special Richardson number (Ri) defined by

$$Ri = \frac{(\rho_i - \rho_o) g d_i}{\bar{\rho} {u_{ref}}^2}, \tag{2.54}$$

where $\bar{\rho} = \frac{\rho_i \rho_o}{\rho_a}$. To quantify the vorticity generation inside the shear layer, we can formulate the reference velocity by $u_{ref} = v_o - v_i$, which equals the strength of the initial shear layer at the inlet. Consequently, the Richardson number defined in Eq. 2.54 measures the buoyancy-induced vorticity generation compared to the strength of the initial shear layer.

To examine the influence of Ri on flow instability of the non-reacting flow concerned, we simulated five different cases with varying buoyancy term but fixed initial shear term. The buoyancy term was changed by diluting the fuel flow with 0%-100% air, so the density ratio between the air stream and the diluted fuel stream could be adjusted between 1.8 and 1.0, hence the *Ri* varying from 0.95 to 0 accordingly. Fig. 2.9 shows the instantaneous vorticity (Ω_z) contours in the *xy*-plane (bottom) and the *xz*-plane (top) at the axial location of $\tilde{y} = 6$. It is observed that flow in *xy*-plane becomes more unstable as *Ri* increases from 0 to 0.95. Specifically, the initial shear layer between fuel and air tends to lose its stability and starts to oscillate in the near-field, under the influence of an external shear layer as the buoyancy effect becomes more prominent.

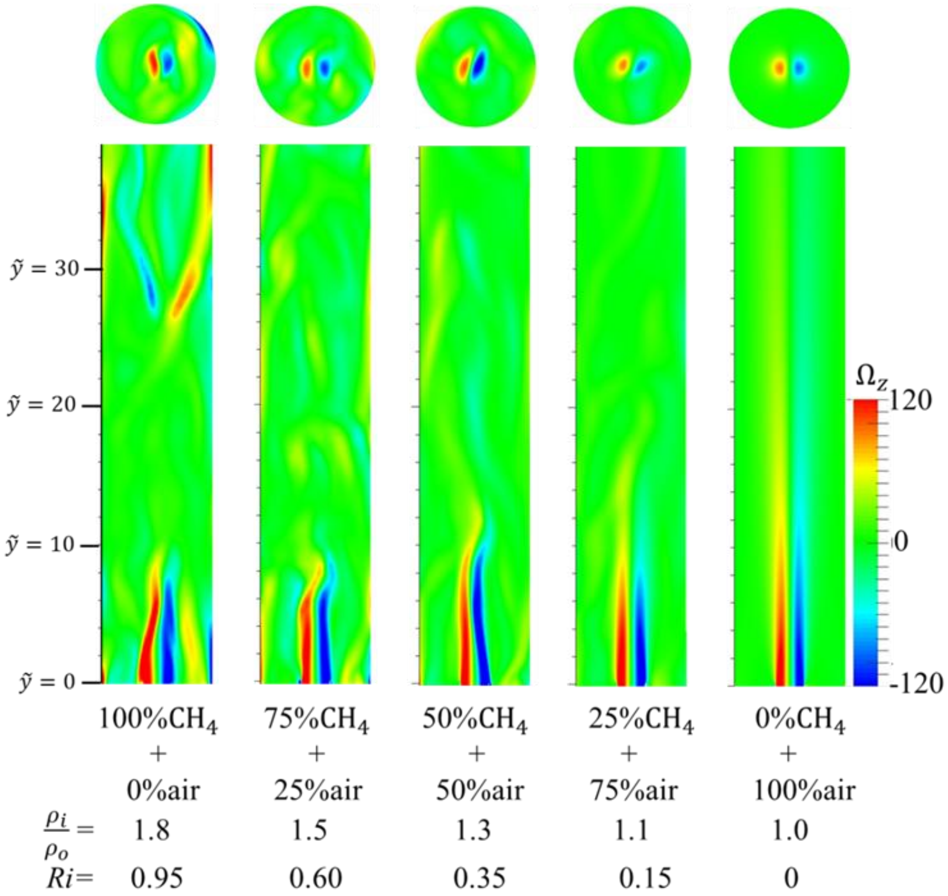

Fig.2.9: Instantaneous vorticity (Ω_z) contours in the *xy*-plane (bottom) and the *xz*-plane (top) at $\tilde{y} = 6$. The Richardson number is adjusted by varying the air/fuel density ratio. The first plot corresponds to the benchmark case introduced before

Alternatively, *Ri* can be adjusted by fixing the buoyancy term while varying the initial shear term. This was done by changing v_o so that *Ri* varies in the range between 0.95 and infinity. Again, in this scenario we simulated five different non-reacting IDF flows and presented their instantaneous vorticity contours in Fig. 2.10. It is seen that the shear flows and vortical structures in the near-field all display significant unsteady features for the cases of *Ri* = 0.95, 1.19, and 1.86. As the Richardson number further increases to *Ri* = 7.44, the flow structures in the near filed tend to become relatively stable. When *Ri* further increases to infinity, the shear layers in the near-field grow into a symmetric steady pattern, indicating the establishment of a stable flow.

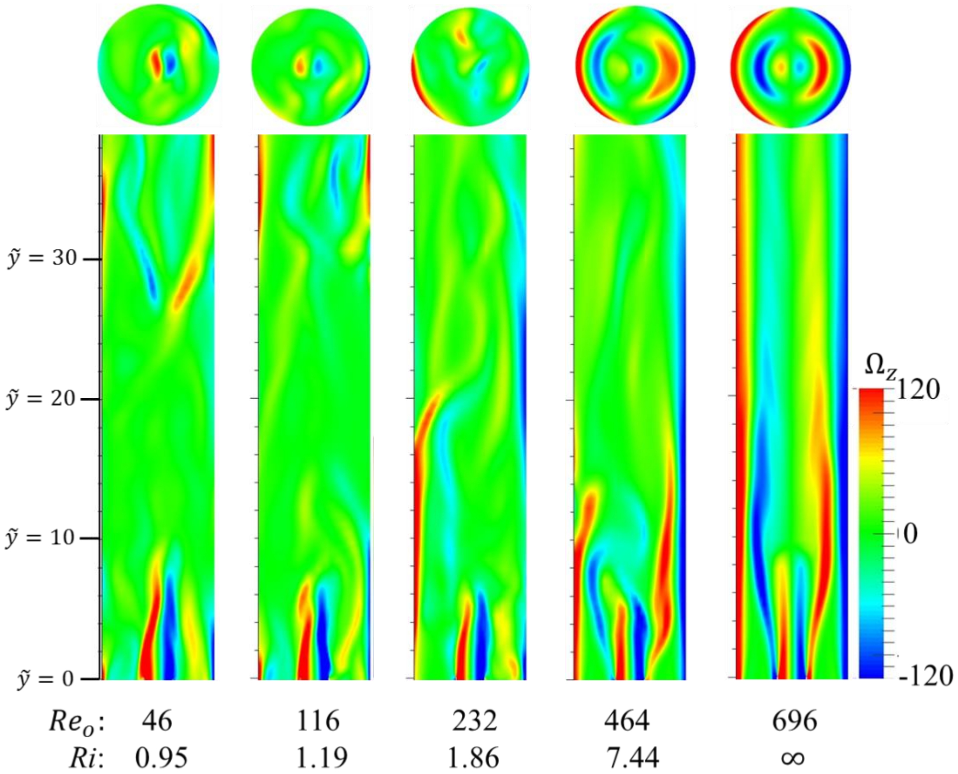

Fig.2.10: Instantaneous vorticity (Ω_z) contours in the *xy*-plane (bottom) and the *xz*-plane (top) at $\tilde{y} = 6$. *Ri* is adjusted by varying the initial shear term through Re_o while fixing the buoyancy term. The first plot corresponds to the benchmark case introduced before.

It has been seen that increasing *Ri* from zero to infinity would cause the stable near-field flow to become unstable and then stable. This non-monotonic influence of *Ri* on flow stability of the non-reacting IDFs can be quantitatively supported by Fig. 2.11, where the time averaged streamwise turbulent kinetic energy, $\frac{1}{2}{U_y}'^2$, is plotted as a function of axial location in the near-field for different *Ri*. We indeed observed that the unsteadiness of the flow is the strongest as *Ri* approaches 1.

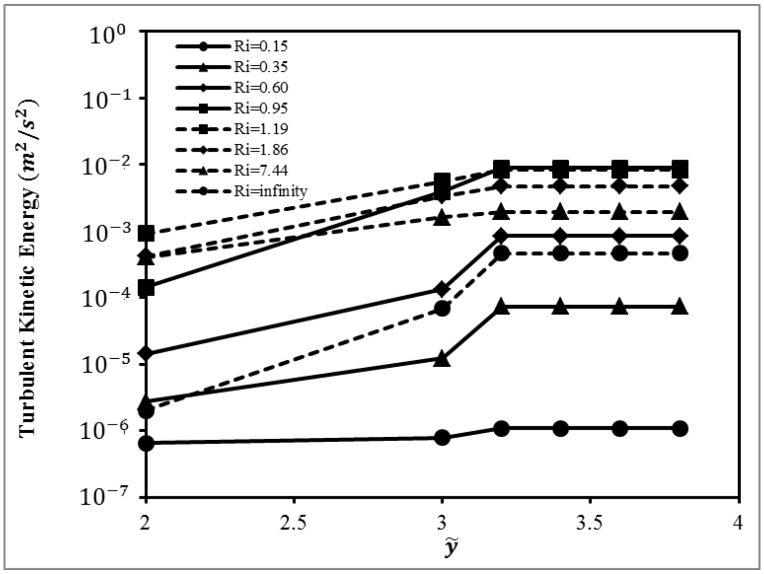

Fig.2.11: Time-averaged turbulent kinetic energy, $\frac{1}{2}{U_y{}'}^2$ at different axial locations for different Ri.

To understand the non-monotonic effect of Ri on the stability of non-reacting IDF flows, we can further unravel the physical meanings of the two contributing terms of Ri. According to Eqs. 2.53 and 2.54, the buoyancy-effect term produces a vorticity proportional to $\boldsymbol{\nabla}\rho \times \boldsymbol{g}$. For non-reacting flows, the density gradient $\boldsymbol{\nabla}\rho$ is caused by the different densities between fuel and air. It is note that the vorticity in the initial shear flow is given by $\Omega_z = \left(\frac{\partial U_y}{\partial x} - \frac{\partial U_x}{\partial y}\right)\vec{k} \approx (\frac{\partial U_y}{\partial x})\vec{k}$. For the present problem, we have $\rho_i > \rho_o$ and $v_i > v_o$, which dictates that $(\frac{\partial U_y}{\partial x})\vec{k}$ and $\boldsymbol{\nabla}\rho \times \boldsymbol{g}$ are always of opposite directions, as illustrated in the schematic of Fig. 2.12. This is partially supported by the cases with $Ri \neq 0$ in Figs. 2.9 and 2.10, where external shear layers grow outside of the initial shear layers with opposite-direction vorticity. We note that this opposite-direction shear layer configuration much resembles that for the von Karman vortex street. To this end, the buoyancy-induced shear flow and the initial shear flow are two competing mechanisms in the near-field of a non-reacting IDF flow. It is important to note that the dominance of either of the mechanisms (*Ri* being either very small or very large) would promote flow stabilization in the near-field, although instability could still develop in the far field as the nature of the dominant shear flow evolves from laminar to turbulent. However, if the two effects are comparable to each other (*Ri* approaches 1), instability would develop immediately from the near-field because of the strong interaction between vortices with comparable strengths but of opposite signs. This explains why the near-field instability of a non-reacting IDF is most significant near *Ri* = 1.

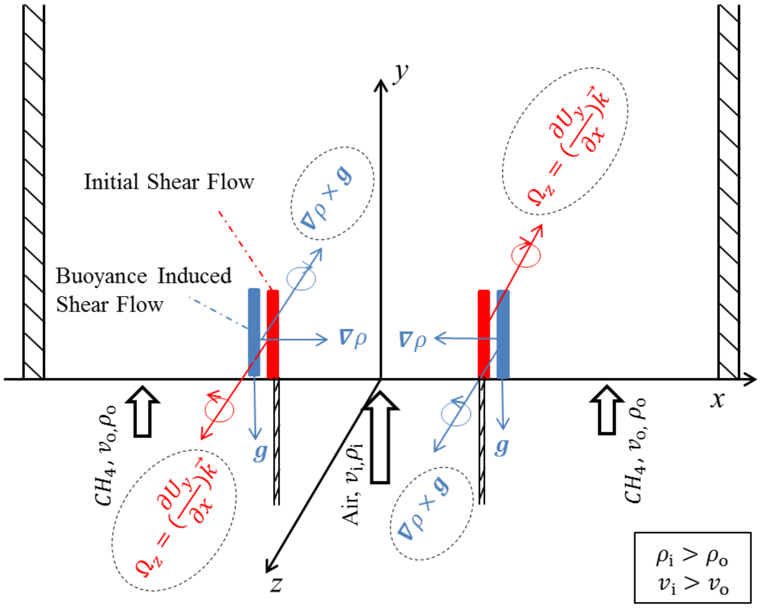

Fig.2.12: Schematic of the relation between the initial shear flow and the buoyancy-induced shear flow in the near-field of a non-reacting IDF flow.

Realizing that both the buoyancy-induced vorticity generation and the initial shear flow are not unique to a non-reacting IDF flow, we were inspired to extend the above understanding of flow instability to non-reacting NDF flows. A non-reacting NDF flow was simulated by injecting fuel flow through the center tube with a velocity of 30 cm/s and air flow through the annular with a velocity of 2 cm/s, so that the air/fuel configuration is exactly opposite of the benchmark case presented in Figs. 2.9 and 2.10. In this case, the initial shear flow is identical to the non-reacting IDF flow, and so is the magnitude of the density gradient. However, the notable difference is the direction of the density gradient and consequently the direction of the buoyancy-induced vorticity. The outcome of the difference is that the initial shear flow would be enhanced by the buoyancy-induced vorticity generation in the non-reacting NDF flow, instead of being counteracted in the non-reacting IDF flow. In this case, the growing initial shear layer would remain stable in the near field, until it reaches certain critical Reynolds number and develops Kelvin-Helmholtz instability in the far field. This is indeed verified in Fig. 2.13 by the stable and growing shear flow of the NDF. The streamline plots in Fig. 2.13 also confirm the existence of asymmetric vortices in the near-field of the IDF flow, indicating a state of unstableness; whereas no individual vortex presents in the near-field of the NDF, indicating a state of stableness.

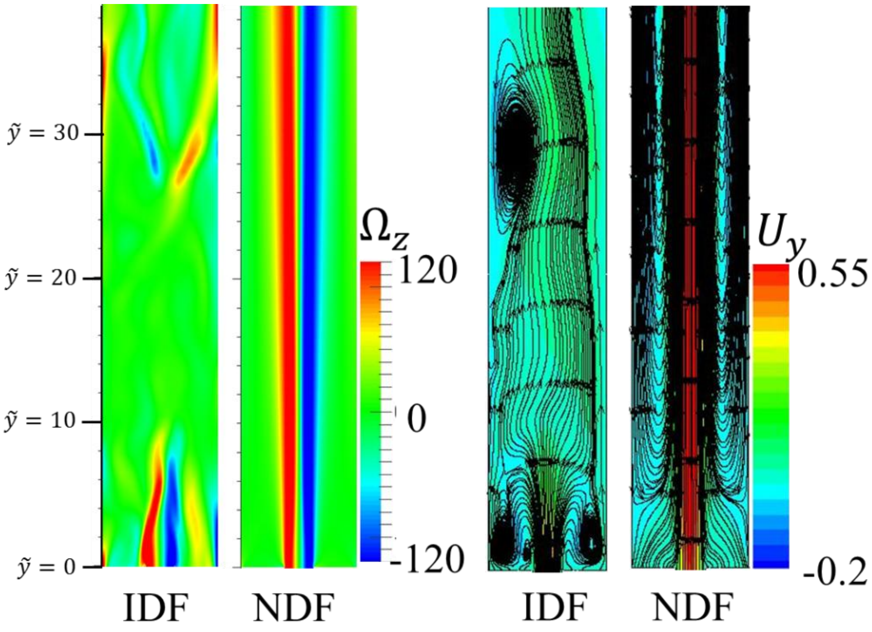

Fig.2.13: Comparison of the instantaneous vorticity (Ω_z) contour (left) and streamline (right) between a non-reacting IDF flow and a non-reacting NDF flow.

In Fig. 2.14 and 2.15, the initial flow evolution is shown. Note that to clearly show the flow evolution, the vorticity contour (colored with black and white) with the velocity vector gives an intuitionistic picture of the initial flow motions. In the beginning, the heavier incoming air flow injection meet with the lighter outer fuel flow, two large vortexes on both sides produced due to shear. Meanwhile a portion of air flow sinks down to the outer flow with the gravitational effect. The sinking air generates a reversed flow region leading to several smaller vortexes in the outer flow of the near field. These vortexes evolve and interact with the main inner air flow causing whole near flow filed turn to instable. Flow oscillation intensity was enhanced in the downstream due to strong interaction of the vortexes. After long enough time period, flow symmetry was broken and the inner air flow starts to oscillates from left to right.

Further information can be found in Fig. 2.15. At t=1.0s, the smaller vortexes in the outer flow of the near field region start to interacts with the large vortex from the main air flow. Those vortexes which have a same spinning direction with the large vortex will combined together to produce a larger vortex and separates from the main air flow, whereas vortexes with an opposite spinning direction vanishes. The above interaction process operates in cycles, with continuous incoming flow shear induced vorticity flow will turn to turbulence eventually. Note that the flow fields in these two figures are for initial stage, further information for the flow field at a statistic steady state will be discussed later.

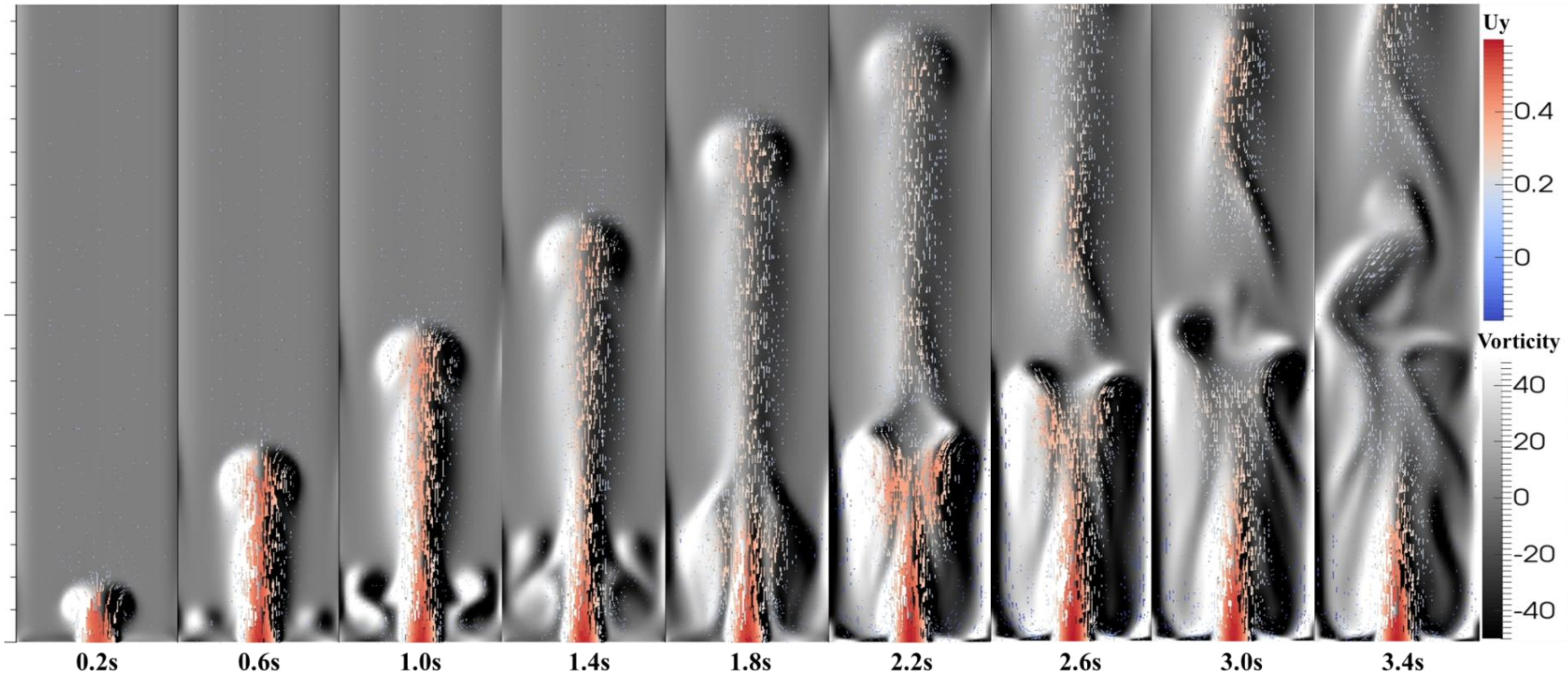

Fig.2.14: Flow evolution at the initial stage (V_{inner}=30cm/s, V_{outer}=2cm/s, Fluid component: pure air for inner flow and pure methane for outer flow)

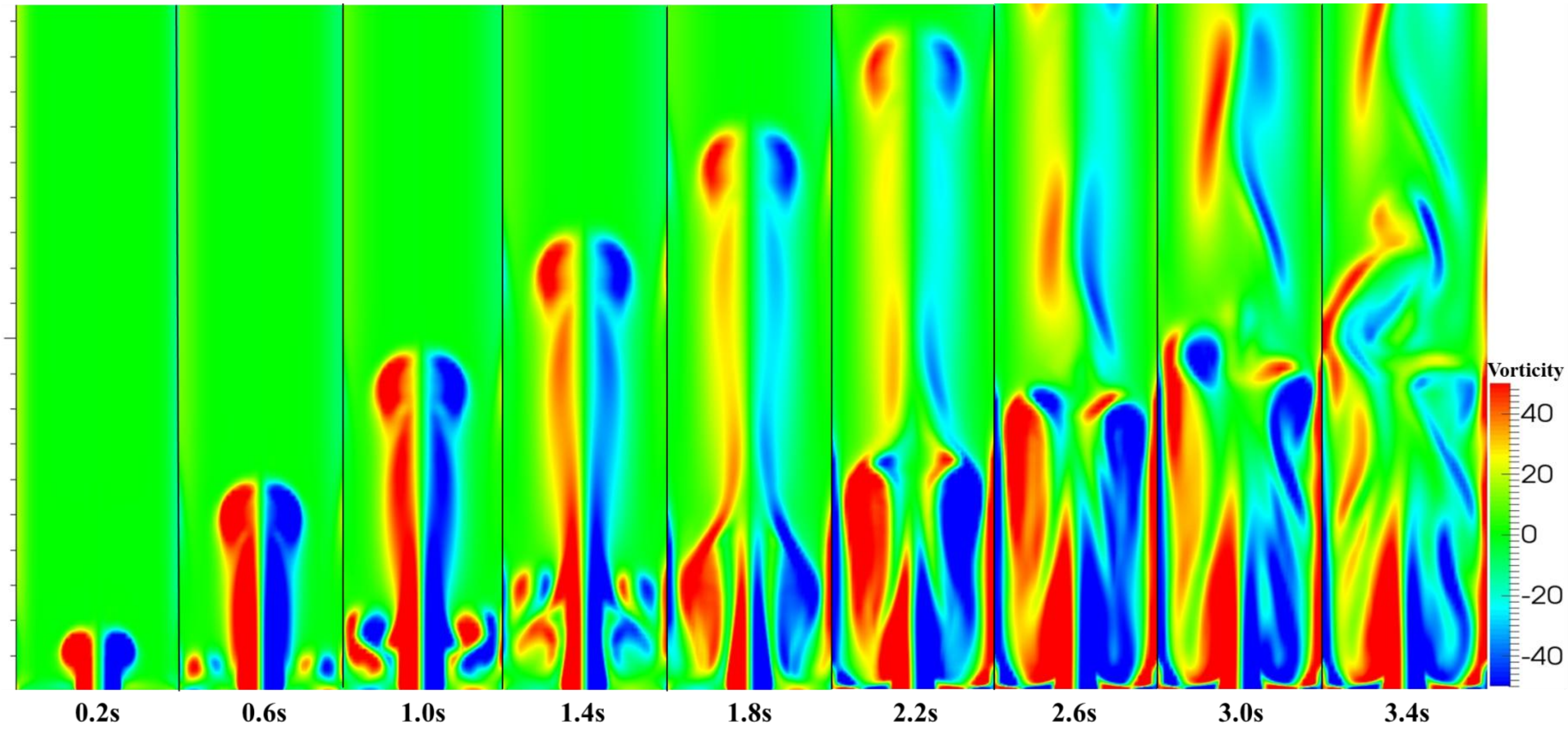

Fig.2.15: Instantaneous z-direction vorticity at the initial stage (V_{inner}=30cm/s, V_{outer}=2cm/s, Fluid component: pure air for inner flow and pure methane for outer flow)

2.4.2 Instability in Reacting Flows

To understand the flame instability in IDFs, we recognized that any flow instability is the result of unsteady behaviors of vorticity, which should not be fundamentally different between reacting and non-reacting flows. Thus, the two mechanisms responsible for the instability of the non-reacting IDF flow can be applied to the IDF to understand the effect of combustion on flow stability. Fig. 2.16 illustrates the comparison between a non-reacting flow (the benchmark case) and its corresponding IDF with the same inlet flow conditions. Here, we consider the region containing the flame to be the near-field of the IDF, where the fuel and oxidizer mixes and interacts with each other intensively. It is observed that the initial shear flow of the IDF is notably enhanced in the near-field, because the inner flow velocity is significantly increased as a result of thermal expansion caused by the combustion heat release. Moreover, the density gradient of the IDF is reversed so that the $\boldsymbol{\nabla}\rho \times \boldsymbol{g}$ term is opposite of that for the non-reacting flow. This is because the combustion heats up the inner flow and hence reduces its density to be lower than that of the outer flow. As a result, the buoyancy-induced vorticity $\boldsymbol{\nabla}\rho \times \boldsymbol{g}$ and the vorticity $(\frac{\partial U_y}{\partial x})\vec{k}$ of the initial shear flow have the same direction. This shear layer configuration resembles the non-reacting NDF flow discussed in Section 5, in the sense that the buoyancy effect in both cases would enhance the initial shear flow.

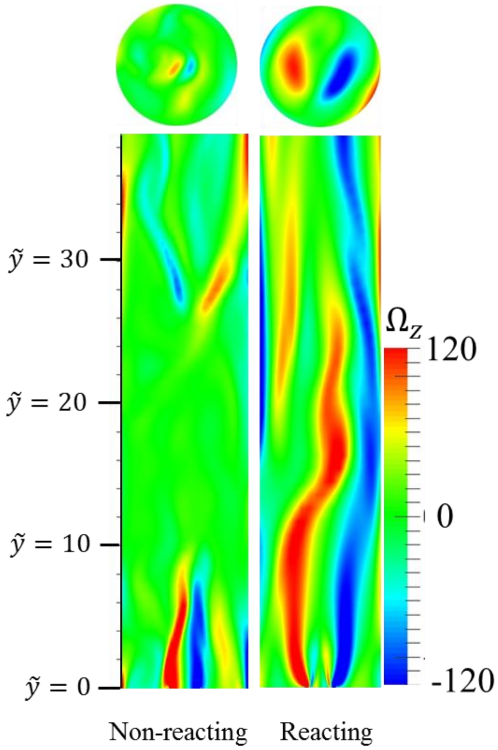

Fig.2.16: Comparison of the instantaneous vorticity (Ω_z) contour between the non-reacting (left) and reacting (right) IDF flows.

Based on the above analysis, we conjectured that the buoyancy effect stabilizes the initial shear flow in the near-field of an IDF. This conjecture is qualitatively supported by the comparison between the non-reacting and reacting flows in Fig. 2.16, where the shear layer of the reacting flow displays relatively symmetric structure in the near-field compared with the non-reacting flow. For a better illustration, Fig. 2.17 shows the time evolution of the vorticity contour for the non-reacting and reacting IDF flows. Again, stable vortical structures can be observed in the near-field of the IDF, but unstable vortical structures are evident in the near-field of the non-reacting IDF flow. For the non-reacting IDF flow, we can observe additional vorticities outside the initial shear flow but with opposite direction. These vortices are the direct evidence for the buoyancy-induced shear flow. As discussed above, the buoyancy-induced shear flow and the initial shear flow are comparable to each other but of opposite vorticity, flow instability develops immediately in the near-field.

For a quantitative validation of the above analysis, Fig. 2.18 presents the evolution of the time-averaged streamwise turbulent kinetic energy evolution along the axial direction. The point (0, $\tilde{y} = 3.8$, 0) is where the time-averaged flame tip is located and serves as the indicator for the near-field of the IDF. The result suggests that the unsteadiness in the near-field of the IDF is much lower than its non-reacting flow. Therefore, we conclude that the combustion-induced buoyancy effect suppresses the flow instability in the near-field of IDFs.

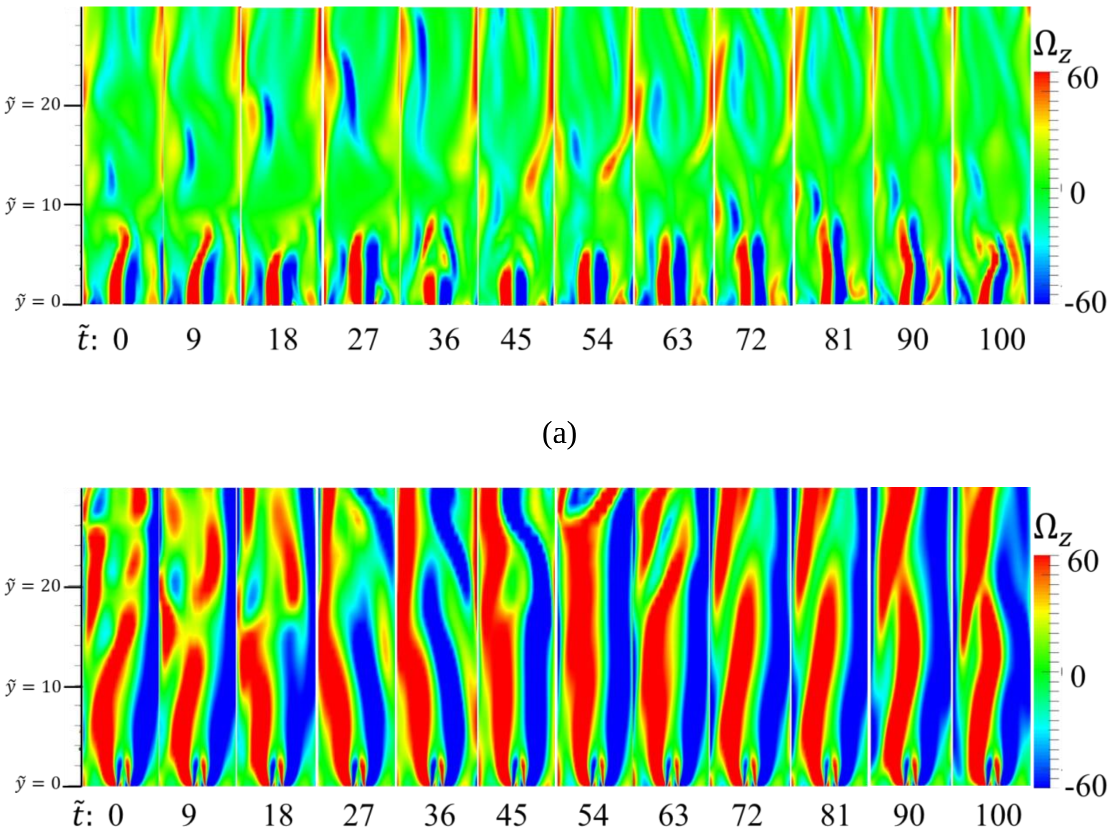

(a)

(b)

Fig.2.17: Time evolution of the vorticity (Ω_z) contour for (a) the non-reacting IDF flow and (b) the IDF. The non-dimensional time is defined as $\tilde{t} = tv_i/d_i$.

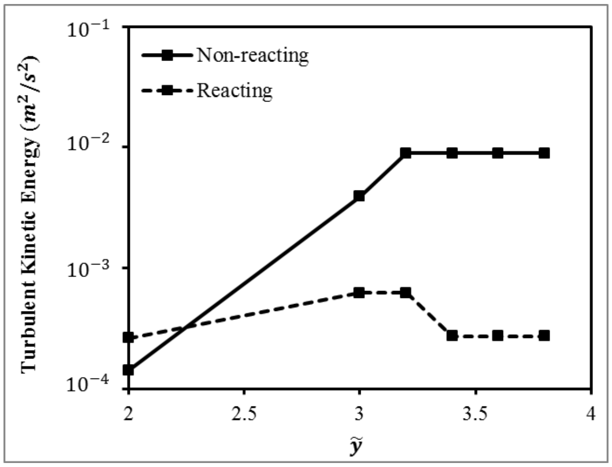

Fig.2.18: Time-averaged turbulent kinetic energy, $\frac{1}{2}{U_y}'^2$ for the non-reacting and reacting IDF flows at different axial locations.

It should be also noted that the above results imply that the far field of the IDF is more unstable than that of its non-reacting flow. This can be understood by that, since the initial shear flow is greatly enhanced in the near-field, natural instability (Kelvin-Helmholtz) starts to develop in the far field as the critical Reynolds number increases. The stronger shear flow of the IDF would induce stronger momentum transportation after the instability kicks in, which is reflected by the higher unsteadiness of the flow. Similar observation was also reported by Jiang and Luo [67], who stated that chemical heat release enhances the flow instability in buoyant flame. However, our study clarifies that the flow instability of a buoyant flame should be considered separately in the near-field and the far field, the latter of which will be the focus of a future work.

2.5 Summery of Part I

Buoyant methane/air inverse diffusion flames (IDFs) were experimentally and numerically investigated to understand their instability in the near-field. It is found that, in buoyant non-reacting IDF flows, the initial shear flow and the buoyancy effect induce opposite-direction vorticities and the interaction between them causes flow instability in the near-field. The flow instability, measured by the turbulent intensity, increases as *Ri* approaches unity, at which the buoyancy term equals the initial shear term. Furthermore, chemical reaction would result in an enhancement of the initial shear layer in the near-field and a reversed density gradient, thereby suppressing the near-field flow instability. Since the flow and flame oscillation in IDFs is dependent on the density gradient between the inner and outer flow in the burner, changing of the fuel type may suppress the flow oscillation in non-reacting flows but will not cause significant difference in reacting flow since the chemical reaction always reduce the density of inner flow to be smaller than the outer flow. As a result, the conclusion that chemical reaction suppress the near field in IDFs still validates.

3 Part II: Wall Effects on the Stability of Buoyant Inverse Diffusion Flames of Methane

3.1 Introduction

Buoyant diffusion flames are common in various industrial combustion devices and accidental fires. Many physical phenomena of fundamental significance are found in buoyancy-driven reactive plumes, for instance vortex transportation and interaction, flow and flame instability, and flow transition to turbulence. Examining the dynamics of buoyant diffusion flames also contributes to applications, such as optimizing combustion efficiency and reducing fire damage. Regardless of the numerous investigations conducted over the past decades [119-121], some processes in buoyant diffusion flames have not been completely understood [122].

Inverse diffusion flames (IDFs), which are typically operated in buoyancy-controlled condition due to its relatively small blow-out limit, have been applied as laboratory flames to investigate soot formation especially soot inception for decades [123-126]. Commonly, IDFs burn in a co-flow and co-annular configuration so that soot forms in the fuel side of the reaction zone, where soot experience inception and surface growth before its agglomeration with other soot particles to form aggregates [123, 126, 127], whereas buoyancy-induced vortices occur in the downstream. These flame features provide an ideal condition for experimental measurements that are designated to model soot formation, especially soot inception and early growth. Due to the special structure of IDFs, such measurements are always performed in the downstream of the flames [123, 127], while flow instability developed in the downstream may cause difficulty to accurate soot sampling. Moreover, IDFs have been recently adopted in synthesizing carbon nanotubes (CNTs) [128, 129], for which an unstable flow may deactivate the catalyst particles by the transportation of polycyclic aromatic hydrocarbons(PAH) or soot to the catalytic substrate, thus impeding the growth or degrading the purity of CNTs [130]. While flow exerts an important influence on soot formation of IDFs [12, 125], the flow dynamics aspects of IDFs have not been sufficiently studied [14, 131-133]. An important factor affecting the stability of an IDF is the confinement wall which is often required to isolate the fuel from the ambient air. The introduction of the wall gives raise to another problem, namely the impact of the boundary walls on the transportation and interaction of the vortical structures. The wall effect is known to play significant roles in non-buoyant flames [134-136], whereas very few work has been concentrated on its influence on buoyant diffusion flames [137], let alone buoyant IDFs. Thus, a further examination of the influence of boundary wall on the flow field of IDFs is necessary.

In the present work, IDFs will be investigated through qualitative experimental observations and then detailed vortex flow analysis based on numerical simulation. The main objective is to understand the fundamental vortex dynamics mechanisms associated with the wall effect and their effects on flow stability of IDFs. Inspired by the knowledge of the wall effect, a shear-layer-based injection technique will be proposed and substantiated for flow stabilization control of IDFs.

3.2 Experimental Specifications and Numerical Methodology

As shown in Fig.3.1 (b), a co-annular burner was designed to generate IDFs. Air flow was injected through the inner tube with a diameter, d_a= 0.01 m, while the gaseous fuel (i.e. methane) through the outer annular with the diameter of the outer tube, d_f= 0.04 m. Thereinafter, non-dimensional distance is applied by using the actual distance divided by the inner tube diameter d_a. A quartz glass tube with a length of l = 0.4 m was mounted above the burner base to isolate the ambient air. The air and fuel flows were supplied by Dewar tanks and controlled by valves to maintain the inflow conditions at 293K and 101kPa. A Cartesian coordinate system is plotted on the burner in Fig. 3.11 (b) for the convenience of discussion in the following paragraphs. Particle Image Velocimetry (PIV) experiments were performed to validate the present numerical simulations. For more detailed information of the air and fuel supply systems, PIV set-ups and the flame image capture system, the interested readers are referred to a recent work by the authors [138].

Large eddy simulation (LES) was also implemented to investigate the IDF flow through the open source code, OpenFOAM [139]. The unsteady Navier-Stokes equations were solved by Pressure and momentum correctors combined with the Pressure Implicit with the Splitting of Operators (PISO) method [140]. The spatial and unsteady terms were discretized by second order schemes [141, 142]. Second order central difference linear interpolation was applied for mass flux calculation. The time step was limited by Courant-Friedrichs-Lewy (CFL) number with the value of 0.4 for non-reacting cases and 0.3 for reacting cases to reduce the simulation oscillation. The computational mesh of the burner for a representative case is shown in Fig. 3.1 (a). The total grid nodes is 0.6

million with local refinement in the vicinities of the fuel-air interfaces as well as the solid wall. The grid size varies in the range of $0.01d_a$ – $0.12d_a$, which is smaller than the turbulence length scale (~$Re^{-1/2}$) for the current problem [143]. The infinitely fast and irreversible chemical reaction schemes were coupled with the flow solver to calculate the flow and temperature field. Non-slip wall and fixed temperature value were applied as the wall condition. The boundary conditions for a benchmark IDF are listed in Tab.2.1 of the supplemental material and the validations of non-reacting and reacting cases are shown in Part I. More detailed numerical methodology is provided in Ref. [138].

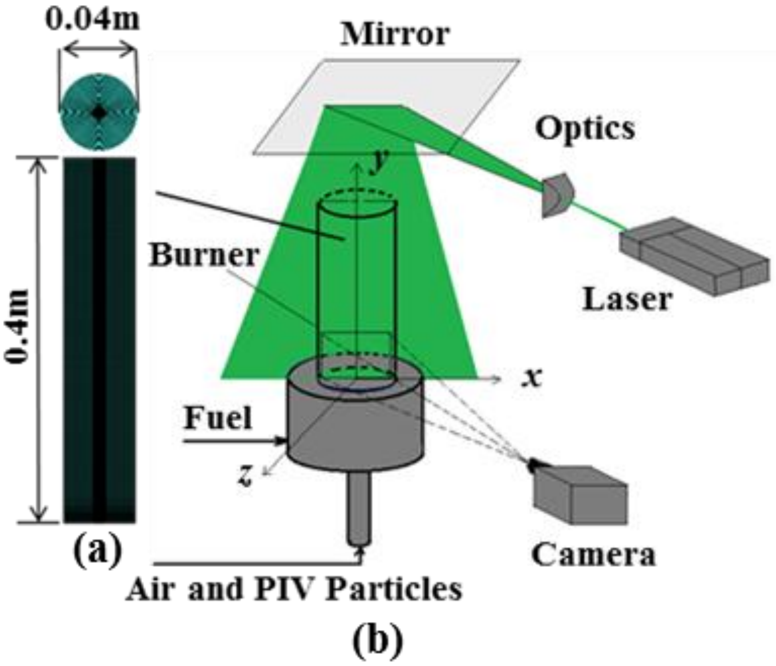

Fig.3.1: Computational mesh (a) and experimental specifications (b).

3.2 Regime Diagram of Methane IDFs

In the present work, we first investigated the stability regimes of IDFs as shown in Fig. 3.2. The burner has a fixed configuration, with an outer-to-inner diameter ratio

$k = d_f/d_a = 4$. Thus, the controlling parameters are the flow rates of the injecting air and fuel, which result in two non-dimensional flow parameters, such as the air flow Reynolds number, Re_a, and the fuel flow Reynolds number, Re_f, and an overall equivalence ratio, Φ, as a non-dimensional measure of the relative abundance of fuel compared with air:

$$Re_a = \frac{\rho_a v_a d_a}{\mu_a},\ Re_f = \frac{\rho_f v_f d_a}{\mu_f},\ \text{and } \Phi = 2(Q_f/Q_a), \tag{1}$$

where ρ, v, and μ are the density, velocity, and dynamic viscosity, respectively. Q is the molar flow rate. The subscript a and f represent the properties of the air and fuel flows, respectively.

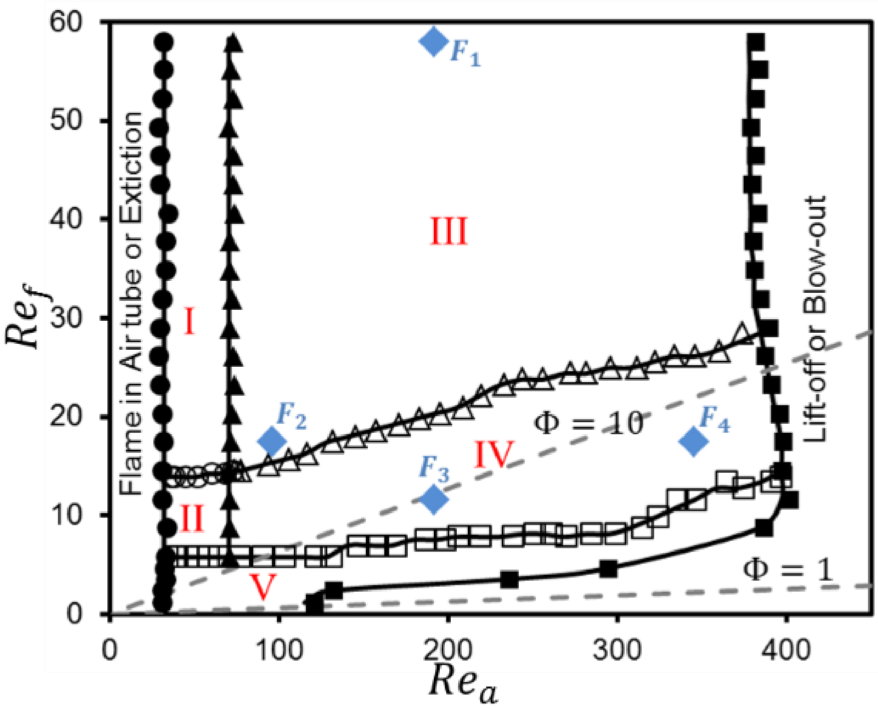

Fig.3.2: IDF regime diagram for the burner with k=4. k is the inner and outer diameter ratio, Φ is the overall equivalence ratio, and the air flow Reynolds number, Re_a, the fuel flow Reynolds number, Re_f.

Five different regimes of IDFs were identified in Fig. 3.2 based on their visual appearance, as are summarized below.

(1) *Regime I*: Stable; blue flame at the bottom and faint yellow cap right above the blue region; increasing Re_f causes no notable change in flame appearance.

(2) *Regime II*: Unstable; flame has a slight swaying and flicking; blue flame with a faint yellow cap, similar to Regime I.

(3) *Regime III*: Stable; brighter and more extended yellow flame region than Regime I; flame height increases with Re_a in a roughly linear pattern; increasing Re_f slightly decreases flame height and causes no significant change in flame appearance.

(4) *Regime IV*: Unstable; notable flame swaying and flickering identified; the swaying amplitude of the visual flame increases with increasing Re_a or decreasing Re_f.

(5) *Regime V*: Unstable; dim blue flame without yellow flame; notable swaying and flickering of the blue flame identified; with sufficiently large Re_a, over-ventilated flame occurs.

It is noted that Fig. 3.2 generally agrees well the regime diagram provided by Wu and Essenhigh [133]. The main difference between the two regime diagrams is the different flame characteristics at low Re_f, where the flame is sensitive to slight variation of fuel or air inflow. Regardless of the slight difference, the most representative stable (III) and unstable (IV) regimes are captured in both regime diagrams. Fig. 3.2 shows that the IDFs tend to become more stable with decreasing Re_a or increasing Re_f. Furthermore, Re_a shows a predominant effect on the flame height, the size of yellow flame, and the radiation intensity, which are less sensitive to Re_f. This is because with the present burner geometry and dimensions (especially the diameter ratio $k = 4$), flames of most regimes are globally “fuel rich” according to the isolines of Φ in Fig. 3.2, meaning that fuel is sufficient in regimes above the $\Phi = 1$ line while air is consumed completely. Thus, further increasing the fuel flow rate (or Re_f) would not significantly affect the flame properties that are dictated by the chemical reaction.

The current experimental setup was not designed for capturing the velocity field of a reacting flow, due to the lab ventilation restrictions for combustion products and solid seeding particles. Instead, we adopt validated numerical simulation to resolve the flow field of an IDF. Fig. 3.3 presents the comparisons between experimental flame images and simulated temperature fields for four representative cases. As shown in Fig. 3.2, the four benchmark cases are marked $F_1 - F_4$ and correspond to Regime III and Regime IV, which are the most representative stable and unstable IDF regimes, respectively. The inlet conditions for the four IDFs are: F_1 $(Re_a = 192, Re_f = 58)$; F_2 $(Re_a = 96, Re_f = 17.4)$;F_3 $(Re_a = 192, Re_f = 11.6)$;$F_4$ $(Re_a = 345.6, Re_f = 17.6)$. Hereinafter, the IDF has the same Re_a and Re_f with F_1 will be marked as F_1, and so forth. According to the study of methane/air IDFs by Mikofski et al. [126], the edge of the blue flame approximates the reaction zone, characterized by a local temperature peak. Comparing the blue flame edge in the experimental images with the peak temperature shape of the simulation results, the qualitative features of the experimental and numerical IDFs in Fig. 3.3 agree well with each other, showing a general good performance of our simulation in predicting both the flame appearance and the flame stability mode.

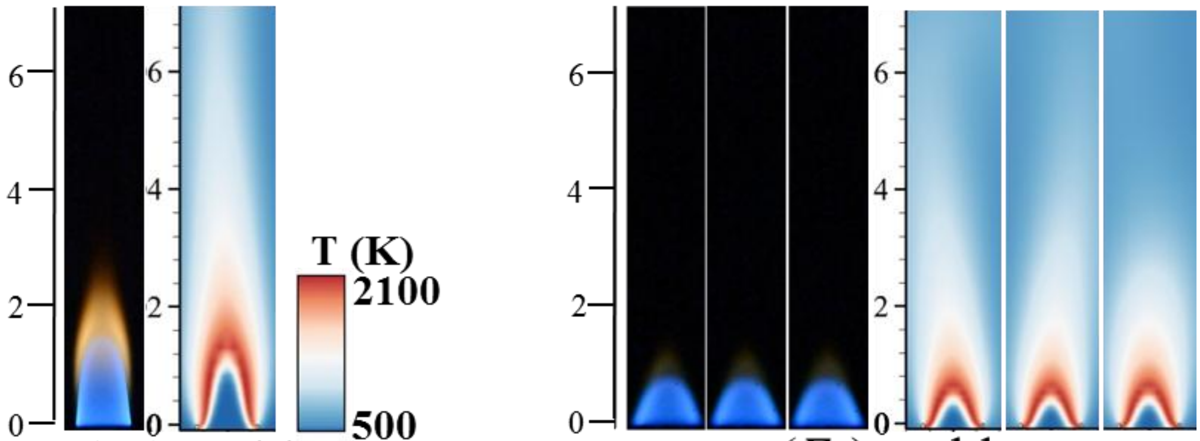

(F_1)-stable

(F_2)-stable

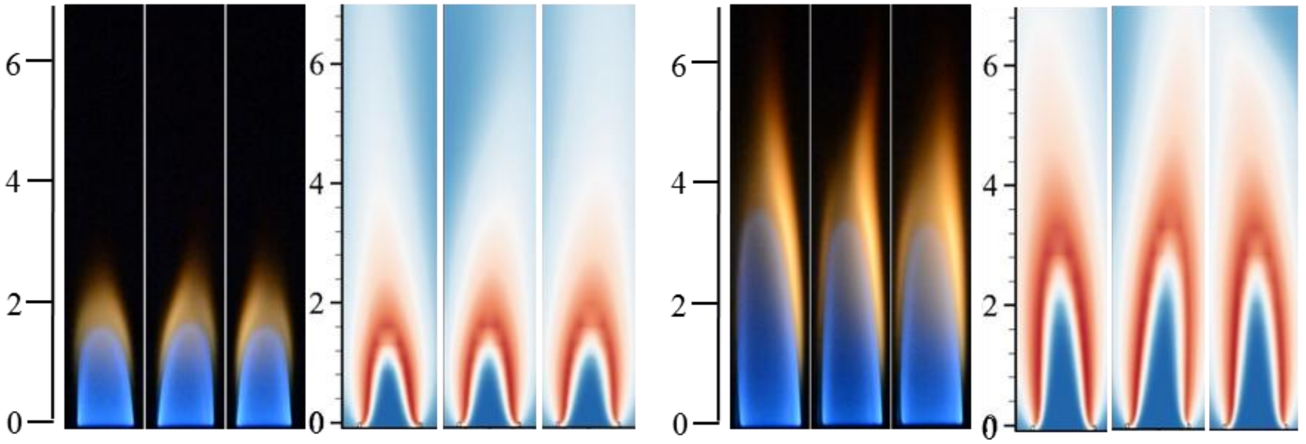

(F_3)-unstable

(F_4)-unstable

Fig.3.3: Instantaneous experimental and numerical flame images for the four IDFs $(F_1 - F_4)$.

Although the stability of IDFs is described based on the visual flames, we need to consider the entire flow field to understand the fundamental mechanism. This is because, as the flow moves downstream of the flame, the transition to an unstable flow is often inevitable, even for the case with a stable visual flame, e.g., the unstable flow structure downstream of the flame evident from the simulated temperature field of F_2. Since the development of instability often originates from the far field and then gradually propagates to the near field, we deem the flow instability occurring downstream to be of essential importance. Thus, the flow stability of the IDFs will be further investigated in the next section in a global sense, which contributes to a comprehensive understanding of different effects on flow and flame stability of IDFs.

3.3 Results and Discussion

3.3.1 Wall Effect of an IDF from Vortex Dynamics Perspective

In general, a diffusion flame sheet corresponds to a thin layer where fuel and oxidizer encounter and react with each other. As the reactants are transported to the flame sheet through convection and diffusion, any dynamic behavior of the luminous flame reflects the unsteadiness of its associating flow field, which usually involves vortices. For buoyancy-driven diffusion flames, the flame oscillation has been attributed to the formation and convection of the large vortical structures [119, 144, 145], where the vorticity is generated by a combined effect of gravity and density gradient [122, 146]. The same buoyancy-induced mechanism should also account for the vorticity generation of the current IDFs. One major difference, however, originates from the addition of the solid-wall confinement, which is practically necessary to isolate the fuel flow of an IDF from its ambient air environment. To this end, the current work seeks to understand the effect of the confinement wall from the vortex dynamics perspective.

We start by analyzing the flow stability of the IDFs in Fig.3.3. The contours of the z-direction vorticity, Ω_z, in the xy plane are plotted for cases F_1-F_4 in Fig. 3.4(a). In each case, two initial shear layers with opposite-direction vorticity grow along the flame as they convect downstream, thanks to the buoyancy-induced vorticity generation. It can be observed that, in all cases, the region of stable luminous flame of Fig. 3.3 approximately matches with the region of symmetric shear layers of Fig. 3.4(a), verifying the relevance between vortices and flame stability. However, the centre shear layers seem to become unstable further downstream, even for case F_1 that has an apparent stable luminous flame. Judging from the downstream shear layers, which are in close contact with the side walls, we hypothesize that this flow instability is caused by the wall effect. A direct evidence is the emergence of a wall-bounded induced shear layer (WISL), as illustrated in Fig. 3.4(a), that is generated due to the induced effect of an existing vortex or shear layer approaching the wall. The mechanism generating the WISL has been well understood by previous studies of vortex-wall interactions [147-149]. Basically, a primary shear layer would always induce a crossflow along its adjacent solid boundary in the inviscid sense. Due to the non-slip boundary condition, the inviscid crossflow of the primary shear layer has to be decelerated at the wall, thus resulting in the formation of a boundary layer on the wall surface, which is the WISL. It is interesting to note that the vorticity inside the WISL is intrinsically opposite to the primary shear layer. Next, we shall discuss the detailed interactions between the WISLs and the primary shear layers to understand the subsequent effects on the stability of IDFs.

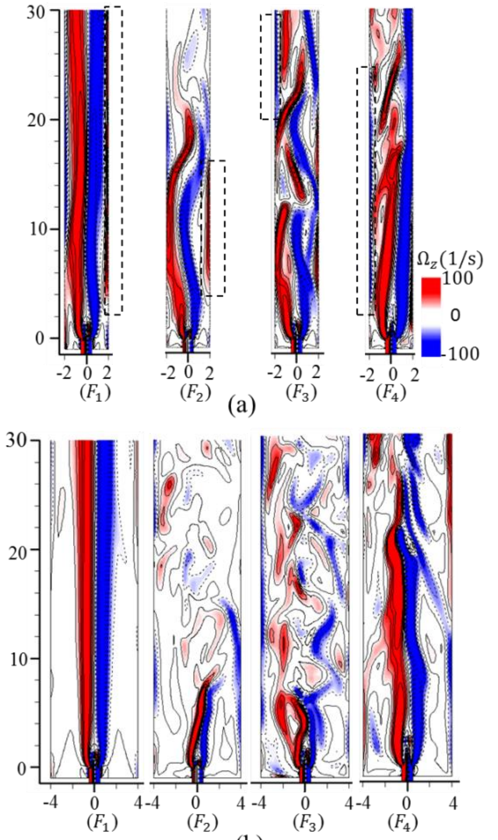

(a)

(b)

Fig.3.4: Instantaneous *z*-direction voticity Ω_z contours for F_1-F_4 (a): $k = 4$; (b): $k = 8$. The wall-bounded induce shear layers (WISLs) are marked by the dashed boxes.

3.3.2 Wall Effect on Flow Stability of IDFs

From vortex dynamics perspective, the effect of a vortical structure on its ambient flow is generally two folds, namely convective and diffusive. The convective effect can be thought as a superimposed velocity field on the original flow without the vortex; whereas the diffusive effect can be considered as an added source or sink of vorticity. Thus, the convective effective is likely to cause the change of motion while the diffusive effect causes vorticity addition or annihilation. For the WISL considered in the current study, its fundamental principle should not be different from that of a general vortical structure.

In order to examine in detail the convective and diffusive effects of the WISL, we need to compare the current IDFs to reference cases that have no wall effects or at least reduced wall effects. For this purpose, four additional cases were simulated for an enlarged burner with k = 8, while their other conditions being identical to cases F_1-F_4, respectively. It is noted that the enlarged burner corresponds to an increased effective Φ, which however generates no obvious influence on the chemical properties of the IDFs since they are already "fuel rich" according to Section 3. The results of vorticity contours for the k = 8 cases are presented Fig. 3.4(b). To provide a quantitative judgement of the stability for the IDFs in Fig. 3.4, the variations of turbulence intensity along the center line are plotted in Fig. 3.5. Here, the turbulence intensity is defined as $I = \frac{u'}{U}$, where u' is the root mean square of the turbulent velocity fluctuations and U is the Reynolds averaged mean velocity.

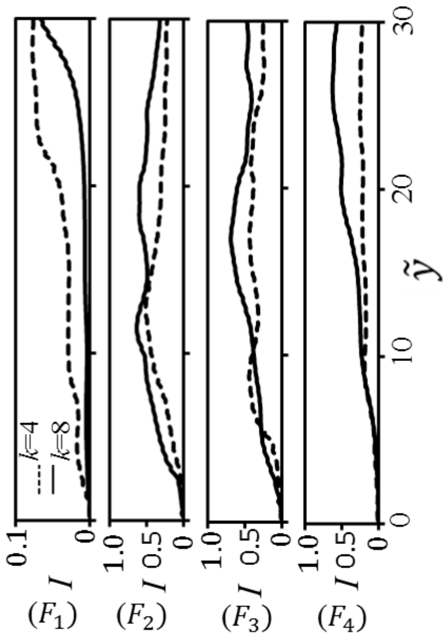

Fig.3.5: Comparison of turbulence intensity variation along the center line for F_1-F_4 with dash line: *k*=4; solid line: *k*=8.

We first compare the two cases, k = 4 and k = 8, of F_1. It is observed that the flow corresponding to k = 8 is rather stable throughout the entire flow field and no notable structure can be identified near the wall. The k = 4 case, on the other hand, has slightly sinuous centre shear layers, displaying a less stable flow compared with the k = 8 case. This observation is also supported by the turbulent intensity calculations of F_1 in Fig. 3.5. Since the apparent difference between the two vorticity contours is the asymmetric WISLs generated near the side wall of the smaller burner, the effect of the WISL in this case should be understood as convective, which cause small disturbances to the main shear layers.

For the cases corresponding to F_2-F_4 in Fig. 3.4(b), the flow become much more unstable than F_1 because of either an enhanced initial shear layer (F_2, F_3) or an increased buoyancy-induced vorticity generation due to elongated flame (F_4). By comparing Fig. 3.4(a) and Fig. 3.4(b), the stronger WISLs of cases F_2-F_4 in Fig. 3.4(a), induced by main shear layers that are closer to the walls, seem to cause a less intense breakdown of vortices or a weaker turbulence as indicated from Fig. 3.5. This suggests that stronger WISLs tend to stabilize the main shear layers for cases F_2-F_4, which could be explained by the diffusive effect of the WISLs as follows. Recall that a WISL and its associating main shear layer have opposite-sign vorticities, according to the vorticity diffusion term, $\nu\nabla^2\omega$, in the vorticity transport equation[137], the vorticity diffusion serve as vorticity sink to deplete vorticity in both shear layers, and the effect intensifies as the shear layers become closer to each other. In the cases of the larger burner where the main shear layers are initially farther away from the side wall, the wall effects are relatively weak so the main shear layers are able to grow and roll up into large vortices, which then detaches from the main shear layers and interacts with the wall to create a highly unstable downstream flow; this is evident from the segmental vortical structures in Fig. 3.4(b). However, in the cases of the smaller burner, the closer distance between the main shear layers and the wall causes strong WISLs, the diffusion effect of which prevents the growth and roll-up of the main shear layers during the early-stage development. As a result, the main shear layers of F_2-F_4 in Fig. 3.4(a) remain rather intact or at least less disturbed compared with those in Fig. 3.4(b).

The above findings can be further interpreted below. For an initially stable IDF, the introduction of side wall would cause WISLs that affect the main flow through convection and impair the established flow stability. For an initially unstable IDF, stronger WISLs would help restrain the continuous growth of the main shear layer and suppress vortex roll-up and detachment, which eventually contributes to a more stable downstream flow.

3.3.3 Wall-inspired Inflow Control for Stabilization of an IDF

Stable IDF is necessary for the convenience of soot measurement; more importantly, stable buoyant diffusion flames are generally desired in practical applications. Inspired by the stabilization effect of the wall, this work seeks to further explore stability control technique that mimics the diffusion effect of the WISL. Realizing that the WISL is essentially a shear layer that is counter-rotating to the main shear layer, we thereby introduce such an initial shear layer in the fuel flow in the *xy* plane as shown in Fig. 3.6. The air flow is injected from the center tube, the inner fuel flow Fuel-1 through the inner annular with $|\tilde{x}| = [0.5, 2]$, where $\tilde{x} = \frac{x}{d_a}$, and the outer fuel flow Fuel-2 through the outer annular with $|\tilde{x}| = [2, 4]$. Here, case F_2 with *k* = 8 is chosen as the benchmark case, with the vorticity contour shown in Fig. 3.7 (a) for comparison. By fixing the velocity of Fuel-1, v_{f-1}, and adjusting the velocity of Fuel-2, v_{f-2}, so that $v_{f-2} > v_{f-1}$, a special shear flow (Shear Flow-1) with the opposite direction to its corresponding main shear flows is generated in the vicinity of $|\tilde{x}| = 2$. To describe the strength of Shear Flow-1, a Reynolds number is introduced by $Re_s = \frac{\rho_f v_s d_f}{\mu_f}$ where $v_s = v_{f-2} - v_{f-1}$. In this study, two additional cases with $Re_s = 46.4$ and $Re_s = 162.4$ were simulated with the instantaneous *z*-direction vorticity Ω_z contours shown in Fig. 3.7 (b) and (c) respectively. It is note that Ω_z for the initial inflow is approximated by $\Omega_z = \left(\frac{\partial U_y}{\partial x} - \frac{\partial U_x}{\partial y}\right)\vec{k} \approx (\frac{\partial U_y}{\partial x})\vec{k}$, where U_x, U_y are the x-direction and y-direction velocity in the *xy* plane respectively, with $\vec{k}$ being the unit vector along *z*- direction.

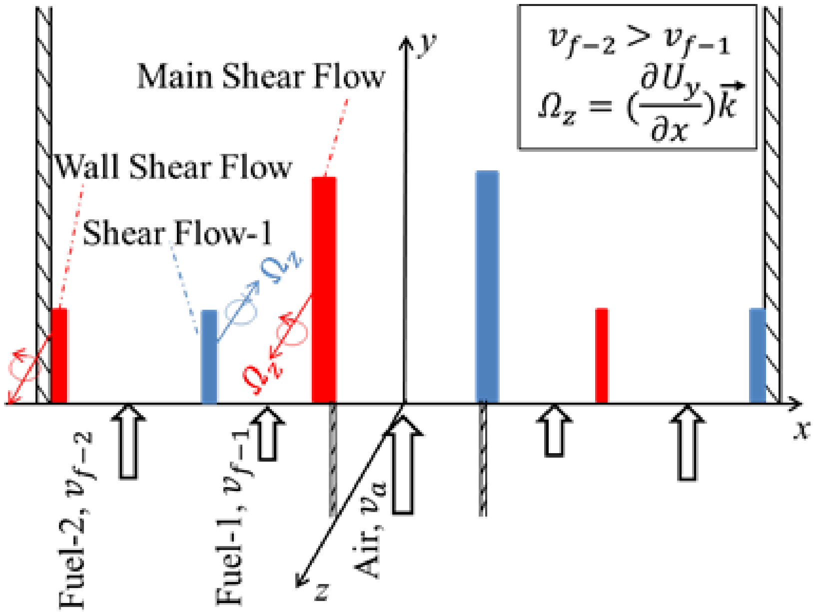

Fig.3.6: The schematic of the non-uniform inflow injection in the *xy* plane. red bar: shear flows with positive Ω_z; blue bar: shear flows with negative Ω_z

As illustrated in Fig. 3.6, the wall shear flow is much farther away from the main shear layer than Shear Flow-1 and thus is less influential according to the discussion in Section 4.2. This means that the flow stability should be dominated by the interaction between the main shear flow and Shear Flow-1. Since Shear Flow-1 is in opposite direction to the main shear flow, its effect should be similar to the WISL which serves as a vorticity sink to suppress the instability developed on the main shear flow. In Fig. 3.7, comparing (a) and (b) does not show a notable change in flow stability, probably because the Shear Flow-1 is still weak and convection still dominates over diffusion. However, further increasing Re_s to 162.4 in Fig. 3.7(c), the instability almost disappears completely. These qualitative observations are well supported by the corresponding turbulent intensity plots in Fig. 3.7(d). Furthermore, comparing the curves between $Re_s = 0$ and $Re_s = 46.4$, we find that increasing Re_s does help push the turbulent transition to farther downstream region. Therefore, these results demonstrate the effectiveness of the wall-inspired shear layer of the inflow in stabilizing the current IDF, which in turn verifies our understanding of the WISL. Last, it is emphasized that this understanding is not limited to an IDF since it is based on the fundamental mechanisms of vortex dynamics. Future relevant work will focus on extending this knowledge to study and control the stability of general diffusion flames with or without confinement.

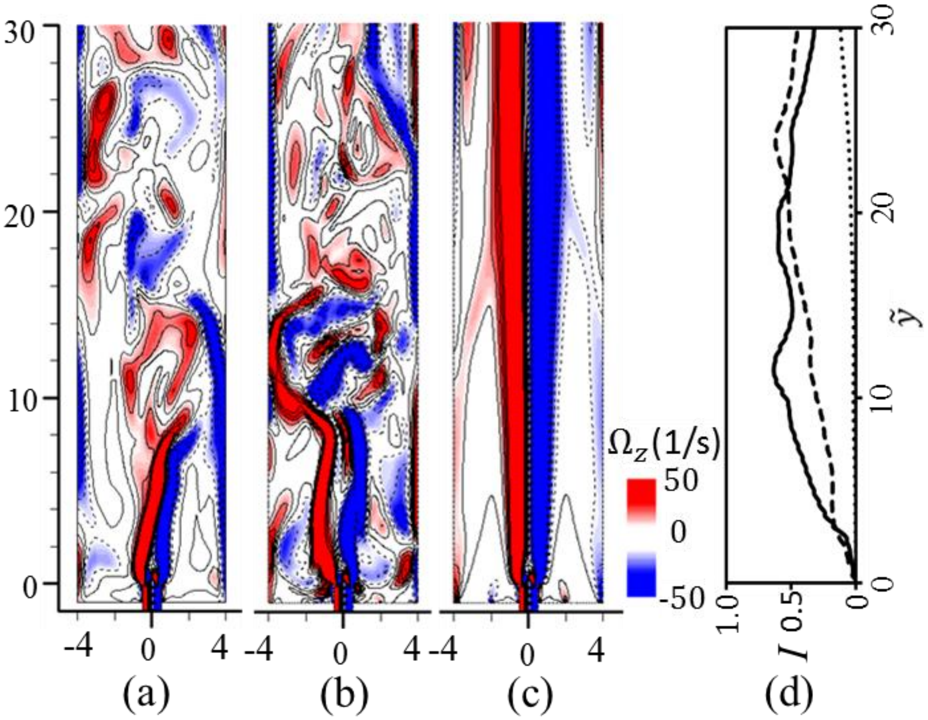

Fig.3.7: Instantaneous z-direction vorticity Ω_z contours for F_2 with k=8 under the condition of (a): uniform fuel inflow ($Re_s = 0$); (b): $Re_s = 46.4$; (c): $Re_s = 162.4$. (d): turbulence intensity variation along the center line for $Re_s = 0$ (solid line), $Re_s = 46.4$ (dashed line), and $Re_s = 162.4$ (dotted line).

3.4 Summery of Part II.

In the present work, methane IDFs were experimentally and numerically investigated. The visual characteristics in the near field of the IDFs were described with the focus on the difference between stable and unstable IDFs. Through numerical simulation, the flow field of IDFs has been physically delineated and the wall effects through the wall-bound induced shear layers (WISLs) have been identified. The IDFs generated from an enlarged burner were numerically found to have minor wall effects. By analyzing the vorticity transportation, we found that the WISLs of the small-burner IDFs may cause either vorticity convection or vorticity diffusion. Specifically, if the original minor-wall-effect IDF is stable then the WISLs would destabilize the flow because of the disturbances introduced by vorticity convection. However, for originally unstable minor-wall-effect IDFs, the vorticity diffusion from the WISLs would stabilize the flow by restraining the development of the main shear layers, and consequently suppressing the roll-up and detachment of individual vortices.

Inspired by the mechanism of the WISLs on the stability of IDFs, a similar shear layer was created in the fuel inflow for stabilization control of an IDF. Since this additional shear layer has opposite sign of vorticity to the main shear layer, it plays the same role as the WISL to drain vorticity from the main shear layer and therefore stabilize the IDF. As the result, either the turbulence transition is pushed to the downstream or flow instability is totally suppressed, depending on the shear Reynolds number, Re_s. The study of this flow control technique on general diffusion flames may merit future studies.

4 Part III: The Influence of Centerbody Air Injection on Liquid Combustion in a Model Gas Turbine Combustor

4.1 Introduction

As a combustion technology widely used in gas turbine combustors for power generation and transportation, spray combustion in a swirling flow has been extensively studied in the past decades [150-152]. Flame stabilization in a swirl combustor is achieved by forming a relatively low-pressure region in the downstream of the swirler as the result of the swirling flow entrainment. Such a region is often referred as the central recirculation zone (CRZ). Because the size, shape and flow characteristics of the CRZ are of critical importance to the operation of swirl combustors, many studies have been focused on studying the fluid dynamic and combustion characteristics of CRZ [153-155] In CRZ, a backflow induced by an adverse pressure gradient [156] entrains a portion of the high-temperature post-combustion gases to the zone to sustain stable combustion. The adverse pressure gradient was frequently used to describe the CRZ characteristics.

Liquid fuel/air mixing in CRZ has a strong influence on the combustion efficiency and flame stabilization in swirl combustors [157, 158]. Hardalups et al. found that swirling flows have a potential of enhancing liquid droplets/air mixing, increasing complete droplets combustion and promoting the decomposition of the liquid sheet [159].According to Chen and Driscoll's study, the CRZ plays a role of enhancing fuel/air mixing. Specially, the CRZ acts like a large toroidal vortex with a characteristic velocity and length scale and the air is entrained into the vortex from the downstream region of the vortex. [160] Moreover, the important role of the swirl intensity and swirler geometry in enhancing air/feel mixing has been recognized. [161, 162] These findings suggest that additional benefits may be gained from manipulating the local stoichiometry by various means in non-premixed combustion of liquid fuels.[163, 164]

It has been well recognized that combustion efficiency, flame stabilization and volumetric heat release rates can be manipulated significantly through varying the swirling flow intensity. [151, 152] However, an excessive swirl may cause the central recirculation flow to move into the inlet annulus and lead to the occurrence of flame flashback in premixed combustion.[165-167] To solve the flashback problem in premixed combustors, Terhaar et al. [168] introduced an axial air injection through the center body and found that the axial air injection provided a suitable flow field for flame stabilization and flashback-proof. For non-premixed combustors, which although are completely free from flashback, the overheating problem of the fuel nozzle and combustion chamber wall is arisen. [57, 169] Fang et al. [58] developed a cold-wall bidirectional vortex non-premixed combustion chamber, in which the swirling flow is separated into two distinct coaxial zones, with the outer vortex stream circulating towards the head end and an inner concentric vortex in the opposite direction. The outer vortex protects the chamber walls from excessive heating loads via convective cooling. By using the means of centerbody air injection, the authors [170] have observed that the CRZ can be pushed to the farther downstream of the fuel nozzle and consequently lessen the overheating problem.

Efforts have been made by designing various swirlers to achieve desired combustion and emission characteristics. Notable examples are the multiple-stage swirler combustors[171, 172] and low swirl combustion (LSC) technology developed by

Researchers[173-175]. The main idea of LSC is to reduce the swirl intensity well below the vortex breakdown threshold by introducing axial flows through the central channel without being swirled so that no recirculating flow is generated in the combustor. Recently, Li et al. [170] studied a model gas turbine combustor with a very small amount of centerbody air injection and found that it holds potentials in enhancing combustion efficiency. In our preliminary testing experiments, the air was injected directly into the CRZ from the cross-drilled circular openings in the centerbody of the swirler. Higher temperatures were observed in the CRZ compared with the experimental results without the centerbody air injection. . A similar design was also used by Qian et al. [65] in bluff-body flame holders by cutting a slot in the center of a bluff-body.

In the present study, we substantially extended our preliminary study by conducting more detailed experimental studies and RANS calculation on kerosene-fueled combustors with and without centerbody air injection, with particular interests in characterizing the flow and temperature characteristics of the CRZ with centerbody air injection. For the simplicity of presentation we shall name the swirl combustor with air injection through the cross drills in the centerbody as cross-drilled swirl combustor (CSC for short and hereinafter), as it illustrates the geometry of the swirler. Similarly, non-cross-drilled combustor (NSC for short and hereinafter) shall be used to indicate the swirl combustor without cross drills and hence the centerbody air injection. By using the RANS calculation, which has been validated by the present experimental data, the influence of airflow velocity and excess air factor, was parametrically studied to demonstrate the effectiveness of the CSC. The structure of the paper is organized as follows. Experimental facilities are described in Section 2, followed by the specifications of

RANS calculation in Section 3. Results for CSC and NSC under non-reacting and reacting conditions are shown and discussed in Section 4.

4.2 Experimental Set-up

The schematic of the experimental system for the present study is shown in Fig. 4. 1.The heated air is accelerated by a centrifugal blower (7), which is driven by an electric motor (6), which can be precisely controlled to generate air flow, to enter an air-feed pipe (9, 10) and subsequently flow rotationally through the swirler fixed on the combustor chamber (16). The liquid kerosene stored in a fuel tank is driven by a nitrogen gas (1) of 2.0MPa to flow through the fuel-feed pipe (5) and then is injected into the combustion chamber (16) in the form of fuel droplets with a 60° hollow-cone. A combined Pitot tube and inclined-tube manometer (Product Model Number: YYT-200B) (19) were used to measure the velocity. Temperature was measured by calibrated thermocouples (Platinum/rhodium alloy thermocouple, Type B). Temperature data were recorded by the data acquisition system (13) (USB-7410, ChaoYu M&C. Co., Ltd, Wuhan, China). In addition, the composition of combustion products were collected and analyzed by a fuel gas analyzer (14) (ET5100 Shanghai Euro Tech Environmental Engineering Ltd.) at the exit of the combustor for estimating the combustion efficiency.

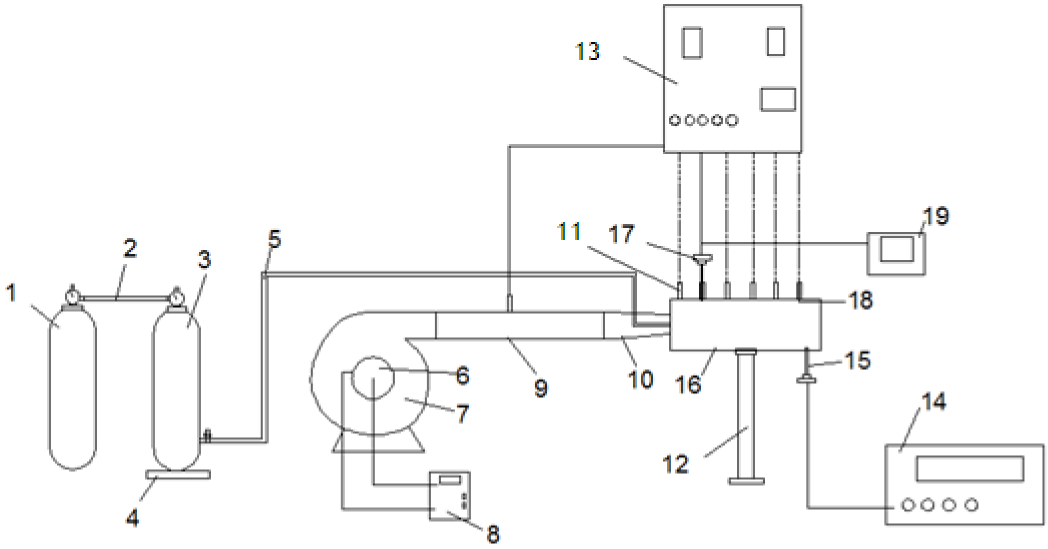

Fig.4.1: Schematic of the experimental facility used in the present study; 1. Nitrogen gas cylinder; 2. Gas pipeline; 3. Fuel tank; 4. Electronic scale; 5. Fuel-feed pipe; 6. Electric motor; 7. Centrifugal blower; 8. Motor controller; 9 and 10. Air-feed pipe; 11. Probe holes; 12. Metal holder; 13. Data acquisition system ; 14. Flue gas analyzer; 15. Flue-gas probe; 16. Combustion chamber; 17. Pressure probe; 18. Thermocouple probe; 19. Inclined-tube manometer.

Fig. 4.2 shows the schematic of the swirl combustor used in the present study. A cylindrical coordinate system (r, θ, z) is so established that the origin point is located at the exit of swirler and the fuel nozzle is located in the 5 mm downstream. The axial direction of the chamber is defined as the z-axis and the radial direction is defined as the r-axis. There are 7 probe holes in serial along the z-axis with a 50 mm separation on the combustor wall for the measurement of velocity and temperature. Velocity and temperature were measured at 30 different radial points at each axial location, as seen in

Fig. 2 (a). Cooling water was injected from the inlet to pass through the interlayer of the combustor chamber.

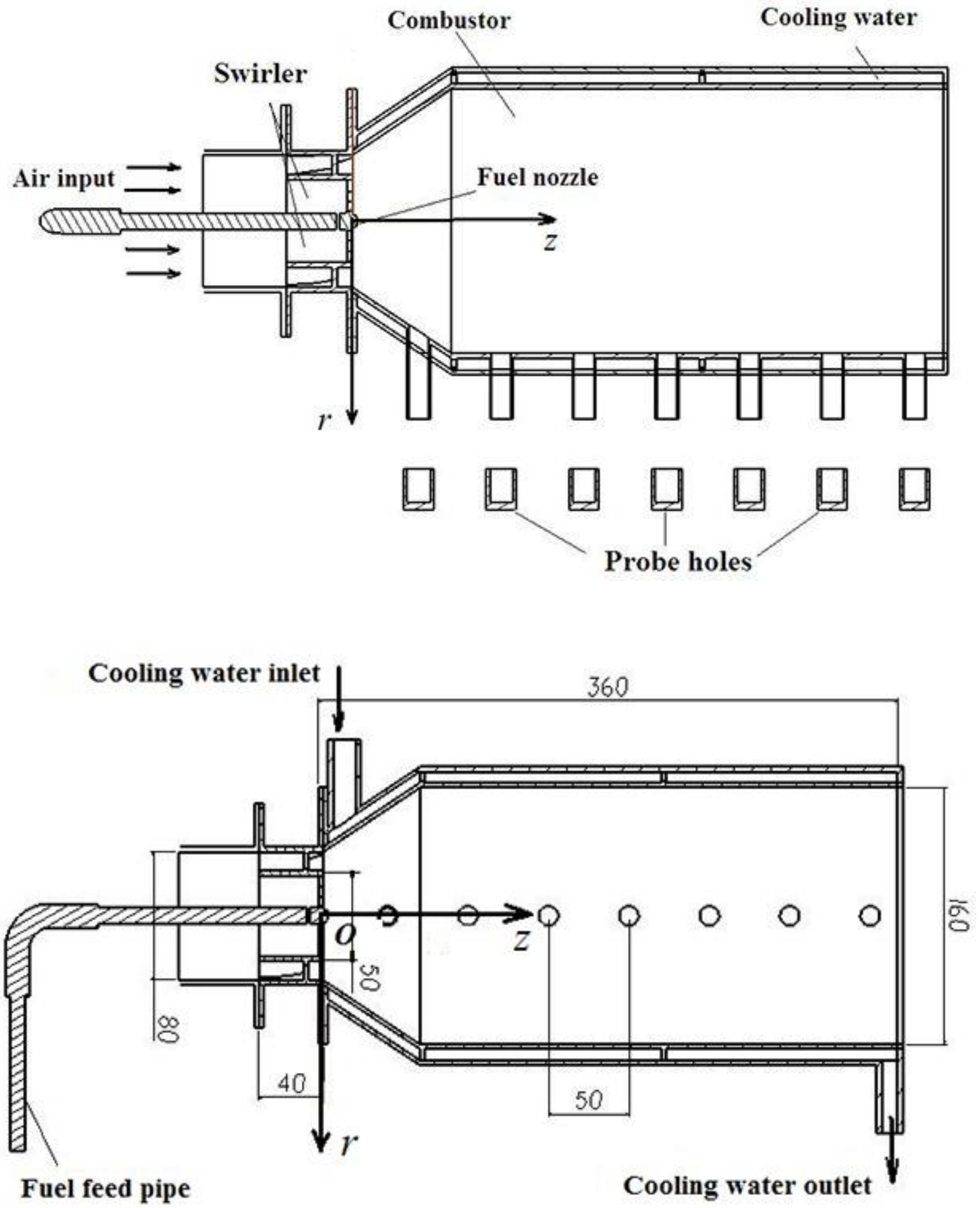

Fig.4.2: Schematic of the combustor geometry in top and side views. (Unit: millimeter)

To minimize the disturbance of the intrusive Pitot tubes or thermal couples to the flow the velocity or temperature measurement was conducted at only one location each time. A typical test in present work lasted for about 1-2 hours, which is sufficiently long to attain a steady-state flow and to finish the velocity and temperature measurements at all the radial and axial locations. The measurement data from the data acquisition system was recorded when a steady reading was obtained, normally 30 seconds after we mounted the measurement device into the combustor. The cross-drilled and non-cross-drilled swirler used in the present study are shown in Fig. 4.3. There are 12 curving vanes on each swirler and the curving angle is 45^o. For cross-drilled swirler, six cross-drilled holes of the 8 mm diameter are distributed uniformly around the center body, through which the airflow can be injected into combustion chamber from upstream of the swirler. In the CSC, a large portion of the incoming airflow is forced to rotate by the swirl vanes while also undergoing a gradual expansion. A small portion of the incoming airflow goes into the CRZ directly through the cross-drilled holes. The pressurized liquid fuel is injected into the combustor via a 60 °hollow-cone.

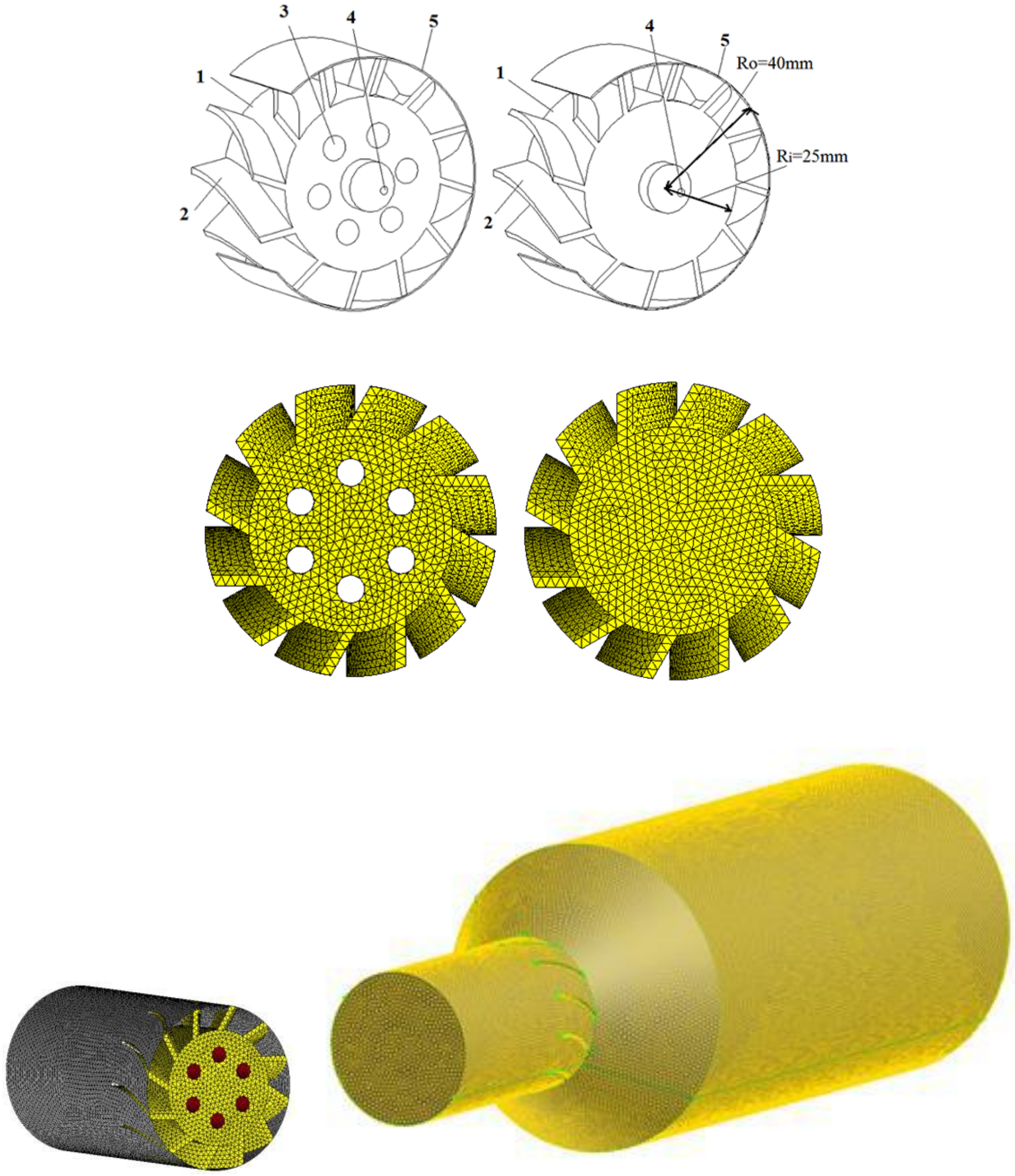

Fig.4.3: Geometry and unstructured mesh for the cross-drilled swirler. (a1) (a2) the non-cross-drilled swirler; (b1) (b2) 1. center body of the swirler; 2. swirler vane; 3. slot; 4. fuel nozzle; 5. circumferential band; (c1) 3D mesh of the computational domain of the CSC; (c2) inlet part of the computational domain of CSC.

Following Johnson et al's definition [176],, we define the local, effective swirl number, S, as the ratio of the tangential momentum flux to the axial momentum flux. Consequently, for NSC without centerbody air injection, the definition leads to

$$S_{NSC} = \frac{2}{3}\tan\theta\frac{1-R^3}{1-R^2} \tag{4.1}$$

and for CSC with centerbody air injection,

$$S_{CSC} = \frac{2}{3}\tan\theta\frac{1-R^3}{1-R^2+m^2((\frac{1}{R^2})-1)^2R^2} \tag{4.2}$$

where θ is the curving angle, R_o and R_i are the outer and inner radius of the swirler respectively, and $R = R_i/R_o$, as shown in Fig. 4.3. m is the rate ratio of the mass flow through the cross-drilled circular openings to the mass flow swirled by the vanes. In present work, $R = R_i/R_o = 0.625$, $m = 0.1$ and $\theta = 45°$. The calculating result of the swirl number is 0.827 for NSC and 0.814 for CSC. As we will see in the following sections, the significant influence of cross-drilled swirler on the combustion performance is not caused by the slightly decreased swirler number. Such a small change of swirl number cannot have significant influence, as demonstrated in the present simulation. Similar conclusions were also reported by [177].

Excess air factor α is the ratio of the actual air-to-fuel ratio to the stoichiometric air-to-fuel ratio. $\alpha = 5.12$ was used in the present experiment.

4.3 Numerical Methodology

The Reynolds Average Navier-Stokes (RANS) calculation for both non-reacting cold flow and combustion were conducted by using the commercial software FLUENT and further validated by the experimental results in the present study. It is recognized that LES has become increasingly prevalent in the simulation of turbulent combustion. However RANS with the widely used Realizable k–ε model was adopted in the present study based on the considerations that only time-average flow fields were considered and measured in the study, that LES is computationally demanding for the present problem as the Reynolds number $Re = 2\,\rho U R_o/\mu$, is as high as 140,000, and that the swirler combustor has a complex three-dimensional geometry, which poses an additional challenge to LES. The total grid number of the unstructured tetrahedral mesh, which is shown in Fig. 4.3(c), is about 2,630,000 and the simulation results did not show significant difference if we refined the mesh further.

The gas flow was simulated in the Eulerian framework while the liquid kerosene droplets, which are injected at (0, 0, 5) with a cone angle of 60°, were simulated by using the discrete phase model (DPM). This model can calculate the trajectories of fuel droplets in the swirl flow by solving the particle equilibrium equation. In the present simulation, kerosene droplets of a uniform diameter of 40 μm are injected into the combustion chamber and the processes of droplet collision and breakup were neglected. Because fuel and air entered separately into the combustor, non-premixed combustion model was used to simulate combustion process of fuel/air mixture. The interaction physics of turbulent flow and chemical reaction was described by non-premixed probability density function (PDF) model, which is known as the standard pre-assumed β-PDF method with the standard transport equation for the mean mixture fraction and mixture fraction variance [178]. $C_{12}H_{23}$ was used as a simplified kerosene surrogate and chemical equilibrium assumption was used to calculate the PDF table. It is known that detailed chemical kinetics modeling is necessary for predicting near-limit combustion phenomena, such as local extinction and auto ignition of flame, and the concentrations of minor species such as NOx and light HC. Since the statistically steady characteristics of velocity and temperature in the combustor is the main focus of the study, the RANS or LES computation with detailed chemical kinetics will be considered in future study. The SIMPLE algorithm was used to calculate the pressure-velocity coupling. Moreover, a segregated solver was chosen to compute the whole physical process, with solution residual being smaller than 10^{-3} for continuity and 10^{-6} for energy. All the numerical calculations are carried out by using second-order upwind discretization scheme. The incoming flow velocity and the pressure output were applied as boundary conditions at the entrance and exit of the combustor, respectively. The temperature of the combustion chamber wall was fixed at the room temperature since cooling water was used in the experiment. P1 radiation model was adopted to model radiation heat loss from the combustor [179]. The constant value inlet condition for air flow and constant temperature condition for the boundary wall was applied. The temperature value is set as 300K at the burner wall since the water cooling system was used as shown above.

4.4 Results and Discussion

4.4.1 Non-reacting Flows

For the dual purposes of understanding the influence of centerbody air injection on the swirling flow and validating the RANS calculation, we conducted experiments for both CSC and NSC under non-reacting flow condition. Fig. 4.4 shows the experimental results for velocity distribution for a representative case, in which the incoming airflow was fixed at 25*m/s* and no liquid fuel was injected. Fig. 4.4(a)-(g) show the comparison between the measured and calculated axial velocity distribution at the axial locations z/D = 1，2，3，4，5，6 and 7 respectively, D =50mm is the diameter of the centerbody. It is seen that the simulation results agree well with the experiment results for both CSC and NSC, suggesting the time-average velocity fields can be correctly described by the present RANS simulation.

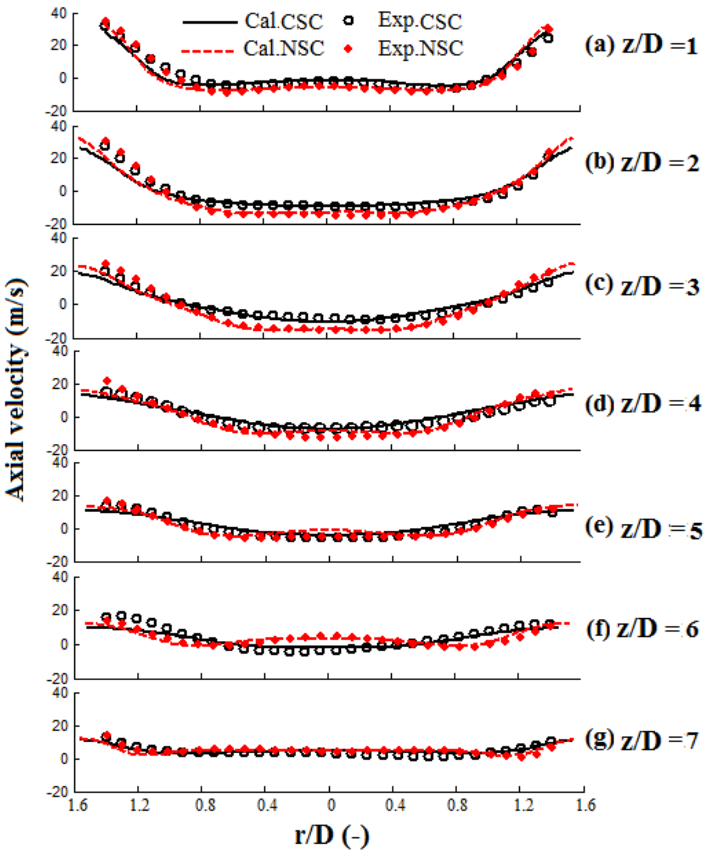

Fig.4.4: Comparison between measured and calculated radial distributions of axial velocity at different axial locations in CSC and NSC. Cal. and Exp. denote the calculated and experimental data, respectively. (a)-(g) represent the axial locations z/D= 1,2,3,4,5,6 and 7.

Several observations can be made about the flow characteristics in the CSC and NSC. First, negative axial velocities emerge around the z-axis all along from z/D =1(Fig. 4.4a) to z/D=6 (Fig. 4.4f), indicating the existence of CRZ as we expected. Specifically, the difference of the axial velocities between the CSC and the NSC increases along the z-axis until z/D=3 and then decrease until at z/D=5 where the axial velocity in the NSC along the center line (r=0) becomes positive. At z/D=6, the axial velocities in the NSC is positive while those in the CSC within the region of r/D ≤0.6 are still negative, indicating z/D=6 is still within the CRZ of the CSC. Beyond z/D=7, the axial velocities of CSC and NSC are all positive and have almost the same distribution, as shown in Fig. 4.4g. In addition, the axial velocity outside the CRZ is smaller in CSC than that in NSC because a portion of the incoming airflow enters into the combustor as the centerbody air injection in CSC instead of all in the swirling flow in NSC

Fig. 4.5 gives the distributions of the axial velocity and the recirculation zone strength (RZS), which will be defined later, pressure in CSC (Fig. 4.5a) and NSC (Fig. 4.5b). For a clarified presentation of the CRZ, which can be characterized as a backflow with negative axial velocities, the positive velocities are not shown in the figure. It is seen that the backflow in CRZ has the tendency of increasing and then decreasing along the axial direction between z/D=1 and 6 for both CSC and NSC. Furthermore, the maximum (most negative) backflow velocity in the CSC occurs in a small, secondary recirculation zone surrounded by the cross-drilled hole flows, while the maximum backflow velocity in the NSC occurs in the middle of the CRZ.

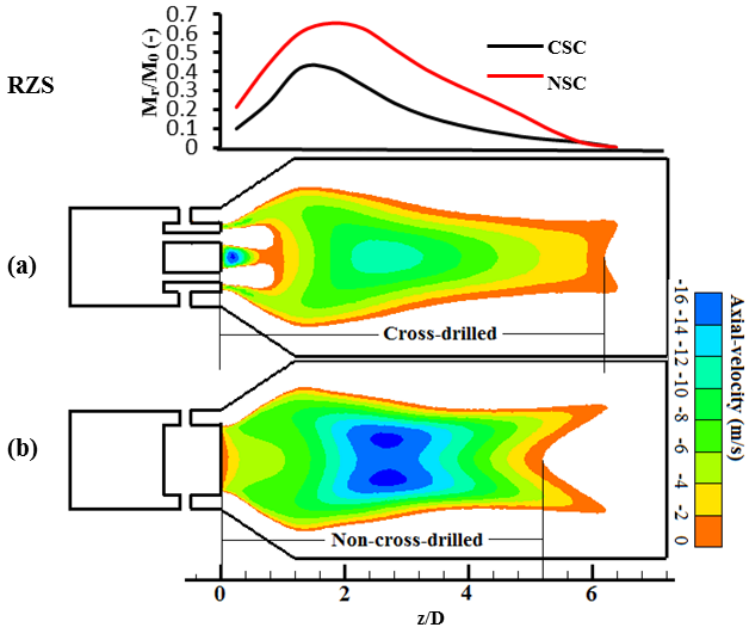

Fig.4.5: Distribution of recirculation zone strength and axial-velocity for (a): CSC and (b): NSC under non-reacting condition. RZS: recirculation zone strength.

It is seen that the geometry and structure of CRZ are distinctly different for CSC and NSC. Specifically, the length of the CRZ, [180] defined as the axial distance between the swirler and the farthest downstream of negative axial velocity, is found to be overall larger in CSC than that of NSC. In addition, the farthest downstream of the CRZ along the center line (r=0) is about z/D=6.5 in the CSC, which is much larger than z/D=5.5 in the NSC. To further quantify the role of centerbody air injection in modifying CRZ, we followed [176] to introduce a recirculation zone strength defined as the ratio of the recirculated mass flow rate and the combustor inlet mass flow rate M_0,

$$\text{RZS} = \frac{1}{M_0}\int_0^R 2\pi r\left(\frac{\sqrt{v^2}-v}{2}\right)\rho dr \tag{4.3}$$

Where R is the radius of recirculation flow cross section, v the axial velocity and ρ the density. The term $\sqrt{v^2}-v$ ensures the integrand to include only the negative axial velocity, i.e. within the CRZ. It is seen in Fig. 4.5 that the peak value of the recirculation zone strength of CSC is about 40% smaller than that of NSC. This is mainly due to the weakening effect of the centerbody air injection on the recirculating flow. However, the circulation zone strength decreases much more rapidly in NSC than does it in CSC, being consistent with our observation on the CRZ length.

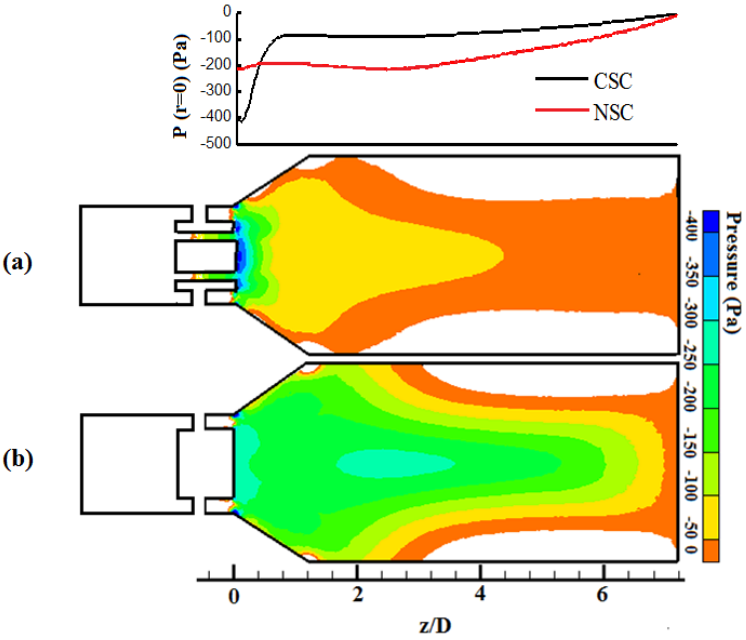

1.

Fig.4.6: Distribution of pressure for (a): CSC and (b): NSC under reacting condition. “P(r=0) (Pa)” shows the variation of the pressure along the center line (r = 0) of the combustors.

To further elucidate the different flow characteristics in the CRZs of CSC and NSC, the pressure variations are shown in Fig. 4.6. The pressure variation in NSC is the same as that in a traditional gradual-expansion swirl combustor. Specifically, the whole combustor can be divided into two pressure regions, namely the upstream region of negative pressure gradient and the downstream region of positive (adverse) pressure gradient, as clearly shown in Fig. 4.6 for center line pressure, $p(r=0)$. The two regions meets at the minimum pressure around z/D=2.6 as the entrainment of the swirling flow develops to its maximum extent at this location. In the CSC, the centerbody air injection from the cross-drilled openings makes the pressure variation different from that in the NSC. Specifically, the existence of the small, secondary recirculation zone in the immediate downstream of the swirler makes the pressure decreases and then increases drastically within the region of $0 < z/D < 0.8$, as a result of the entrainment of the air injection flows. Beyond the secondary recirculation zone, the pressure variation is mainly affected by the swirl flow as it does in the NSC. Due to the reduced adverse pressure gradient, the length of CRZ in CSC is overall larger than that in NSC.

It should be noted that the centerbody air injection will slightly reduce the effective swirl number from $S=0.827$ in NSC to $S=0.814$ in CSC. To rule out the possibility that the distinctive CRZ velocity and pressure characteristics is caused by the reduced swirl number, we repeated the above non-reacting flow calculation without centerbody air injection with these two swirl numbers. The almost identical results suggest that the slightly reduced swirl number can not cause any significant influence on the velocity and pressure distributions. Based on the observations the air flows injected from the cross-drilled openings mainly influences the flow pattern in the CRZ. Particularly, the injected air pushes the CRZ to the downstream hence lengthens the CRZ, head-on encounters the reversed flow consequently weakens it, and fills into the CRZ resulting in a reduced adverse pressure gradient in CRZ.

4.4.2 Reacting Flows.

To analyze and compare the flow and combustion characteristics of CSC and NSC, we simulated the reacting swirling flows in the CSC and NSC. The airflow was fixed at 25*m/s* and the mass flow rate of liquid fuel is 1.0g/s.

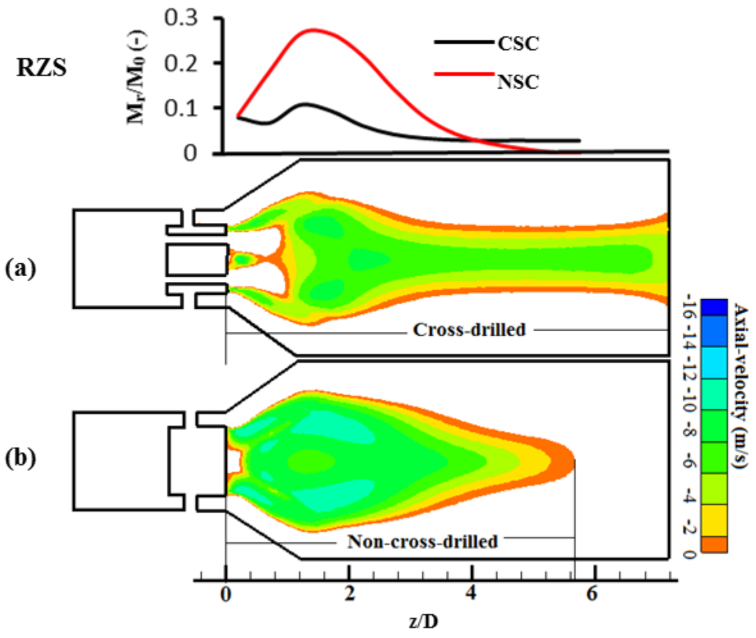

Fig.4.7: Distribution of recirculation zone strength and axial-velocity for (a): CSC and (b): NSC under reacting condition. RZS: recirculation zone strength.

Several observations can be made towards the changed flow characteristics of the CRZ in both CSC and NSC under reacting flow condition. First, it is seen in Fig. 4.7 that the length of CRZ in CSC is substantially increased compared with that under the non-reacting flow condition. The peak value of the recirculation zone strength of CSC decreases from that of NSC by about 70%. Such a substantial reduction may be caused by both the centerbody air injection (similar to the non-reacting flow conditions) and the stronger thermal expansion of high-temperature CRZ gases in CSC, to be discussed shortly in the following text.

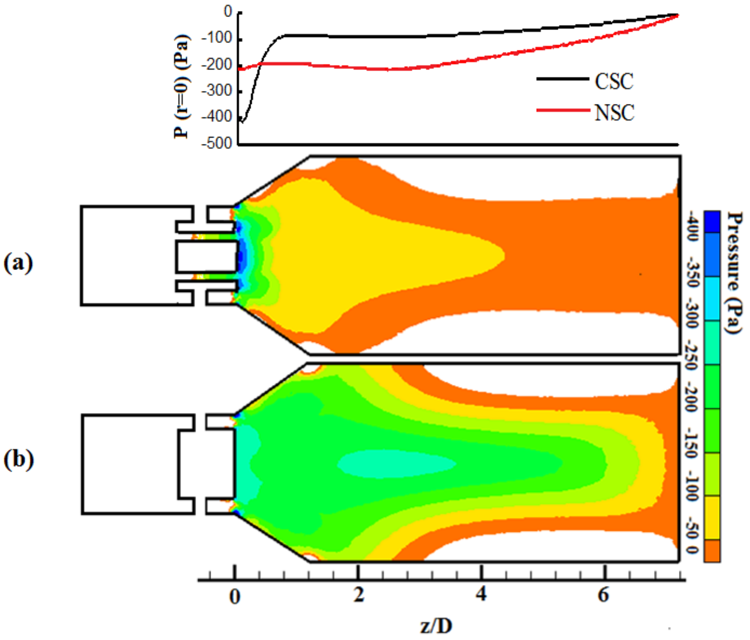

Fig.4.8: Distribution of pressure for (a): CSC and (b): NSC under reacting condition. “P(r=0) (Pa)” shows the variation of the pressure along the center line (r = 0) of the combustors.

The pressure contour in the combustor together with the pressure distribution along the center line (r=0) are shown in Fig. 4.8. It is seen that the secondary recirculation zone surrounded by the cross-drilled hole flows almost disappears compared with its counterpart under the non-reacting condition. This may be due to the fuel injection counteracting the pressure rise due to the entrainment of the centerbody air injection. Compared with the non-reacting flow condition where the negative and positive pressure gradient alternately appears, the whole combustion flow field can be divided into two regions of adverse pressure gradient. The adverse pressure gradient between z/D=1 and z/D=6 is significantly smaller than that under the non-reacting condition, causing the increase of the length of the CRZ. It is also seen that the length of the CRZ in the NSC is moderately decreased compared with that under the non-reacting flow condition. A possible explanation is based on the observation that combustion in NSC is more concentrated in the two high-temperature branches instead of in the center region, as shown in Fig. 4.9. As a result, the decrease of the adverse pressure gradient due to combustion in NSC is not as significant as that in CSC, as can be seen in Fig. 4.8. The moderately decreased length of the CRZ may be due to the increased viscosity of the gas, which facilitates the viscous dissipation and deceleration of the swirling flow.

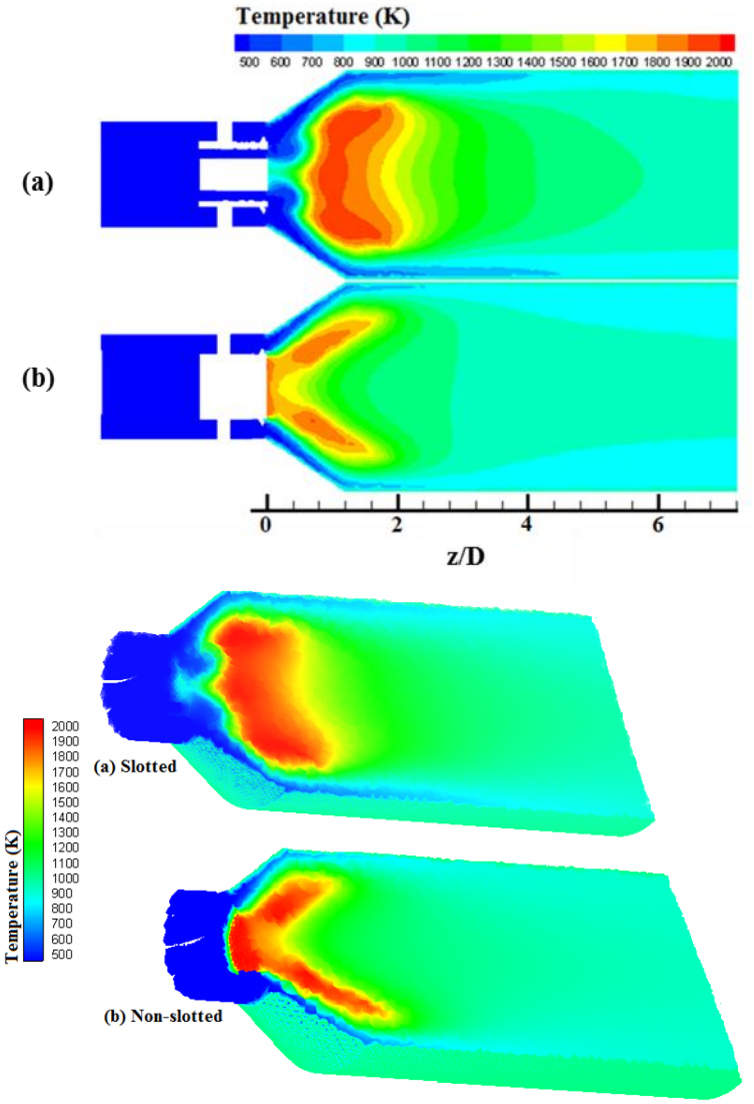

Fig.4.9: Distribution of temperature for (a): CSC and (b): NSC under reacting condition.

In order to examine the mixing process of the kerosene fuel with the air, we calculated the mean mixture fraction, as shown in Fig. 4.10 for the CSC and the NSC, respectively. The stoichiometric mixture fraction for kerosene, which is approximated by the chemical formula $C_{12}H_{23}$, is 0.0625. It is seen that there is an extended region of the near-stoichiometric mixture in the CSC compared with the bifurcated distribution of mixture fraction in the NSC, implying more complete combustion and higher temperature in the CSC than the NSC. This is further substantiated by the calculated temperature contours for the CSC and the NSC, as shown in Fig. 4.9, respectively. This is the most remarkable characteristics of centerbody air injection in enhancing the combustion performance by modifying the local stoichiometry in the vicinity of fuel injection. Furthermore, the high temperature region in the CSC is moved to the downstream of the swirler by the cross-drilled holes flows and therefore reduces the overheating problem to the fuel injector, as we expected.

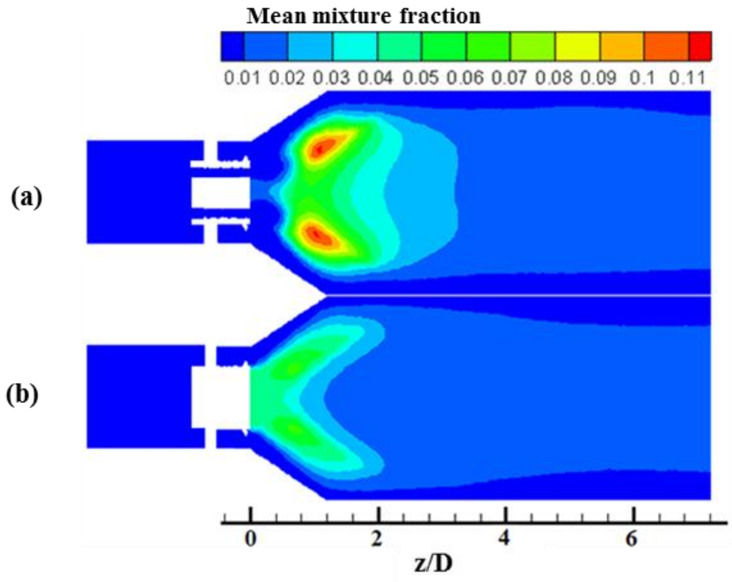

Fig.4.10:Distribution of mean mixture fraction for (a): CSC and (b): NSC under reacting condition.

To validate the present simulation results for swirl combustion, we compared the measured and calculated radial distribution of temperature at different axial locations, as shown in Fig. 4.11. Overall, the simulation results agree reasonably with the experimental results. However, relatively large discrepancies can be found in the region near the combustor wall. Such discrepancies may be due to the underestimated heat loss, the inaccurate assumption of infinitely fast reaction rate adopted in the PDF combustion model, and the oversimplified fuel atomization models. All of them would make the simulated temperatures are higher than the measured ones. Temperature measurement with higher accuracy and LES with detailed chemistry and spray models are certainly merited and will be considered in future work.

As seen in Fig. 4.11, a substantially higher temperature occurs in the CRZ ($r/D \leq 0.8$) of the CSC than that in NSC in the downstream of the swirler, say, $z/D=1$, at which the temperature difference is larger than 700 *K*. The flame formed in the CRZ is called as permanent flame which is expected to be on duty in igniting fuel-gas in combustor and therefore guarantee the flame stabilization. It is also seen that the main combustion process in the CSC happened in the CRZ results in lower near-wall and near-nozzle temperature. Because the same amount of fuel and air was burned in the CSC and the NSC, the higher temperature at exit of the CSC than that of NSC denotes that the combustion in the CSC is more complete than that in the NSC.

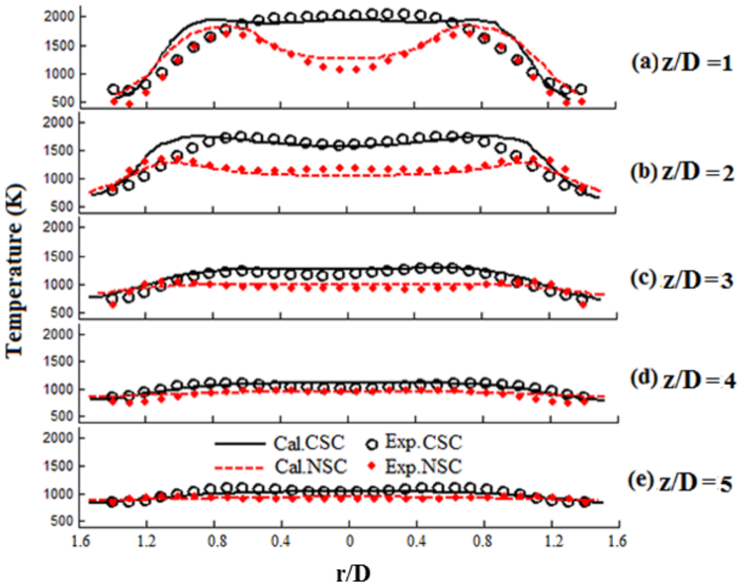

Fig.4.11: Comparison between measured and calculated radial distributions of temperature at different axial locations in CSC and NSC. Cal. and Exp. denote the calculated and experimental data, respectively. (a)-(e) represent axial locations z/D = 1, 2, 3, 4 and 5.

In the present study, the CO_2 concentration at the exit of the combustors was measured by a fuel-gas analyzer in order to estimate the overall combustion efficiency [170, 181, 182]:

$$\eta = 1-(T_{gas}-T_{air})(\frac{V_{dry}\cdot c_{p,m}\cdot \phi(CO_2)_{\max}}{H_{gas}\cdot \phi(CO_2)^2}+\frac{V_{H_2O}\cdot c_{p,m(H_2O)}}{H_{gas}}) \tag{4.4}$$

Here, η is combustion efficiency; T_{gas} and T_{air} are temperature from gas and environment respectively; H_{gas} is net heat produced by gas; $\Phi(CO_2)$ is the measured mass fraction of CO_2 emission; Volume of dry flue gas and water vapor are shown as V_{dry} and V_{H2O}; $c_{p,m}$ and $c_{p,m(H2O)}$ are specific heat for gas and water vapor; $\Phi(CO_2)$max is the maximum amount of CO_2 production when fuel reacts thoroughly.

The result of combustion efficiency calculation is 82% for CSC and 71% for NSC. In the present experiment, it may be due to the heat loss through the water-cooling chamber wall that results in lower combustion efficiency than the prevalent efficiency of modern gas-turbine combustors.

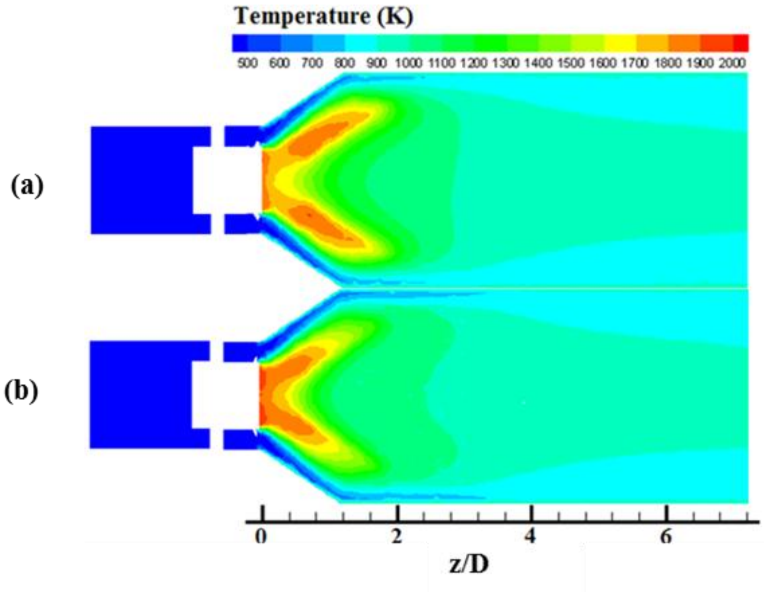

Fig.4.12: Simulated temperature results comparison between non-cross-drilled swirl combustors with different swirl number. a:S=0.827, b:S=0.814.

In order to further clarify the role of cross-drilled swirler, we repeated the above simulation and compared the temperature distributions of non-cross-drilled swirler combustion with two swirl numbers of S=0.827 and S=0.814, as shown in Fig. 4.12 and 4.13. The slightly smaller swirl number is the same as swirl number of the cross-drilled swirler as a result of the axial injection of air. It is seen that such a small change of swirl number does not cause any significant influence on the temperature distributions at various axial locations, demonstrating that the prominent influence of cross-drilled swirler is not a result of reducing the effective swirl number.

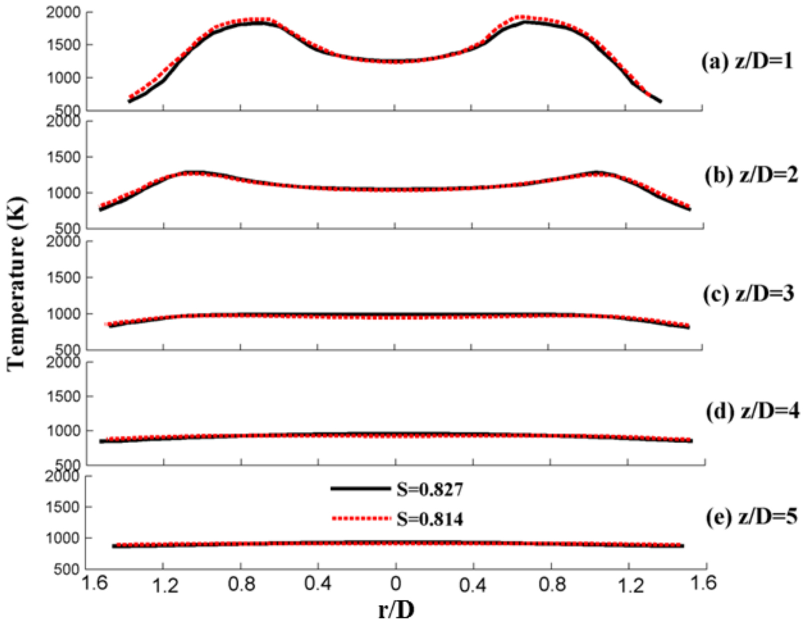

Fig.4.13: Simulated temperature results comparison at different axial locations in non-cross-drilled swirl combustors with different swirl number.

4.5 Parametric Study

To further demonstrate the advantages of CSC over NSC in enhancing the combustion efficiency and flame stabilization, we conducted a parametric study for the influence of the airflow velocity and excess air factor on the performance of the cross-drilled swirler. A wide ranges of airflow velocities, including 15*m/s*, 20*m/s*, 30*m/s* and 35*m/s*, and excess air factors, including 4.0, 4.5, 5.5 and 6.0, were considered in the simulation.

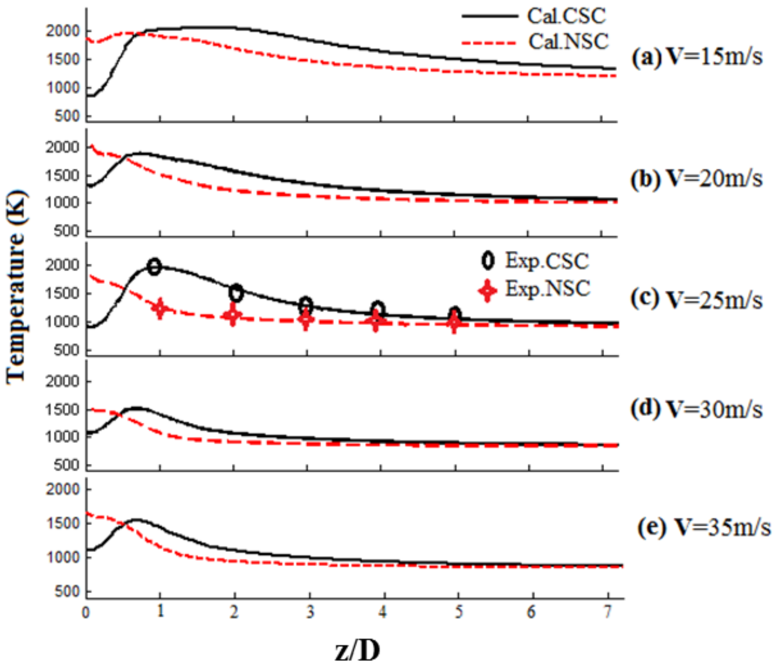

Fig.4.14: Comparison between measured and calculated temperature (r=0) at different axial locations in CSC and NSC. Cal. and Exp. denote the calculated and experimental data, respectively. (a)-(e) represent the incoming airflow velocity V=15,20,25,30 and 35m/s respectively.

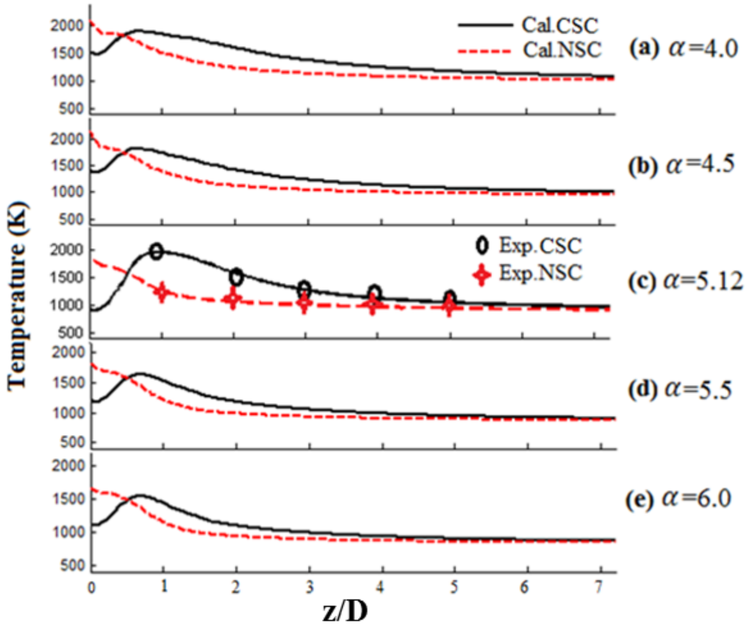

Fig.4.15: Comparison between measured and calculated temperature (r=0) at different axial locations in CSC and NSC. Cal. and Exp. denote the calculated and experimental data, respectively. (a)-(e) represent the excess air factor α= 4.0, 4.5, 5.12, 5.5 and 6.0 respectively.

Fig. 4.14 shows the variation of temperature at r=0 along the z-axis for both CSC and NSC and for various airflow velocities. The results for the representative case, in which the airflow velocity is 25m/s and the excess air factor is 5.12, are also shown in the figure for comparison. It is seen that the CSC always results in a wider distribution of higher temperature compared with the NSC, implying an improved combustion performance. In addition, the highest temperature occurs in the 30-50 mm downstream of the swirler in the CSC while the highest temperature almost always appears at the entrance in the NSC. These results suggest that the over-heating problem would be relieved by using CSC to push the high temperature combustion region to the downstream. Fig. 4.15 displays the variation of temperature at r=0 along the z-axis for both CSC and NSC and for various excess air factors. Again, the results for the representative case are also shown in the figure for comparison. It is seen that the CSC shows better performance in enhancing the combustion temperature although the extent of the enhancement varies with the airflow velocity and the excess air factor. Specifically, the highest temperature in the CSC decreases with increasing the airflow velocity and the excess air factor, indicates the decreasing influence of the cross-drilled swirler in combustion temperature. Optimization design is merited in future study by considering different swirl number, number and shape of cross-drilled holes to maximize the influence of CSC. More detailed flow and temperature information can be found in

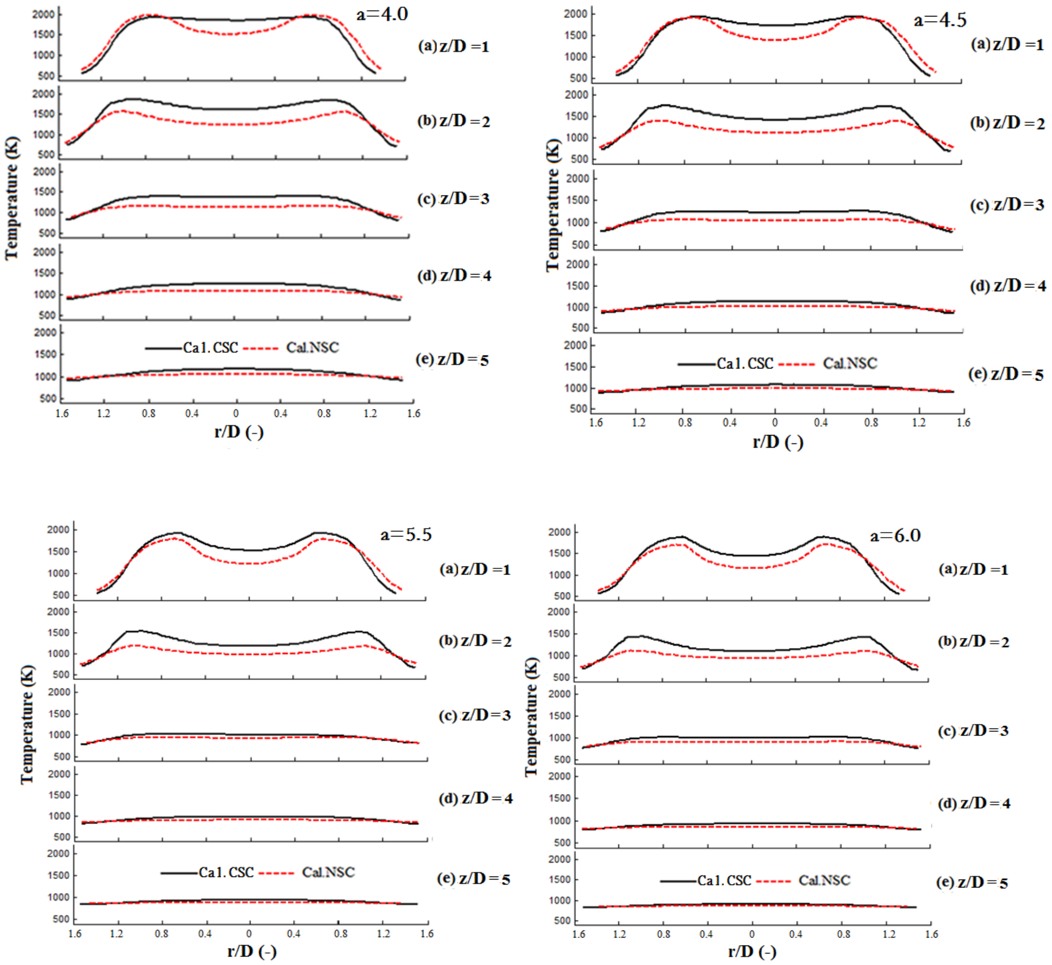

Fig.4.16: Simulated temperature results comparison at different axial locations between CSC and NSC with different excess air factors.

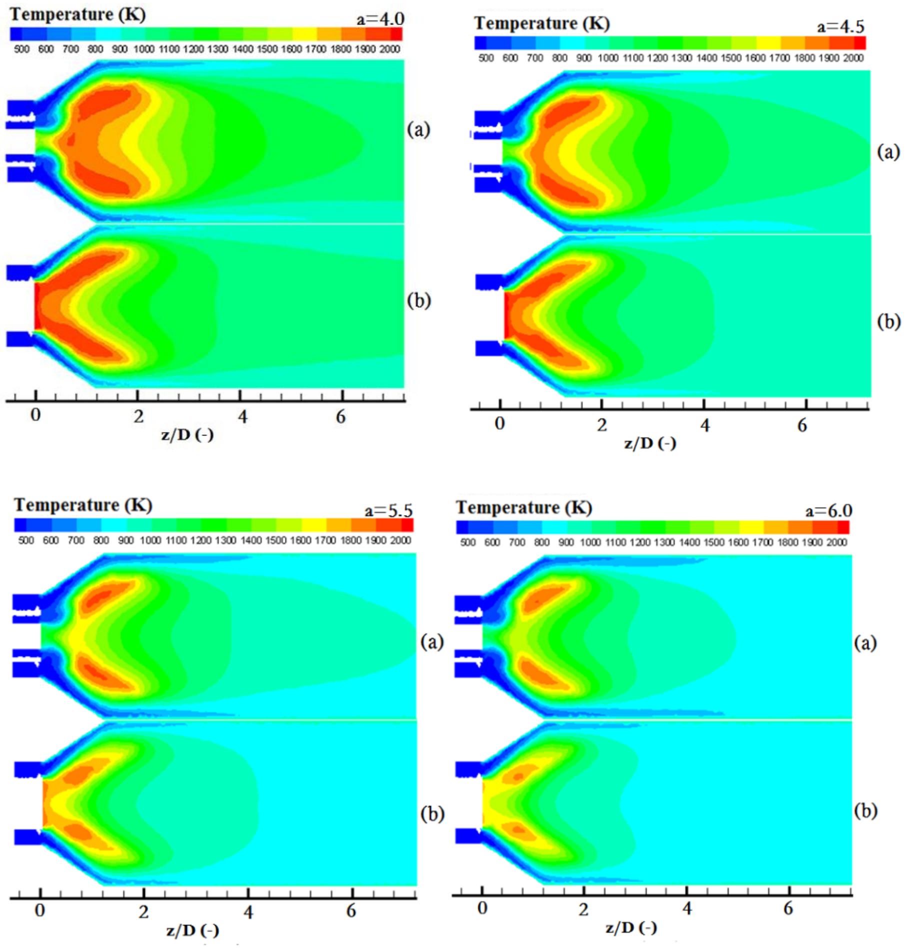

Fig.4.17: Simulated temperature contour comparison between CSC (a) and NSC (b) with different excess air factors.

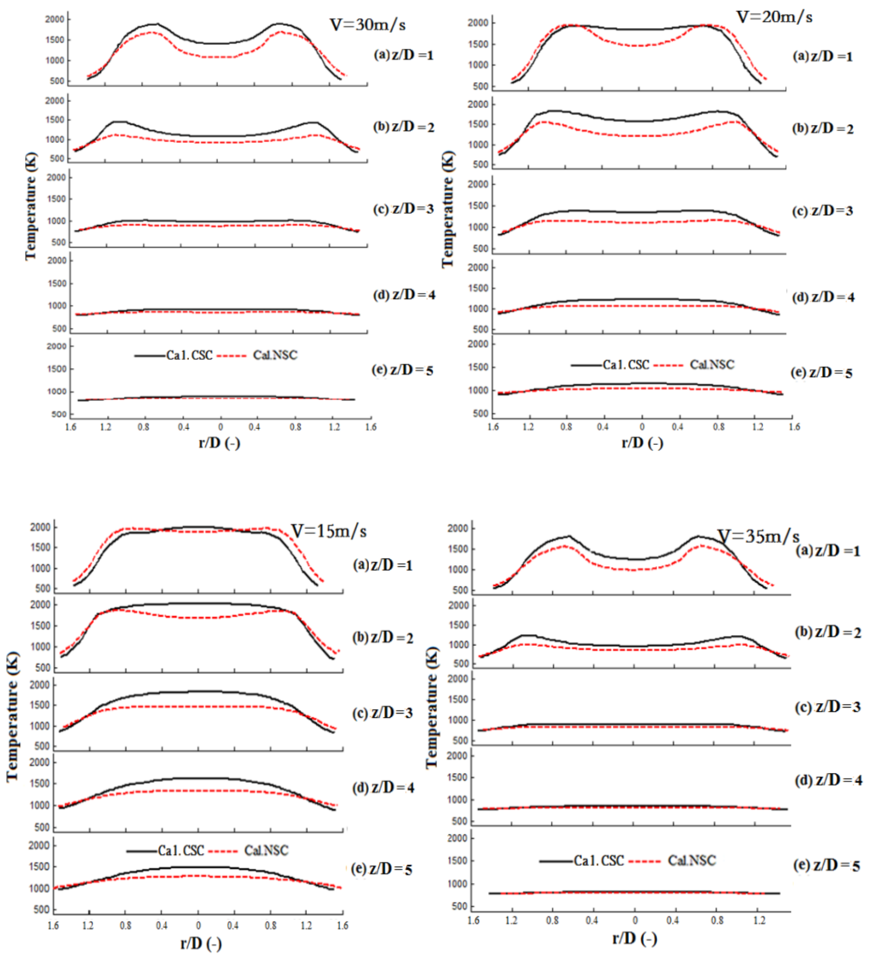

Fig.4.18: Simulated temperature results comparison at different axial locations between CSC and NSC with different incoming airflow velocities.

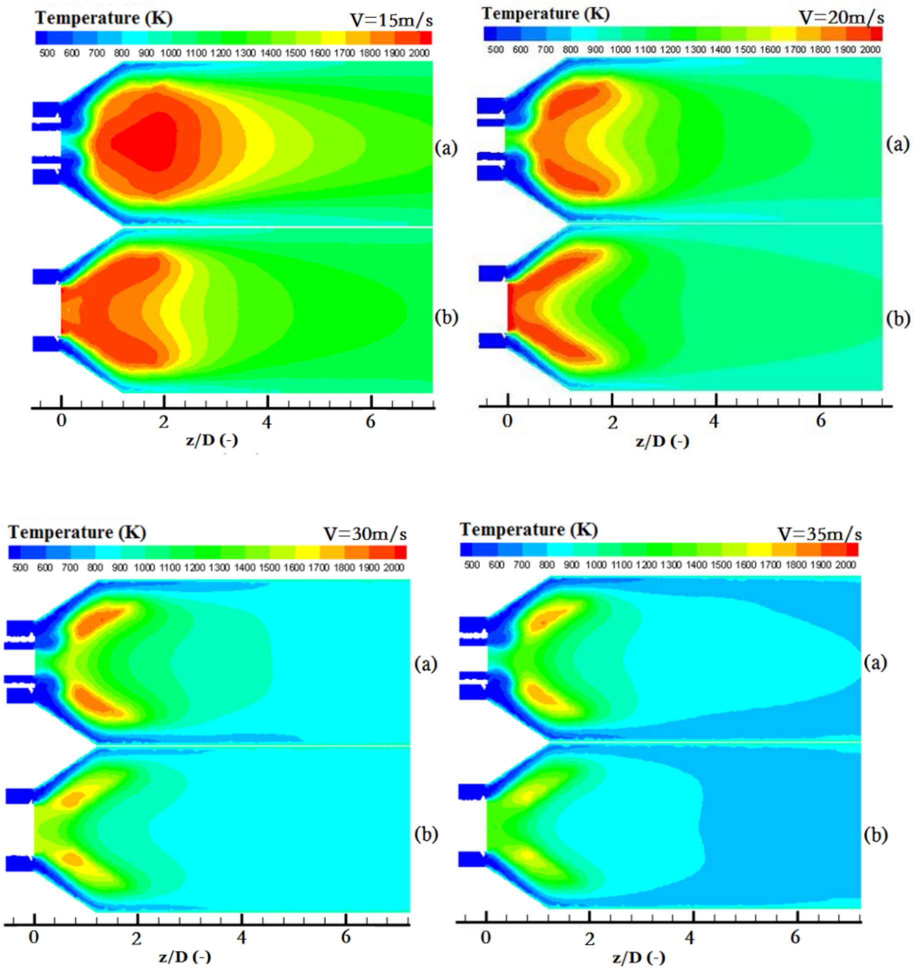

Fig.4.19: Simulated temperature contour comparison between CSC (a) and NSC (b) with different incoming airflow velocities.

4.6 Summary of Part III

Experimental study and RANS calculation were conducted for investigating the flow characteristics of combustors with or without centerbody air injection under both non-reacting and reacting flow conditions. The simulation results show reasonably good agreement with the experimentally measured velocity and temperature distributions. In all the examined cases for different incoming airflow velocities and excess air factors, the CSC shows improved combustion performance by increasing the highest combustion temperatures, widening the high temperature combustion region and pushing the high temperature region to the farther downstream of the swirler to relieve the heating problem of the swirler and the fuel nozzle. The improved performance is not a consequence of the slightly reduced swirl number, but a consequence of modifying the flow characteristics of the central recirculation zone (CRZ) by introducing a portion of incoming airflow directly to the combustion through the cross-drilled holes on the swirler. In general, the centerbody injecting flows can increase the length of the CRZ, reduce the recirculation zone strength in the CRZ, and concentrate the fuel injection in the CRZ instead of carrying to the side walls by the swirling flow. Consequently, the fuel/air mixture has a wider region of near-stoichiometry in the CRZ, which render the enhanced combustion efficiency. It is noted that the performance of the combustor with centerbody air injection also depends on other factors such as the airflow velocity and the excess air factor, which were examined in a parametric simulation study. Future work on high-accuracy flow measurements and LES simulation with advanced models for chemistry-turbulence interaction and fuel spray is merited to solve the existing discrepancies between the measured and calculated temperature distribution. Optimization design is also worth future study by considering different swirler design and swirl number. The unsteady combustor characteristics, which was not considered in the present study, is certainly another interesting and worthwhile topic for future study.

5 Conclusion

In the present work, the influence of flow characteristics on a oscillating IDF, steady IDF and a liquid gas turbine combustion has been investigated experimentally and numerically. The conclusion can be summarized as follows:

1. In the research of the oscillation of IDF, both non-reacting and reacting IDFs are investigated by experiments and 3-dimensional unsteady LES. PIV measurement is performed and results are used for qualitative and quantitative validation of the numerical prediction in non-reacting flow. Steady and unsteady flow information is obtained through LES to have a further insight into the flow. A wide range of cases are examined numerically and result comparison provides a detailed understanding of the non-reacting IDF flow transition to turbulence. LES combined with infinite fast irreversible chemical reaction is used to study the reacting IDF dynamics. With the comprehensive analysis, it is concluded that,For non-reacting IDF, flow shear is firstly produced in the central tube due to the shear effect between inner flow and the central tube wall. This shear combined with a flow shear between the inner heavier flow and the outer lighter flow constitutes the initial flow shear. Flow turbulence intensity in very near field increases when the Richardson number approaches to unit at which flow shear term equals to buoyance term. Unlike the absolute buoyance instability, the IDF flow transition to turbulence is caused by an opposite direction buoyance effect impacts on the initial flow shear. Instability occurs in a very near field with asymmetry flow pattern is a particular feature for IDF among buoyance driven jet flows.

In reacting IDFs, oscillation in instantaneous experimental and numerical flames is discussed. Due to gravitational effect, vortex stretching and baroclinic torque, reacting flow turns to unstable after evolve for an enough long distance. It is observed experimentally and numerically that IDF oscillation only happens in the upper region the flame with the bottom part keeping stable. By comparing and analyzing the vertical structure for non-reacting flow and reacting flow, it is identified flow is relatively stable in the vicinity of the flam bottom. The stable near field flow is mainly because combustion chemical heat source decreases the inner flow density to reverse buoyance effect direction. On the contrary to that in non-reacting flow, buoyance effect induced vorticity in reacting flow has a same direction with the initial flow shear, so that there are not extra vortices produced in the vicinity of the flame to interact with the flow shear induced vortices. The flame oscillation in IDFs is investigated and explained.

2. Experimental and numerical study has been performed on various steady methane IDFs with variable fuel and air inlet velocities. The flame height, structure and appearance for different inlet conditions have been obtained. Laminar simulation combined with radiation and soot formation model have been conducted and validated by a published paper. Using the detailed information in simulation, the flame structure and soot formation characteristics have been analysed. It is concluded that,

   By fixing the air inlet velocity, increasing fuel flow rate will firstly decrease flame height. Starting from a specific value, further increasing fuel inlet velocity cause no obvious flame height change. Due to the higher fuel velocity, the residence time for soot formation is shorten leading to less soot volume fraction in the downstream of the flame.

Flame height extends to downstream when air inlet velocity increases. The extension rate is linearly related to the air inlet velocity. Due to the higher flame temperature, larger high-temperature region and longer residence time, soot formation rate and soot volume fraction increases when raising the air flow rate.

The results can be used as a reference for the research of IDFs.

3. In the research of liquid gas turbine combustion, it is found that center air injection increases the peak value of combustion temperature, widens the high temperature combustion region and pushes the high temperature region to the farther downstream of the swirler to relieve the heating problem of the swirler and the fuel nozzle. The improved performance is not a consequence of the slightly reduced swirl number but introducing a portion of incoming airflow directly to the CRZ through the cross-drilled holes on the swirler to result in a wider region of near-stoichiometry and a longer residence time. The performance of the cross-drilled swirler also depends on other factors such as the airflow velocity and the excess air factor.

References

[[1] A. Tewarson, J. Steciak, Fire ventilation, Combustion and flame 53 (1983) 123-134.

[2] W.M. Pitts, The global equivalence ratio concept and the formation mechanisms of carbon monoxide in enclosure fires, Progress in energy and combustion science 21 (1995) 197-237.

[3] T.R. Barfknecht, Toxicology of soot, Progress in energy and combustion science 9 (1983) 199-237.

[4] H.-G. Neumann, Health risk of combustion products: toxicological considerations, Chemosphere 42 (2001) 473-479.

[5] C.W. Lautenberger, J.L. de Ris, N.A. Dembsey, J.R. Barnett, H.R. Baum, A simplified model for soot formation and oxidation in CFD simulation of non-premixed hydrocarbon flames, Fire Safety Journal 40 (2005) 141-176.

[6] J.L. De Ris, P.K. Wu, G. Heskestad, Radiation fire modeling, Proceedings of the Combustion Institute 28 (2000) 2751-2759.

[7]

J. Arthur, D. Napier. Formation of carbon and related materials in diffusion flames. In: editor^editors. Symposium (International) on Combustion; 1955: Elsevier. p. 303-316.

[8] J. Kent, H.G. Wagner, A reversed coflowing laminar diffusion flame, Zeitschrift für Physikalische Chemie 139 (1984) 59-68.

[9] J. Walker, Flames in which air is introduced into a flammable gas rather than vice versa, Scientific American 241 (1979) 192-200.

[10]

I. Glassman. Soot formation in combustion processes. In: editor^editors. Symposium (international) on combustion; 1989: Elsevier. p. 295-311.

[11] C.R. Shaddix, T.C. Williams, L.G. Blevins, R.W. Schefer, Flame structure of steady and pulsed sooting inverse jet diffusion flames, Proceedings of the Combustion Institute 30 (2005) 1501-1508.

[12] C.R. Shaddix, T.C. Williams, Measurements of the velocity field in laminar ethylene inverse jet diffusion flames, Combust. Flame 156 (2009) 942-945.

[13] C. Kaplan, K. Kailasanath, Flow-field effects on soot formation in normal and inverse methane–air diffusion flames, Combust. Flame 124 (2001) 275-294.

[14] L.G. Blevins, R.A. Fletcher, B.A. Benner, E.B. Steel, G.W. Mulholland, The existence of young soot in the exhaust of inverse diffusion flames, Proc. Combust. Inst. 29 (2002) 2325-2333.

[15] V.R. Katta, L.G. Blevins, W.M. Roquemore, Dynamics of an inverse diffusion flame and its role in polycyclic-aromatic-hydrocarbon and soot formation, Combustion and Flame 142 (2005) 33-51.

[16] G.W. Sidebotham, I. Glassman, Flame temperature, fuel structure, and fuel concentration effects on soot formation in inverse diffusion flames, Combustion and flame 90 (1992) 269-283.

[17] D. Makel, I.M. Kennedy, Soot formation in laminar inverse diffusion flames, Combustion science and technology 97 (1994) 303-314.

[18] E.J. Lee, K.C. Oh, H.D. Shin, Soot formation in inverse diffusion flames of diluted ethene, Fuel 84 (2005) 543-550.

[19] D.S. Bento, K.A. Thomson, Ö.L. Gülder, Soot formation and temperature field structure in laminar propane–air diffusion flames at elevated pressures, Combustion and Flame 145 (2006) 765-778.

[20] R. Santoro, T. Yeh, J. Horvath, H. Semerjian, The transport and growth of soot particles in laminar diffusion flames, Combust. Sci. Technol. 53 (1987) 89-115.

[21] L.G. Blevins, R.A. Fletcher, B.A. Benner, E.B. Steel, G.W. Mulholland, The existence of young soot in the exhaust of inverse diffusion flames, Proc. Comb. Inst. 29 (2002) 2325-2333.

[22] K. Kang, J. Hwang, S. Chung, W. Lee, Soot zone structure and sooting limit in diffusion flames: Comparison of counterflow and co-flow flames, Combustion and Flame 109 (1997) 266-281.

[23] C.R. Shaddix, T.C. Williams, Measurements of the velocity field in laminar ethylene inverse jet diffusion flames, Combustion and Flame 156 (2009) 942-945.

[24]

K.-T. Wu, R.H. Essenhigh. Mapping and structure of inverse diffusion flames of methane. In: editor^editors. Symposium (International) on Combustion; 1985: Elsevier. p. 1925-1932.

[25] W. Krebs, P. Flohr, B. Prade, S. Hoffmann, Thermoacoustic stability chart for high-intensity gas turbine combustion systems, Combustion Science and Technology 174 (2002) 99-128.

[26] Y.S. Najjar, Gas turbine cogeneration systems: a review of some novel cycles, Applied thermal engineering 20 (2000) 179-197.

[27] W.B. WILLIAM, Fundamentals of gas turbines, 1984.

[28] J.M. Beer, N.A. Chigier, Combustion Aerodynamics, Applied Science Publishers LTD, London, (1972).

[29] N. Syred, J.M. Beer, Combustion in swirling flow: a review, Combust. Flame 23 (2) (1974) 143-201.

[30] D.G. Lilley, Combustion in swirl flows: a review, AIAA J 15 (1977) 1063-1067.

[31] A.K. Gupta, D.G. Lilley, N. Syred, Swirl Flows, Abacus Press, England, (1984).

[32] T.C. Lieuwen, Unsteady Combustor Physics, Cambridge University Press2012.

[33] N. Syred, A review of oscillation mechanisms and the role of the precessing vortex core (PVC) in swirl combustion systems, Prog. Energ. Combust. 32 (2006) 93-161.

[34] T.C. Lieuwen, Y. Neumeier, B.T. Zinn, The role of unmixedness and chemical kinetics in driving combustion instabilities in lean premixed combustors, Combust Sci Technol 135 (1998) 193-211.

[35] S. Candel, D. Durox, T. Schuller, P. Palies, J.-F. Bourgouin, J.P. Moeck, Progress and challenges in swirling flame dynamics, CR Mecanique. 340 (2012) 758-768.

[36] D.L. Rhode, D.G. Lilley, D.K. Mclaughlin, Mean flowfields in axisymmetric combustor geometries with Swirl, AIAA J. 21 (1983) 593-600.

[37] M. Ghaffarpour, B. Chehroudi, Experiments on spray combustion in a gas-turbine model combustor, Combust Sci Technol 92 (1993) 173-200.

[38] A. Valera-Medina, N. Syred, P. Bowen, Central recirculation zone visualization in confined swirl combustors for terrestrial energy, J. Propul. Power 29 (2012) 195-204.

[39] J.K. Eaton, J.P. Johnston, A review of research on subsonic turbulent flow reattachment, AIAA j. 19 (1981) 1093-1100.

[40] P.M. Anacleto, E.C. Fernandes, M.V. Heitor, S.I. Shtork, Swirl flow structure and flame characteristics in a model lean premixed combustor, Combust. Sci. Technol. 175 (2003) 1369-1388.

[41] R. Rawe, H. Kremer, Stability limits of natural gas diffusion flames with swirl, Proc. Combust. Inst. 18 (1981) 667-677.

[42] C. Schulz, V. Sick, Tracer-LIF diagnostics: quantitative measurement of fuel concentration, temperature and fuel/air ratio in practical combustion systems, Prog. Energ. Combust. 31 (2005) 75-121.

[43] V. Tangirala, R.H. Chen, J.F. Driscoll, Effect of heat release and swirl on the recirculation within swirl-stabilized flames, Combust. Sci. Technol. 51 (1987) 75-95.

[44] R. Chen, J.F. Driscoll, The role of the recirculation vortex in improving fuel-air mixing within swirling flames, Proc. Combust. Inst. 22 (1989) 531-540.

[45] V. Sankaran, S. Menon, LES of spray combustion in swirling flows, J. Turbul. 3 (2002) 1-23.

[46] C.W. Lee, S.Y. Moon, An experimental investigation of the effects of turbulence generators attached to an axial swirler nozzle on mixing and combustion, Aerosp. Sci. Technol. 6 (2002) 517-520.

[47] T. Terasaki, S. Hayashi, The effects of fuel-air mixing on NOx formation in non-premixed swirl burners, Proc. Combust. Inst. 26 (1996) 2733-2739.

[48] P.J. Bowen, T. O'Doherty, O. Lucca - Negro, Theoretical investigations of rotating instabilities, Dev. Chem. Eng. Min. Process. 7 (1999) 269-285.

[49] B. Guo, T.A. Langrish, D.F. Fletcher, CFD simulation of precession in sudden pipe expansion flows with low inlet swirl, Appl. Math. Model. 26 (2002) 1-15.

[50] B. Wegner, A. Maltsev, C. Schneider, A. Sadiki, A. Dreizler, J. Janicka, Assessment of unsteady RANS in predicting swirl flow instability based on LES and experiments, Int. J. Heat Fluid Fl. 25 (2004) 528-536.

[51] K.K.J. Ranga Dinesh, K.W. Jenkins, M.P. Kirkpatrick, W. Malalasekera, Effects of swirl on intermittency characteristics in non-premixed flames, Combust. Sci. Technol. 184 (2012) 629-659.

[52] Y. Huang, V. Yang, Effect of swirl on combustion dynamics in a lean-premixed swirl-stabilized combustor, Proc. Combust. Inst. 30 (2005) 1775-1782.

[53] T.C. Lieuwen, V. McDonell, D. Santavicca, T. Sattelmayer, Burner development and operability issues associated with steady flowing syngas fired combustors, Combust. Sci. Technol. 180 (2008) 1169-1192.

[54] T.C. Lieuwen, V. Yang, Combustion Instabilities in Gas Turbine Engines: Operational Experience, Fundamental Mechanisms and Modeling, AIAA2005.

[55] S. Terhaar, T.G. Reichel, C. Schrödinger, L. Rukes, C.O. Paschereit, K. Oberleithner, Vortex breakdown types and global modes in swirling combustor flows with axial injection, J. Propul. Power, (2014) 1-11.

[56] V. Tangirala, J.F. Driscoll, Temperatures within non-premixed flames-effects of rapid mixing due to swirl, Combust. Sci. Technol. 60 (1988) 143-162.

[57] F.Z. Sierra, A. Uribe, J. Kubiak, H. Lara, G. Urquiza, J. Nebradt, 3-dimensional pressure driven temperature field in a gas turbine combustion chamber, Proceedings of the ASME Turbo Expo 1 (2006) 23-30.

[58] D. Fang, J. Majdalani, M.J. Chiaverini, Simulation of the cold-wall swirl driven combustion chamber, AIAA Paper 5055 (2003) 2003.

[59] F.F. Grinstein, T.R. Young, E.J. Gutmark, G. Li, G. Hsiao, H.C. Mongia, Flow dynamics in a swirl combustor, J. Turbul. 3 (2002) 1-19.

[60] M.M. Kamal, Combustion characteristics of pulverized coal and air/gas premixed flame in a double swirl combustor, Combust. Sci. Technol. 181 (2008) 136-158.

[61] R.K. Cheng, D.T. Yegian, M.M. Miyasato, G.S. Samuelsen, C.E. Benson, R. Pellizzari, P. Loftus, Scaling and development of low-swirl burners for low-emission furnaces and boilers, Proc. Combust. Inst. 28 (2000) 1305-1313.

[62] D. Littlejohn, A.J. Majeski, S. Tonse, C. Castaldini, R.K. Cheng, Laboratory investigation of an ultralow NOx premixed combustion concept for industrial boilers, Proc. Combust. Inst. 29 (2002) 1115-1121.

[63] L.L. Zhao, Q.T. Zhou, C.S. Zhao, Flame characteristics in a novel petal swirl burner, Combust. Flame 155 (2008) 277-288.

[64] Y. Li, R. Li, D. Li, J. Bao, P. Zhang, Combustion characteristics of a slotted swirl combustor: An experimental test and numerical validation, Int. Commun. Heat and Mass, (2014).

[65] R. Qian, T. Wu, S. Jin, Y. Du, A new mechanism of flame stabilization, Journal of Combustion Science and Technology 6 (2011) 003.

[66] C.M. Coats, Coherent structures in combustion, Prog. Energy Combust. Sci. 22 (1996) 427-509.

[67] X. Jiang, K.H. Luo, Dynamics and structure of transitional buoyant jet diffusion flames with side-wall effects, Combust. Flame 133 (2003) 29-45.

[68] A. Liñán, E. Fernandez-Tarrazo, M. Vera, A.L. Sánchez, Lifted laminar jet diffusion flames, Combust. Sci. Technol. 177 (2005) 933-953.

[69] A. Liñán, M. Vera, A.L. Sánchez, Ignition, liftoff, and extinction of gaseous diffusion flames, Ann. Rev. Fluid Mech. 47 (2015) 293-314.

[70] G. Cox, Combustion fundamentals of fire, Academic Press(1995).

[71] L.D. Chen, J.P. Seaba, W. Roquemore, L. Goss, Buoyant diffusion flames, Proc. Comb. Inst. 22 (1989) 677-684.

[72] W.M.G. Malalasekera, H.K. Versteeg, K. Gilchrist, A review of research and an experimental study on the pulsation of buoyant diffusion flames and pool fires, Fire Mater. 20 (1996) 261-271.

[73] M.R.J. Charest, C.P.T. Groth, Ö.L. Gülder, Effects of gravity and pressure on laminar coflow methane–air diffusion flames at pressures from 1 to 60 atmospheres, Combust. Flame 158 (2011) 860-875.

[74] T.C. Williams, C.R. Shaddix, R.W. Schefer, P. Desgroux, The response of buoyant laminar diffusion flames to low-frequency forcing, Combust. Flame 151 (2007) 676-684.

[75] A. Datta, Effects of gravity on structure and entropy generation of confined laminar diffusion flames, Int. J. Therm. Sci. 44 (2005) 429-440.

[76] B.W. Albers, A.K. Agrawal, Schlieren analysis of an oscillating gas-jet diffusion flame, Combust. Flame 119 (1999) 84-94.

[77] T. Toong, Mechanisms of combustion instability, Proc. Comb. Inst. 10 (1965) 1301-1313.

[78] F.A. Williams, Combustion Theory 2nd ed., Addison-Wesley, Reading, MA,1985.

[79] E.E. Zukoski, Properties of fire plumes, Combustion Fundamentals of Fire, Academic Press, San Diego(1995).

[80] A.F. Ghoniem, I. Lakkis, M. Soteriou, Numerical simulation of the dynamics of large fire plumes and the phenomenon of puffing, Proc. Comb. Inst. 26 (1996) 1531-1539.

[81] A. Hamins, J.C. Yang, T. Kashiwagi, An experimental investigation of the pulsation frequency of flames, Proc. Comb. Inst. 24 (1992) 1695-1702.

[82] V.R. Katta, W.M. Roquemore, Role of inner and outer structures in transitional jet diffusion flame, Combust. Flame 92 (1993) 274-282.

[83] X. Jiang, K.H. Luo, Combustion-induced buoyancy effects of an axisymmetric reactive plume, Proc. Comb. Inst. 28 (2000) 1989-1995.

[84] B.M. Cetegen, K.D. Kasper, Experiments on the oscillatory behavior of buoyant plumes of helium and helium-air mixtures, Phys. Fluids 8 (1996) 2974-2984.

[85] J. Buckmaster, N. Peters, The infinite candle and its stability—a paradigm for flickering diffusion flames, Proc. Comb. Inst. 21 (1988) 1829-1836.

[86] T. Maxworthy, The flickering candle: transition to a global oscillation in a thermal plume, J. Fluid. Mech. 390 (1999) 297-323.

[87] P. Huerre, P.A. Monkewitz, Local and global instabilities in spatially developing flows, Ann. Rev. Fluid Mech. 22 (1990) 473-537.

[88] A. Lingens, K. Neemann, J. Meyer, M. Schreiber, Instability of diffusion flames, Proc. Comb. Inst. 26 (1996) 1053-1061.

[89] X. Jiang, K.H. Luo, Spatial direct numerical simulation of the large vortical structures in forced plumes, Flow Turbulence Combust. 64 (2000) 43-69.

[90] X. Jiang, K. Luo, Direct numerical simulation of the near field dynamics of a rectangular reactive plume, Int. J. Heat Fluid Flow 22 (2001) 633-642.

[91] X. Jiang, K. Luo, Combustion-induced buoyancy effects of an axisymmetric reactive plume, Proc. Comb. Inst. 28 (2000) 1989-1995.

[92] A. Sobiesiak, J.C. Wenzell, Characteristics and structure of inverse flames of natural gas, Proc. Comb. Inst. 30 (2005) 743-749.

[93] M.A. Mikofski, T.C. Williams, C.R. Shaddix, L.G. Blevins, Flame height measurement of laminar inverse diffusion flames, Combustion and Flame 146 (2006) 63-72.

[94] K.T. Kang, J.Y. Hwang, S.H. Chung, W. Lee, Soot zone structure and sooting limit in diffusion flames: Comparison of counterflow and co-flow flames, Combust. Flame 109 (1997) 266-281.

[95] U. Sen, T. Gangopadhyay, C. Bhattacharya, A. Mukhopadhyay, S. Sen, Dynamic characterization of a ducted inverse diffusion flame using recurrence analysis, Combust. Sci. Technol., (2017).

[96] K.T. Wu, R.H. Essenhigh, Mapping and structure of inverse diffusion flames of methane, Proc. Comb. Inst. 20 (1985) 1925-1932.

[97] G.W. Sidebotham, I. Glassman, Effect of oxygen addition to a near-sooting ethene inverse diffusion flame, Combustion Science and Technology 81 (1992) 207-219.

[98] H. Tennekes, J.L. Lumley, A first course in turbulence, MIT press1972.

[99] N. Peters, Turbulent combustion, Cambridge university press2000.

[100] P. Sagaut, S. Deck, M. Terracol, Multiscale and multiresolution approaches in turbulence: LES, DES and hybrid RANS/LES methods: applications and guidelines, World Scientific2013.

[101]

S. Pope. Computations of turbulent combustion: progress and challenges. In: editor^editors. Symposium (International) on Combustion; 1991: Elsevier. p. 591-612.

[102]

A.N. Kolmogorov. The local structure of turbulence in incompressible viscous fluid for very large Reynolds numbers. In: editor^editors. Dokl. Akad. Nauk SSSR; 1941: JSTOR. p. 301-305.

[103] S.B. Pope, Turbulent flows, IOP Publishing, 2001.

[104] W. Jones, B. Launder, The prediction of laminarization with a two-equation model of turbulence, International journal of heat and mass transfer 15 (1972) 301-314.

[105] D. Wilcox, Turbulence Modelling for CFD DCW Industries Inc, La Canada, California, (1998).

[106] F. Menter, M. Kuntz, R. Langtry, Ten years of industrial experience with the SST turbulence model, Turbulence, heat and mass transfer 4 (2003) 625-632.

[107] U. Piomelli, Large-eddy simulation: achievements and challenges, Progress in Aerospace Sciences 35 (1999) 335-362.

[108] T. Poinsot, D. Veynante, Theoretical and numerical combustion, RT Edwards, Inc.2005.

[109] C.K. Law, Combustion physics, Cambridge university press2006.

[110] H.G. Weller, G. Tabor, H. Jasak, C. Fureby, A tensorial approach to computational continuum mechanics using object-oriented techniques, Comp. Phys. 12 (1998) 620-631.

[111] R.I. Issa, Solution of the implicitly discretised fluid flow equations by operator-splitting, J. Comput. Phys. 62 (1986) 40-65.

[112] H. Jasak, Error analysis and estimation for finite volume method with applications to fluid flow, Ph.D. thesis, Imperial College of Science, Technology and Medicine, 1996.

[113] B. Leonard, Simple high‐accuracy resolution program for convective modelling of discontinuities, Int. J. Numer. Methods Fluids 8 (1988) 1291-1318.

[114] M. Darwish, A new high-resolution scheme based on the normalized variable formulation, Numer. Heat Transfer Part B 24 (1993) 353-371.

[115] M.T. Landahl, E. Mollo-Christensen, Turbulence and random processes in fluid mechanics, Cambridge University Press1992.

[116] A. D’anna, A. D’Alessio, J. Kent, A computational study of hydrocarbon growth and the formation of aromatics in coflowing laminar diffusion flames of ethylene, Combust. Flame 125 (2001) 1196-1206.

[117] D.B. Makel, I.M. Kennedy, Soot formation in laminar inverse diffusion flames, Combust. Sci. Technol. 97 (1994) 303-314.

[118] J. Du, R.L. Axelbaum, The effect of flame structure on soot-particle inception in diffusion flames, Combust. Flame 100 (1995) 367-375.

[119] L.D. Chen, J.P. Seaba, W.M. Roquemore, L.P. Goss, Buoyant diffusion flames, Proc. Combust. Inst. 22 (1989) 677-684.

[120] D. Durox, T. Yuan, E. Villermaux, The effect of buoyancy on flickering in diffusion flames, Combust. Sci. Technol. 124 (1997) 277-294.

[121] B.M. Cetegen, Y. Dong, Experiments on the instability modes of buoyant diffusion flames and effects of ambient atmosphere on the instabilities, Exper. Fluids 28 (2000) 546-558.

[122] X. Jiang, K.H. Luo, Combustion-induced buoyancy effects of an axisymmetric reactive plume, Proc. Combust. Inst. 28 (2000) 1989-1995.

[123] G.W. Sidebotham, I. Glassman, Flame temperature, fuel structure, and fuel concentration effects on soot formation in inverse diffusion flames, Combust. Flame 90 (1992) 269-283.

[124] A. Sobiesiak, J.C. Wenzell, Characteristics and structure of inverse flames of natural gas, Proc. Combust. Inst. 30 (2005) 743-749.

[125] C.R. Kaplan, K. Kailasanath, Flow-field effects on soot formation in normal and inverse methane–air diffusion flames, Combust. Flame 124 (2001) 275-294.

[126] M.A. Mikofski, T.C. Williams, C.R. Shaddix, L.G. Blevins, Flame height measurement of laminar inverse diffusion flames, Combust. Flame 146 (2006) 63-72.

[127] G.W. Sidebotham, I. Glassman, Effect of oxygen addition to a near-sooting ethene inverse diffusion flame, Combust. Sci. Technol. 81 (1992) 207-219.

[128] F. Xu, X. Liu, D.T. Stephen, Synthesis of carbon nanotubes on metal alloy substrates with voltage bias in methane inverse diffusion flames, Carbon 44 (2006) 570-577.

[129] G.W. Lee, J. Jurng, J. Hwang, Formation of Ni-catalyzed multiwalled carbon nanotubes and nanofibers on a substrate using an ethylene inverse diffusion flame, Combust. Flame 139 (2004) 167-175.

[130] C.J. Unrau, R.L. Axelbaum, P. Biswas, P. Fraundorf, Synthesis of single-walled carbon nanotubes in oxy-fuel inverse diffusion flames with online diagnostics, Proc. Combust. Inst. 31 (2007) 1865-1872.

[131] R.J. Santoro, T.T. Yeh, J.J. Horvath, H.G. Semerjian, The transport and growth of soot particles in laminar diffusion flames, Combust. Sci. Technol. 53 (1987) 89-115.

[132] K.T. Kang, J.Y. Hwang, S.H. Chung, W. Lee, Soot zone structure and sooting limit in diffusion flames: Comparison of counterflow and co-flow flames, Combust. Flame 109 (1997) 266-281.

[133] K.T. Wu, R.H. Essenhigh, Mapping and structure of inverse diffusion flames of methane, Proc. Combust. Inst. 20 (1985) 1925-1932.

[134] F.F. Grinstein, K. Kailasanath, Three-dimensional numerical simulations of unsteady reactive square jets, Combust. Flame 100 (1995) 2-10.

[135] F.F. Grinstein, K. Kailasanath, Exothermicity and three-dimensional effects in unsteady propane square jets, Proc. Combust. Inst. 26 (1996) 91-96.

[136] F.F. Grinstein, K. Kailasanath, Exothermicity and relaminarization effects in unsteady reactive square jets, Combust. Sci. Technol. 113 (1996) 291-312.

[137] X. Jiang, K.H. Luo, Dynamics and structure of transitional buoyant jet diffusion flames with side-wall effects, Combust. Flame 133 (2003) 29-45.

[138] X. Zhu, X. Xia, P. Zhang, Near-field Flow Stability of Buoyant Methane/Air Inverse Diffusion Flames, Combust. Flame 191 (2018) 66-75.

[139] H.G. Weller, G. Tabor, H. Jasak, C. Fureby, A tensorial approach to computational continuum mechanics using object-oriented techniques, Comp. Phys. 12 (1998) 620-631.

[140] R.I. Issa, Solution of the implicitly discretised fluid flow equations by operator-splitting, J. Comput. Phys. 62 (1986) 40-65.

[141] H. Jasak, Error analysis and estimation for finite volume method with applications to fluid flow, Ph.D. thesis, Imperial College, University of London (1996).

[142] B.P. Leonard, Simple high‐accuracy resolution program for convective modelling of discontinuities, Int. J. Numer. Methods Fluids 8 (1988) 1291-1318.

[143] M.T. Landahl, E. Mollo-Christensen, Turbulence and random processes in fluid mechanics, Cambridge University Press, Cambridge(1992).

[144] Z. Shu, S.K. Aggarwal, V.R. Katta, I.K. Puri, Flame-vortex dynamics in an inverse partially premixed combustor: The Froude number effects, Combust. Flame 111 (1997) 276-286.

[145] B.M. Cetegen, T.A. Ahmed, Experiments on the periodic instability of buoyant plumes and pool fires, Combust. Flame 93 (1993) 157-184.

[146] A.F. Ghoniem, I. Lakkis, M. Soteriou, Numerical simulation of the dynamics of large fire plumes and the phenomenon of puffing, Proc. Combust. Inst. 26 (1996) 1531-1539.

[147] T.L. Doligalski, C.R. Smith, J.D.A. Walker, Vortex interactions with walls, Ann. Rev. Fluid Mech. 26 (1994) 573-616.

[148] A. Luton, S. Ragab, D. Telionis, Interaction of spanwise vortices with a boundary layer, Phys. Fluids 7 (1995) 2757-2765.

[149] C.C. Chu, C.T. Wang, C.C. Chang, A vortex ring impinging on a solid plane surface—Vortex structure and surface force, Phys. Fluids 7 (1995) 1391-1401.

[150] N. Syred, J.M. Beer, Combustion in swirling flow: a review, Combustion and Flame 23 (2) (1974) 143-201.

[151] J.M. Beér, N.A. Chigier, Combustion aerodynamics, New York, (1972).

[152] E. Scheid, F. Pischinger, K. Knoche, H.-J. Daams, E. Hassel, U. Reuter, Spray combustion chamber with optical access, ignition zone visualization and first Raman measurements of local air-fuel ratio, SAE Technical Paper, 1986.

[153] D.L. Rhode, D.G. Lilley, D.K. Mclaughlin, Mean flowfields in axisymmetric combustor geometries with Swirl, AIAA Journal 21 (1983) 593-600.

[154] M. Ghaffarpour, B. Chehroudi, Experiments on spray combustion in a gas-turbine model combustor, Combustion Science and Technology 92 (1993) 173-200.

[155] A. Valera-Medina, N. Syred, P. Bowen, Central recirculation zone visualization in confined swirl combustors for terrestrial energy, Journal of Propulsion and Power 29 (2012) 195-204.

[156] J.K. Eaton, J.P. Johnston, A review of research on subsonic turbulent flow reattachment, AIAA journal 19 (1981) 1093-1100.

[157] Y.-w. Yan, J.-x. Zhao, J.-z. Zhang, Y. Liu, Large-eddy simulation of two-phase spray combustion for gas turbine combustors, Applied Thermal Engineering 28 (2008) 1365-1374.

[158] R. Hadef, B. Lenze, Measurements of droplets characteristics in a swirl-stabilized spray flame, Experimental thermal and fluid science 30 (2005) 117-130.

[159] Y. Hardalupas, A. Taylor, J. Whitelaw, Velocity and size characteristics of liquid-fuelled flames stabilized by a swirl burner, Proceedings of the Royal Society of London. A. Mathematical and Physical Sciences 428 (1990) 129-155.

[160] R. Chen, J.F. Driscoll, The role of the recirculation vortex in improving fuel-air mixing within swirling flames, Proceedings of the Combustion Institute 22 (1989) 531-540.

[161] V. Sankaran, S. Menon, LES of spray combustion in swirling flows, Journal of Turbulence 3 (2002) 1-23.

[162] M. Soltani, K. Ghorbanian, M. Ashjaee, M. Morad, Spray characteristics of a liquid–liquid coaxial swirl atomizer at different mass flow rates, Aerospace science and technology 9 (2005) 592-604.

[163] A. Williams, Combustion of liquid fuel sprays, Butterworth-Heinemann2013.

[164] A.H. Lefebvre, Gas turbine combustion, CRC Press2010.

[165] Y. Huang, V. Yang, Effect of swirl on combustion dynamics in a lean-premixed swirl-stabilized combustor, Proceedings of the Combustion Institute 30 (2005) 1775-1782.

[166] T.C. Lieuwen, V. McDonell, D. Santavicca, T. Sattelmayer, Burner development and operability issues associated with steady flowing syngas fired combustors, Combustion Science and Technology 180 (2008) 1169-1192.

[167] T.C. Lieuwen, V. Yang, Combustion Instabilities in Gas Turbine Engines: Operational Experience, Fundamental Mechanisms and Modeling, Progress in Astronautics and Aeronautics, doi:10.2514/4.866807(2005).

[168] S. Terhaar, T.G. Reichel, C. Schrödinger, L. Rukes, C.O. Paschereit, K. Oberleithner, Vortex breakdown types and global modes in swirling combustor flows with axial injection, Journal of Propulsion and Power, (2014) 1-11.

[169] V. Tangirala, J.F. Driscoll, Temperatures within non-premixed flames-effects of rapid mixing due to swirl, Combustion Science and Technology 60 (1988) 143-162.

[170] Y. Li, R. Li, D. Li, J. Bao, P. Zhang, Combustion characteristics of a slotted swirl combustor: An experimental test and numerical validation, International Communications in Heat and Mass Transfer, (2014).

[171] F.F. Grinstein, T.R. Young, E.J. Gutmark, G. Li, G. Hsiao, H.C. Mongia, Flow dynamics in a swirl combustor, Journal of Turbulence 3 (2002) 1-19.

[172] M.M. Kamal, Combustion characteristics of pulverized coal and air/gas premixed flame in a double swirl combustor, Combustion Science Technology 181 (2008) 136-158.

[173] R.K. Cheng, D.T. Yegian, M.M. Miyasato, G.S. Samuelsen, C.E. Benson, R. Pellizzari, P. Loftus, Scaling and development of low-swirl burners for low-emission furnaces and boilers, Proceedings of the Combustion Institute 28 (2000) 1305-1313.

[174] D. Littlejohn, R.K. Cheng, D. Noble, T. Lieuwen, Laboratory investigations of low-swirl injectors operating with syngases, Journal of Engineering for Gas Turbines and Power 132 (2010) 011502.

[175] S. Tachibana, J. Yamashita, L. Zimmer, K. Suzuki, A.K. Hayashi, Dynamic behavior of a freely-propagating turbulent premixed flame under global stretch rate oscillations, Proceedings of the Combustion Institute 32 (2009) 1795-1802.

[176] M.R. Johnson, D. Littlejohn, W.A. Nazeer, K.O. Smith, R.K. Cheng, A comparison of the flowfields and emissions of high-swirl injectors and low-swirl injectors for lean premixed gas turbines, Proceedings of the Combustion Institute 30 (2005) 2867-2874.

[177] D. Feikema, R.H. Chen, J.F. Driscoll, Enhancement of flame blowout limits by the use of swirl, Combustion and Flame 80 (1990) 183-195.

[178] ANSYS FLUENT 12.0 Theory Guide, (2009).

[179] A. Habibi, B. Merci, G.J. Heynderickx, Impact of radiation models in CFD simulations of steam cracking furnaces, Computers and Chemical Engineering 31 (2007) 1389-1406.

[180] H. Sheen, W. Chen, S. Jeng, Recirculation zones of unconfined and confined annular swirling jets, AIAA journal 34 (1996) 572-579.

[181] D.E. Ward, W.M. Hao, R.A. Susott, R.E. Babbitt, R.W. Shea, J.B. Kauffman, C.O. Justice, Effect of fuel composition on combustion efficiency and emission factors for

African savanna ecosystems, Journal of Geophysical Research: Atmospheres 101 (1996) 23569-23576.

[182] A. Gungor, Analysis of combustion efficiency in CFB coal combustors, Fuel 87 (2008) 1083-1095.